Title	Crystallographic and Thermoelectric Properties of Group 13 Elements-added Skutterudite Compounds
Author(s)	崔, 城豪
Citation	大阪大学, 2016, 博士論文
Version Type	VoR
URL	https://doi.org/10.18910/55969
rights	
Note	

Doctoral Dissertation

Crystallographic and Thermoelectric Properties of Group 13 Elements-added Skutterudite Compounds

SEONGHO CHOI

January 2016

Graduate School of Engineering

Osaka University

Thesis Advisors:

Professor Shinsuke Yamanaka, Ph.D.

Associate Professor Ken Kurosaki, Ph.D.

Yamanaka Laboratory, Division of Sustainable Energy and Environmental Engineering, Graduate School of Engineering, OSAKA UNIVERSITY

Thesis Committee:

Professor Shinsuke Yamanaka, Ph.D.

Professor Takao Yamamoto, Ph.D.

Associate Professor Ken Kurosaki, Ph.D.

Associate Professor Hiroshi Nishikawa, Ph.D.

Graduate School of Engineering

OSAKA UNIVERSITY

CONTENTS

CHAPTER I

Introduction

1.1 Background

There is an ongoing exploration for discovering sustainable and environment-friendly energy solutions. The solutions could be new resources or new ways to improve the utilisation of the conventional energy sources. The reason for the question is as follows: firstly, the majority of current energy resources are the fossil fuel such as oil, natural gas, and coal of hydrocarbon system.[1] The fuels have been created over millions of years, and are thus non-renewable, so humankind may run out of them some day. Furthermore, the combustion of the fossil fuels releases the gas CO_2, which brings about the green-house effect. It is well known that the increase in the amount of CO_2 in the atmosphere will increase the average temperature on earth, which may be a primary factor of the floods and draughts. The issues led to renewed interest in science and technology to provide a sustainable and environmental energy.[2] Thermoelectric (TE) phenomena, which involves the conversion between thermal and electric energy, are considered have the potential in meeting the future energy challenge.

TE devices have a simple structure and no moving parts, which means to cost less to maintain as well as environment-friendly. However, the efficiency of the TE devices is low as ever and not enough to be commercialized. The conversion efficiency of TE devices is fundamentally up to the properties of the embedded materials. My research has been within TE materials. They are materials that can convert heat into electricity due to a temperature difference, a so-called heat engine; or induce an electric current from a temperature difference by a heat flow, acting as a refrigerator., TE materials, operating as a heat engine, can utilise waste heat to minimise unnecessary energy losses; TE materials, operating as a refrigerator, might be able to outcompete commercial refrigerators in energy efficiency.

TE phenomena was discovered by Thomas Seebeck in 1821. Jean Charles Athanase Peltier discovered the refrigerating effect in 1834, and in 1854, Lord Kelvin connected the two effects while discovering other TE effects. In the next 80 years, Altenkirch's derivation of TE

efficiency in 1911 was the sole lasting contribution. The field of TE research got interest in the 1950's and TEs developed slowly and received little attention around the world during the 1960's-1990's. From the early 1990's, the research chances were given to advanced TE materials to the point that they could be more competitive in power generation and refrigeration applications from a performance point of view.[3,4] As a result, two different approaches were taken for the development of the next generation TE materials, new bulk TE materials and low dimensional TE materials.

In this thesis, I investigate on the thermoelectric (TE) material skutterudite. This type of material is found to be one of the most promising novel thermoelectric materials in the last two decades. Especially cobalt antimony based skutterudites, which can be modified by rare earths (RE), elements from other electropositive species, are expected to be used in prospective thermoelectric generator modules for high temperature purposes.

This thesis comprises five chapters: I Introduction, II Experimental Methods, III Thermoelectric properties of Tl-filled p-type Skutterudites, IV Thermoelectric properties of Ga and In co-added n-type Skutterudites, and V Summary. Chapter I introduces the basic knowledge about the TE effects, the Hall effect, dimensionless figure of merit zT and an applied theoretical models in this thesis (i.e. the single parabolic band and the Debye model). Furthermore the applicability of thermoelectric generators or Peltier coolers is briefly covered and recent concepts for novel thermoelectric materials are presented, which are in the focus of the scientific community. The experimental methods and calcualtions such as Rietveld refinement are described in Chapter II. The following chapters III and IV show the results and detailed discussion of this work, in which my focus lies on the crystallographic and TE properties of the skutterudite materials. The chemical compositions in each subsection are different and as follows: $Tl_xFe_{2.5}Ni_{1.5}Sb_{12}$, $Tl_xFe_{1.5}Co_{2.5}Sb_{12}$, $Ga_{0.2}In_xCo_4Sb_{12}$, and $Ga_{0.34}In_{0.11}Co_4Sb_{12}$ (the x in the chemical composition indicates that the particular elements are varied in their concentration). Finally, chapter V will summarize the results, which can be drawn from the experiments in this thesis.

1.2 Thermoelectric Phenomena

1.2.1 Thermoelectric effects and Hall effects[5]

The Seebeck effect is to generate a voltage along a conductor when a temperature difference in both side of conductor happens. In Figure 1.1(a), two different conductors, A and B, have the contact junctions at H and C, respectively. If a temperature difference happens between the H and the C, a charged carrier (electron or hole) moves from the hot side to the cold side, which applies an internal electric field to impede further movement. Seebeck coefficient S, in the open circuit conditions, is defined as $S_{AB} = V/\Delta T$. The differential Seebeck coefficient $S_{AB} = V/\Delta T = S_A - S_B$, where both S_A and S_B are the absolute S values of the conductors.
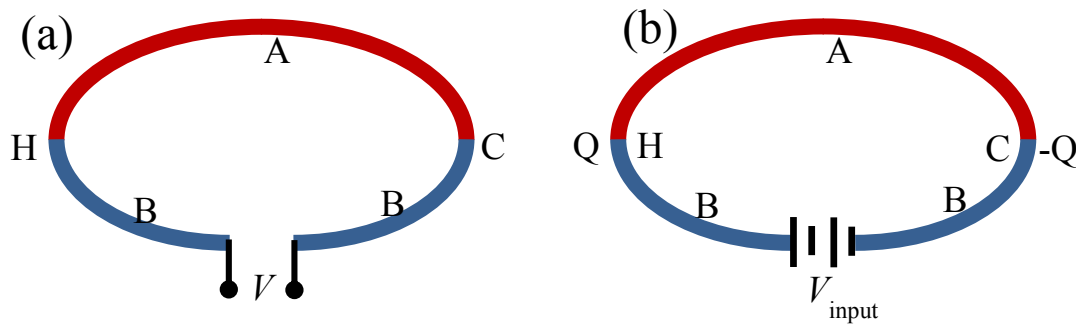

Figure 1.1 Schematic illustrations of (a) Seebeck effects and (b) Peltier effects

In contrast, **Peltier effect** means that a temperature difference is induced by applying a voltage between both sides, as seen in Figure 1.1(b). When the electrical current I is made to flow through a junction between two conductors, A and B, the Peltier heat Q generates at one junction and the Peltier cooling −Q generates at the other junction. The heat would be proportional to the current, Q= Π_{AB}I= (Π_A −Π_B)I. The constant Π is called as Peltier coefficient. The Peltier effect is different from Joule heating, is a reversible process and, is dependent on the direction of the current. As another effect in TEs, there is **Thomson effect**. It describes that the heat radiation or the heat absorption happen in a material which has a temperature gradient and voltage. A gradient of the heat flux is given as dQ/dx = τ_{AB}I(dT/dx), where x is a spatial coordinate, and τ is the Thomson coefficient. The three coefficients are related to each other, and Kelvin derived the relations, $\Pi_{AB} = S_{AB}T$ and $\tau_{AB} = T(dS_{AB}/dT)$.

The Hall effect was discovered by Edwin Herbert Hall in the year 1879 and signifies the response of charge carriers by an electric field within a conductor due to a applied magnetic field *B*, which is arranged non-parallel to a direction of a current density *j* (i.e. *j* × *B*). The charge carriers experience a Lorentz force due to the perpendicular magnetic component and, as a result, are deflected from their original path and accumulated vertically to the direction of the electrical current. The accumulation of charge carriers gives rise to the generation of a voltage perpendicular to the direction of the electrical current and is denoted as the Hall voltage. The Hall effect is reversible and only observed if a magnetic field is applied. In the simple case, the charge carriers create the Hall voltage V_H due to the magnetic field *B*, which is given by

$$V_H = \frac{-I \cdot B}{n_H \cdot e \cdot d} \tag{1.1}$$

Where the *I* is an applied current, *B* is a magnetic field, *d* is the thickness of the specimen, *e* is an electron charge and n_H is an charge carrier concentration. Hall coefficient R_H is defined as

$$R_H = \frac{E_y}{j_x \cdot B} = \frac{U_H \cdot t}{I \cdot B} = -\frac{1}{n_H \cdot e} \tag{1.2}$$

E_y is the induced transversal electrical field and j_x is the direction of the current density (perpendicular to the magnetic field). Latter is defined as $j_x = ne^2\tau E_x/m$, where τ is the charge carrier relaxation time, E_x is the longitudinal electrical field and *m* is a mass of the carriers. The charge carrier concentration means an effective charge carrier concentration, which is a superposition of minority and majority charge carrier concentrations. This is accordingly to the of the charge carrier mass *m*, which also becomes a superposition of two distinct charge carrier masses. Furthermore the Hall mobility μ_H of a particular material can be derived from the relation between the Hall constant R_H and the electrical conductivity σ, which is expressed as $\mu_H = |\sigma \cdot R_H|$.

1.2.2 Thermoelectric Figure of Merit

The basic component in TE device is the TE couple consisting of both a **p** branch with a positive *S* and an **n** branch with a negative *S*. Figure 1.2 shows the schematic of a TE couple. The two branches are joined by a metal interconnect. The two legs are connected thermally in parallel and electrically in series. The total thermal conductance and electrical resistance are:

$$K_{np} = \kappa_p A_p + \kappa_n A_n \qquad\qquad r_{np} = L\left(\frac{\rho_p}{A_p} + \frac{\rho_n}{A_n}\right) \qquad\qquad (1\text{-}3)$$

Where the κ, L and A are the thermal conductivity, the length and the cross section area of the legs, respectively.
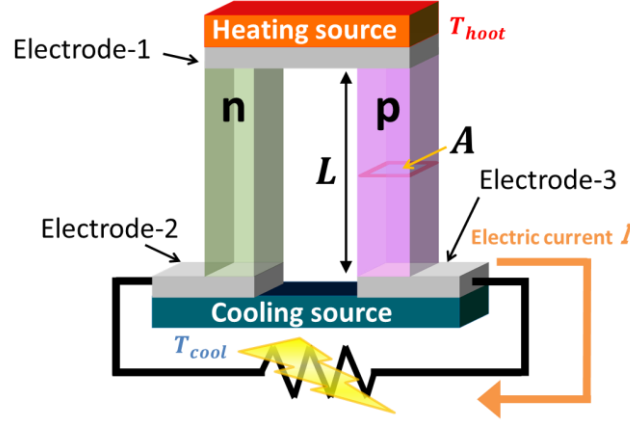

Figure 1.2 Schematic of a TE couple consisting of a *n*- and *p*-type thermoelectric material for TE power generator

In the electrode-1, one can consider that Q_{total} is total heat flow, Q_{np} is the absorbing heat, $Q_{H \rightarrow L}$ is the heat flow from total thermal conductance, and $Q_{J \rightarrow H}$ is the heat flow from the Joule heating. So,

$$Q_{np} = S_{np} I T_{hot} \qquad\qquad (1\text{-}4)$$

$$Q_{H \rightarrow L} = -K_{np}(T_{hot} - T_{cool}) \qquad\qquad (1\text{-}5)$$

$$Q_{J \rightarrow H} = \frac{1}{2}I^2 r_{np} \qquad\qquad (1\text{-}6)$$

The I is the current in the closed circuit. S_{np} is the Seebeck coefficient of this circuit. S_n and S_p are the Seebeck coefficients of *n*-type and *p*-type legs, respectively.

$$S_{np} = S_n - S_p \qquad\qquad (1\text{-}7)$$

$$Q_{total} = -Q_{np} - Q_{H \rightarrow L} - Q_{J \rightarrow H} \qquad\qquad (1\text{-}8)$$

$$Q_{total} = S_{np} I T_{hot} + K_{np}(T_{hot} - T_{cool}) - \frac{1}{2}I^2 r_{np} \qquad\qquad (1\text{-}9)$$

Also, if *V* is the thermal electromotive force,

$$I = \frac{V}{R + r_{np}} = \frac{S_{np}(T_{hot} - T_{cool})}{R + r_{np}} \qquad\qquad (1\text{-}10)$$

If *R* is the load resistance and *P* is the output power,

$$P = \{S_{np}(T_{hot} - T_{cool})\}^2 \frac{R}{(R + r_{np})^2} \qquad\qquad (1\text{-}11)$$

From above relations, the conversion efficiency η for whole circuit is

$$\eta = \frac{P}{Q_{total}} = \frac{\{S_{np}(T_{hot} - T_{cool})\}^2 \dfrac{R}{(R + r_{np})^2}}{S_{np}IT_{hot} + K_{np}(T_{hot} - T_{cool}) - \dfrac{1}{2}I^2 r_{np}}$$

$$= \frac{T_{hot} - T_{cool}}{T_{hot}} \frac{R/r_{np}}{1 + \dfrac{K_{np}r_{np}(R+r_{np})^2}{S_{np}{}^2\, T_{hot}r_{np}{}^2} - \dfrac{T_{hot}-T_{cool}}{2T_{hot}}} \qquad (1\text{-}12)$$

$K_{np}r_{np}$ could be minimized as the selection of cross section area in semiconductors.

$$\frac{\kappa_n}{\kappa_p}\frac{\rho_p}{\rho_n} = \left(\frac{A_p}{A_n}\right)^2 \qquad (1\text{-}13)$$

If one selects cross section area to satisfy the eq. (1-13), the efficiency is

$$\eta = \frac{T_{hot} - T_{cool}}{T_{hot}} \frac{R/r_{np}}{1 + \dfrac{1}{Z_{np}T_{hot}r_{np}{}^2}\dfrac{(R+r_{np})^2}{} - \dfrac{T_{hot}-T_{cool}}{2T_{hot}}} \qquad (1\text{-}14)$$

$$Z_{np} = \frac{S_{np}{}^2}{\left(\sqrt{\kappa_p\rho_p}+\sqrt{\kappa_n\rho_n}\right)^2} \qquad (1\text{-}15)$$

Z_{np} is the TE figure of merit from the properties of semiconductor. From the above eq. (1-14) and (1-15), one can know that the conversion efficiency is the harmonic increment function of Z_{np}. The figure of merit for each leg is

$$Z = \frac{S^2}{\kappa\rho} = \frac{S^2\sigma}{\kappa} \qquad (1\text{-}16)$$

Where σ is the electrical conductivity and $S^2\sigma$ is power factor. In order to maximize the conversion efficiency, the ratio between external and internal resistances is regard as $m = R/r_{np}$.

$$\eta = \frac{T_{hot} - T_{cool}}{T_{hot}} \frac{\dfrac{m}{m+1}}{1 + \dfrac{1}{Z_{np}}\dfrac{m+1}{T_{hot}} - \dfrac{T_{hot}-T_{cool}}{2T_{hot}(m+1)}}$$

$$= \frac{T_{hot}-T_{cool}}{T_{hot}} \frac{\dfrac{m}{m+1}}{1 + \dfrac{1}{Z_{np}T_{hot}}\dfrac{m+1}{} - \dfrac{T_{hot}-T_{cool}}{2T_{hot}(m+1)}} \qquad (1\text{-}17)$$

by $\partial\eta/\partial m = 0$,

$$m_{opt} = \sqrt{1 + Z_{np}\frac{T_{hot}+T_{cool}}{2}} = \sqrt{1 + zT} \qquad (1\text{-}18)$$

6

Here, zT is called as dimensionless figure of merit. The maximum conversion efficiency is

$$\eta_{max} = \frac{T_{hot}-T_{cool}}{T_{hot}} \frac{\sqrt{1+zT}-1}{\sqrt{1+zT}+T_{cool}/T_{hot}}$$
(1-19)
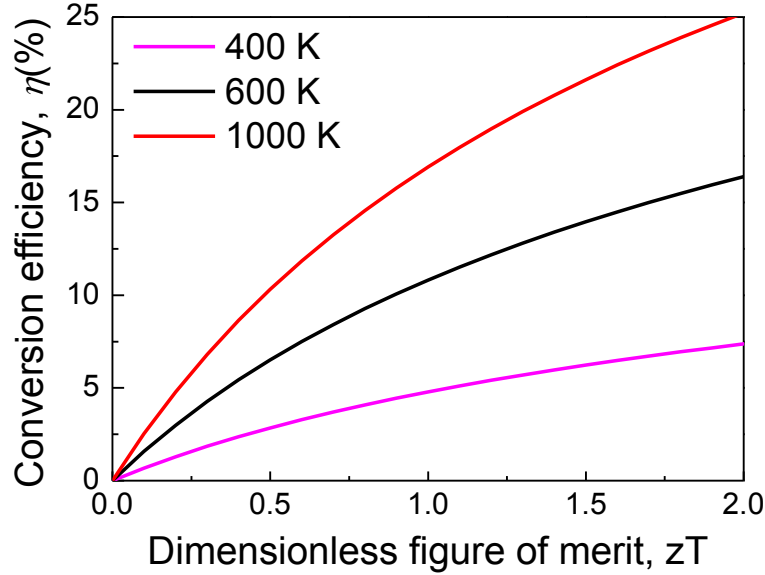
This relation is shown in Figure 1.3.

Figure 1.3 Efficiency of a power generator as a function of the material's dimensionless figure of merit zT

In other words, an enhancement of zT needs to improve the electrical properties (S, ρ), meanwhile, decrease the thermal conductivity κ. In TE field, the doping control for materials is a main technique to lead to the considerable change in the crystallographic and TE properties.[6] As shown in Figure 1.4, the S decreases and both electrical conductivity σ ($= \rho^{-1}$) and κ increase as the carrier concentration increases. Thus, power factor ($S^2\sigma$) and zT show mostly large values in the range of $10^{19} \sim 10^{20}$ cm^{-3}, which corresponds to the region of heavily doped semiconductor.[6,7]
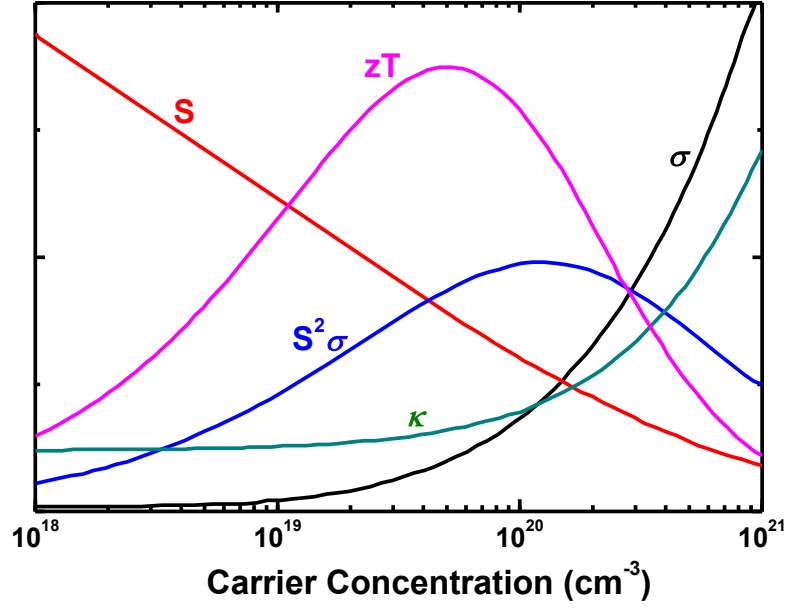
Figure 1.4 Carrier concentration dependences of the Seebeck coefficient S, the electrical conductivity σ, the power factor $S^2\sigma$, thermal conductivity κ, and dimensionless figure of merit zT. This relation was obtained by assuming single parabolic band and acoustic phonon scattering.

1.3 Transport of Electron and Heat

The characterization of TE materials primarily involves the measurement of the variables in equation $zT = S^2T/\rho\kappa$, which are the temperature dependent values of S, ρ and κ. This is the reasonable equation because the efficiency of the TE materials is a main topic for the advancement of the research on TE materials. For the further understanding of the materials however a physical interpretation of the particular variables is necessary. This is complicated by the fact that S, ρ and κ are interdependent on each other and are determined by several different phenomena.

Both, the single parabolic band model and the Debye approximation facilitate the interpretation of the measured transport properties of the skutterudite material. The former is used to interpret the electronic characteristics of the skutterudites and its deviations from a metal with a single parabolic band structure. The other, the Debye approximation, makes an estimation about the weighing of different scattering types (e.g. phonon-phonon interactions or scattering at crystal defects) and consequently gives more insight into the lattice thermal

conductivity of the material and help to further interpret possible deviations from this model (e.g. due to bipolar diffusion). These models can be applied to the skutterudite materials. The details will be discussed in upcoming sections.

1.3.1 Single Parabolic Band Model

The thermoelectric effects are non-equilibrium situations and consequently complicate an exact calculation of the macroscopic transport properties. Pioneering papers from Thomson, Boltzmann and Onsager helped to overcome this problem by assuming certain boundary conditions and simplifications.[8] With the work of Onsager this non-equilibrium situation can be regarded as a collection of local equilibria, which can be used to simplify a guess for the general Boltzmann transport equation, which has to be solved to derivate the macroscopic transport equations:

$$\frac{\partial f}{\partial t} = \left(\frac{\partial f}{\partial t}\right)_{diffusion} + \left(\frac{\partial f}{\partial t}\right)_{field} + \left(\frac{\partial f}{\partial t}\right)_{scattering} \tag{1-20}$$

The f denotes a distribution function f(r, k, t), which is introduced to describe the occupancy of allowed energy states. It may change due to a number of mechanisms: external fields, diffusion, and collision process.

Suppose we are dealing with a simple condition: one carrier (electrons or holes) resides in a single band. The band is in parabolic form $E = h^2k^2/(8\pi m^*)$. Using the relaxation-time approximation, the Boltzmann Transport Equation take the following form:

$$\frac{\partial f}{\partial t} + v \cdot \nabla f + qE \cdot \frac{\partial f}{\partial p} = \frac{f_0 - f}{\tau} \tag{1-21}$$

where $q=-e$ for electrons and $+e$ for holes. In the case of the steady state, the time dependence of the distribution function is much smaller than the space dependence of that, or $df/dt << v \cdot \nabla f$, so that we can assume $df/dt \approx 0$. The temperature slope and electric field is small so that the deviation from equilibrium distribution f_0 is small, i.e. $f_0-f << f_0$, and $df/dp \approx df_0/dp = (df_0/dE) \cdot (dE/dp) = v \cdot df_0/dE$. By applying these assumptions into eq. (1-21), it becomes

$$v \cdot \left(\nabla f + qE \cdot \frac{\partial f}{\partial E}\right) = \frac{f_0 - f}{\tau} \tag{1-22}$$

The equilibrium distribution of electrons described by the Fermi-Dirac distribution

$$f_0(k) = \frac{1}{\exp(\dfrac{E(k)-\mu}{k_BT})+1} = \frac{1}{\exp(\eta)+1}; \quad \eta \equiv \frac{E-\mu}{k_BT} \qquad (1\text{-}23)$$

Where μ is the chemical potential which relies weakly on the temperature and strongly on the carrier concentration. Both E and μ can be measured from the band edge state.

From eq. (1-23)

$$\frac{\partial f_0}{\partial E} = \frac{df_0}{d\eta}\frac{\partial \eta}{\partial E} = \frac{df_0}{d\eta}\frac{1}{k_BT} \qquad (1\text{-}24)$$

From eq. (1-24)

$$\nabla f_0 = \frac{df_0}{d\eta}\nabla \eta = k_BT\frac{\partial f_0}{\partial E}\nabla \eta \qquad (1\text{-}25)$$

From $\nabla E(k) = 0$ for the reference system

$$\nabla \eta = \frac{1}{k_BT}(\nabla E(\vec{k}) - \nabla \mu) - \frac{E-\mu}{k_BT^2}\nabla T = -\frac{1}{k_BT}\nabla\mu - \frac{E-\mu}{k_BT^2}\nabla T \qquad (1\text{-}26)$$

From eq. (1-25) and (1-26),

$$\nabla f_0 = -\frac{\partial f_0}{\partial E}(\nabla\mu + \frac{E-\mu}{T}\nabla T) \qquad (1\text{-}27)$$

Combine eqs. (1-22) and (1-27),

$$\vec{v}\cdot[-\nabla\mu - \frac{E-\mu}{T}\nabla T + q\vec{E}]\frac{\partial f_0}{\partial E} = \frac{f_0 - f}{\tau} \qquad (1\text{-}28)$$

Note that

$$E = -\nabla\varphi_e \qquad\qquad \Phi = \mu + q\varphi_e \qquad (1\text{-}29)$$

Where φ_e is the electrostatic potential, and Φ is the electro-chemical potential which combines the electrostatic potential energy and the chemical potential. The electro-chemical potential is the driving force for current flow, which used to cause by the gradient in either the electrostatic potential or the chemical potential.

From eqs. (1-28) and (1-29)

$$f = f_0 - \tau v\cos\theta\left[-\frac{d\Phi}{dx} - \frac{E-\mu}{T}\frac{dT}{dx}\right]\frac{\partial f_0}{\partial E} \qquad (1\text{-}30)$$

Considering a simple situation, the field and temperature gradient lie along the x axis. There will be no flow of current when f is equal to f_0. The energy flux for charge carriers is expressed as

$$J = \frac{1}{3} \int_{E=0}^{\infty} \frac{\partial f_0}{\partial E} D(E) q v^2 \tau \left(\frac{d\mu}{dx} + \frac{E - \mu}{T} \frac{dT}{dx} - qE_z \right) dE \tag{1-31}$$

Use $E = mv^2/2$ to remove v in eq. (1-31)

$$J = \frac{2q}{3m} \int_{E=0}^{\infty} \frac{\partial f_0}{\partial E} D(E) E \tau \left(\frac{d\Phi}{dx} + \frac{E - \mu}{T} \frac{dT}{dx} \right) dE \tag{1-32}$$

Eq. (1-32) can be rearranged as

$$J = L_{11} \left(-\frac{1}{q} \frac{d\Phi}{dx} \right) + L_{12} \left(-\frac{dT}{dx} \right) \tag{1-33}$$

where

$$L_{11} = -\frac{2q^2}{3m} \int_{E=0}^{\infty} \frac{\partial f_0}{\partial E} D(E) E \tau dE \tag{1-34}$$

$$L_{12} = -\frac{2q}{3mT} \int_{E=0}^{\infty} \frac{\partial f_0}{\partial E} D(E) E (E - \mu) \tau dE \tag{1-35}$$

In the case of zero temperature gradient and zero carrier concentration gradient, $dT/dx = 0$ and $du/dx = 0$, eq. (1-34) becomes

$$J = L_{11} \left(-\frac{1}{q} \frac{d\Phi}{dx} \right) = L_{11} \left(-\frac{1}{q} \frac{d\mu}{dx} + E_x \right) = L_{11} E_x \tag{1-36}$$

The electrical conductivity is defined as

$$\sigma \equiv \frac{J}{E_x} = L_{11} = -\frac{2q^2}{3m} \int_{E=0}^{\infty} \frac{\partial f_0}{\partial E} D(E) E \tau dE \tag{1-37}$$

A thermoelectric voltage, in the case of non-zero temperature gradient along the x direction, can be measured between the two ends of the dense matter with an open loop electrometer, i.e. $J = 0$. Thus, from eq. (1-34), we acquire

$$J = L_{11} \left(-\frac{1}{q} \frac{d\Phi}{dx} \right) + L_{12} \left(-\frac{dT}{dx} \right) \tag{1-38}$$

Thus,

$$\frac{\left(\dfrac{d\Phi}{dx}\right)}{\left(\dfrac{dT}{dx}\right)} = -\frac{qL_{12}}{L_{11}} \tag{1-39}$$

As mentioned above, the voltage which the electrometer measure between the two ends of the solid is $\Delta V = \Delta\Phi/q$. The Seebeck coefficient is defined as the ratio between the voltage gradient and the temperature gradient for an open loop configuration with zero net current flow

$$S = -\frac{\left(\dfrac{dV}{dx}\right)}{\left(\dfrac{dT}{dx}\right)} = -\frac{1}{q}\frac{\left(\dfrac{d\Phi}{dx}\right)}{\left(\dfrac{dT}{dx}\right)} = \frac{L_{12}}{L_{11}} = -\frac{1}{qT}\left(\mu - \frac{\displaystyle\int_{E=0}^{\infty} \frac{\partial f_0}{\partial E} D(E)E^2\tau dE}{\displaystyle\int_{E=0}^{\infty} \frac{\partial f_0}{\partial E} D(E)E\tau dE} \right) \tag{1-40}$$

From above equations, we can rewrite

$$J = \sigma\left(-\frac{1}{q}\frac{d\Phi}{dx}\right) + \sigma S\left(-\frac{dT}{dx}\right) \tag{1-41}$$

The relaxation time of the scattering is dependent on the energy, and it can be assumed as $\tau = \tau_0 E^r$, where τ_0 is a constant independent on E.

When E is measured from the band edge for either holes or electrons, the density of states

$$D(E) = \frac{(2m)^{3/2}}{2\pi^2\hbar^3} E^{1/2} \tag{1-42}$$

Thus,

$$S = -\frac{1}{qT}\left(\mu - \frac{\displaystyle\int_{E=0}^{\infty} \frac{\partial f_0}{\partial E} D(E)E^2\tau dE}{\displaystyle\int_{E=0}^{\infty} \frac{\partial f_0}{\partial E} D(E)E\tau dE} \right) = -\frac{1}{qT}\left(\mu - \frac{\displaystyle\int_{E=0}^{\infty} \frac{\partial f_0}{\partial E} E^{2+r+1/2} dE}{\displaystyle\int_{E=0}^{\infty} \frac{\partial f_0}{\partial E} E^{1+r+1/2} dE} \right) \tag{1-43}$$

The integrals can be simplified using the product rule

$$\int_{E=0}^{\infty} \frac{\partial f_0}{\partial E} E^s dE = f_0 E^s \big|_0^{\infty} - s\int_{E=0}^{\infty} f_0 E^{s-1} dE = -s\int_{E=0}^{\infty} f_0 E^{s-1} dE \tag{1-44}$$

Using eq. (1-44) to reduce eq. (1-43) to

$$S = -\frac{1}{qT}\left(\mu - \frac{(r+5/2)\int\limits_{E=0}^{\infty} f_0 E^{r+3/2} dE}{(r+3/2)\int\limits_{E=0}^{\infty} f_0 E^{r+1/2} dE} \right) \qquad (1\text{-}45)$$

The two integrals in eq. (1-45) can be simplified with the reduced energy $\zeta = E/k_{BT}$

$$\int\limits_{E=0}^{\infty} f_0(E,\mu) E^n dE = (k_B T)^{n+1}\int\limits_{0}^{\infty} f_0(\zeta,\eta)\zeta^n d\zeta = (k_B T)^{n+1} F_n(\eta); \quad \eta = \mu/k_B T \qquad (1\text{-}46)$$

where the Fermi-Dirac integral is defined as

$$F_n(\eta) = \int\limits_{0}^{\infty} f_0(\zeta,\eta)\zeta^n d\zeta \qquad (1\text{-}47)$$

Use Eq. (1-46) to reduce eq. (1-45) to

$$S = -\frac{1}{qT}\left(\mu - k_B T \frac{\left(r+\frac{5}{2}\right)F_{r+3/2}(\eta)}{\left(r+\frac{3}{2}\right)F_{r+1/2}(\eta)} \right) = -\frac{k_B}{q}\left(\eta - \frac{\left(r+\frac{5}{2}\right)F_{r+3/2}(\eta)}{\left(r+\frac{3}{2}\right)F_{r+1/2}(\eta)} \right) \qquad (1\text{-}48)$$

where k_B is a Boltzmann constant, the e is a fundamental charge, the r is the scattering exponent, η is the reduced Fermi energy. For temperatures beyond the Debye temperature, acoustic scattering was assumed for the calculation, which is in terms of the scattering exponent $r = 0$. Furthermore, the carrier concentration n can be determined and is mathematically derived from the Boltzmann transport equation as follows:

$$n = \sqrt{\frac{2}{\pi}}\left(\frac{m^* k_B T}{\hbar^2} \right)^{3/2} F_{1/2}(\eta) \qquad (1\text{-}49)$$

Where the $\hbar$ is the reduced Planck constant and the m^* is the density of states (DOS) effective mass. The DOS effective mass m^* can be determined by adjusting it to the measured data in a *S-n* diagram. The fitted value of m^* denotes the density of states effective mass for a single parabolic band. In a more complex band structure, where several bands at one point in the reciprocal space may exist (i.e. non-parabolic), the fitted value of m^* is a mean value of several effective masses and additionally with different weighting. Nevertheless, with this procedure, m^* can be easily approximated and the band degeneracy can be directly identified, when the measured values of the carrier concentration and the Seebeck coefficient systematically deviate from the model.

1.3.2 Debye Model

The calculation of the lattice thermal conductivity is carried out to draw conclusions about the particular scattering mechanisms, which are taking place at the projected temperature between 300 and 700K in the skutterudite material. In the Debye model all branches of the vibrational spectrum are replaced by three branches with the identical dispersion relation:

$$\omega = c \cdot k \tag{1-50}$$

Where the ω is an angular frequency, the c is the speed of light and k is the wave vector. Using this approximation, a simplification of the Boltzmann equation can be attained, without knowing the exact phonon spectra of the material. Thus the phonon relaxation time τ_{ph}, which consists of several scattering types, can be approximated and compared to the experimental data. In this model the lattice thermal conductivity κ_{lat} is derived from the thermal conductivity data $\kappa(T)$ by application of the Wiedemann-Franz law and the calculated Lorenz number L_0. In the following the derivation of the lattice thermal conductivity is briefly summarized and the main assumptions of this model are presented.[9,10]

The thermal conductivity κ is mathematically described in the kinetic theory as follows

$$\kappa = \frac{1}{3} C \cdot \upsilon \cdot l \tag{1-51}$$

C is the specific heat capacity, v the mean velocity of the particles (phonons) and l is the mean free path between two scattering events. Equation (1.51) is phenomenological a good description of the thermal conductivity. However a mathematical treatment of the lattice thermal conductivity κ_{lat}, which is a non-equilibrium transport parameter, has to consider the microscopic response by the crystal lattice due to heat conduction, i.e. to obtain a solution of the Boltzmann transport equation with reasonable assumptions. The linearized Boltzmann equation can be written as

$$\frac{f_{ph} - f_{ph}^0}{\tau_{ph}} = v_g \cdot \nabla T \frac{\partial f_{ph}^0}{\partial T} \tag{1-52}$$

Where f_{ph} is the phonon distribution function, f_{ph}^0 is the local equilibrium distribution and v_g is the phonon group velocity. It is an assumption of the linearized Boltzmann equation to distinguish between a local equilibrium distribution f_{ph}^0 and a (general) distribution function

f_ph, i.e. the system will experience a local distribution, which tends to return to the (general) distribution function. Furthermore the Bose-Einstein distribution is valid here, since the involved particles are phonons. In the diffusion term of the Boltzmann equation (right side of equation (1.52)) a temperature gradient is present, which represents (a steady state) temperature field in the specimen.

When the equation (1.52) is solved, κ_{lat} can be expressed as follows:

$$\kappa_{lat} = \frac{\left|\vec{Q}\right|}{\left|\nabla T\right|} = \frac{1}{2\pi^2 v} \int_0^{\omega_D} \hbar\omega^3 \tau_{ph}(\omega) \frac{\hbar\omega/k_B T^2 \cdot e^{\hbar\omega/k_B T}}{\left(e^{\hbar\omega/k_B T} - 1\right)^2} \cdot d\omega \qquad (1\text{-}53)$$

Where $\left|\vec{Q}\right|$ is the heat flux, ω_D is the Debye frequency ($\omega_D = k_B \theta_D / \hbar$), v is the average phonon velocity (simplification by the Debye theory) and for f_{ph}^0 the phonon distribution function is inserted ($f_{ph}^0 = 1/(exp(\hbar\omega/k_B T) - 1)$). When $\hbar\omega/k_B T$ is substituted by x and the Debye temperature θ_D is entered into eq. (1-53), it gives the Debye approximation, which is applied in this work to compare it to the experimental data:

$$\kappa_{lat} = \frac{k_B}{2\pi^2 v} \left(\frac{k_B T}{\hbar}\right)^3 \int_0^{\theta_D/T} \tau_{ph} \frac{x^4 e^x}{\left(e^x - 1\right)^2} \cdot dx \qquad (1\text{-}54)$$

This equation is clearly dependent on the phonon relaxation time τ_{ph}, which is governed by the Matthiessen rule and the different scattering mechanisms. Consequently the inverse phonon relaxation time can be approximated by the expression:

$$\tau_{ph}^{-1} = \frac{v}{L} + A\omega^4 + B\omega^2 T e^{-\theta_D/3T} + \frac{C\omega^2}{\left(\omega_0^2 - \omega^2\right)^2} \qquad (1\text{-}55)$$

Where ω_0 being the resonance frequency of the filler element (discussed later), *L* is the average grain size, and the coefficients *A, B, C* are the fitting parameters. The terms on the right side of equation (1.55) represents the boundary and point defect scattering, phonon-phonon Umklapp processes and the phonon resonant scattering contribution, respectively. Boundary scattering is dominating in the low temperature regime, whereas Umklapp scattering is strongly present at higher temperatures. Point defect scattering is important for the intermediate temperature range and the phonon resonant scattering is an approach to include the characteristic of the skutterudites which are the target material in this thesis.

1.4 Skutterudites

Recently, TE devices are mainly receiving attention from the automobile industry, a higher value-added business. It has been known that the large part (nearly 40%) of the energy released in fuel combustion process of automobiles is lost as the form of the waste exhaust gas heat.[11] To be the good TE materials for applications in automobile industry, the high thermos-mechanical and chemical compatibilities are required to the temperature over 500℃, the maximum temperature of exhaust heat gas in automobile system. Considering the temperature of the coolant part around 150℃, for the application in automobile, we need to develop the TE materials with high average zT approximately between 300℃ and 500℃. Thus, as suitable materials at the temperature range, PbTe-based materials have shown the excellent TE properties over a decade through the enhanced power factor by the electronic band engineering and the reduction of lattice thermal conductivity by precise doping control. However, the PbTe has strong toxicity for human and thus it needs to be replaced. Therefore, we need the materials to satisfy the conditions such as the same application temperature range, minimum toxicity to people, and inexpensive elements. The conditions can be satisfied by $CoSb_3$-based skutterudites which are promising for the application for automobile systems.[11,12]
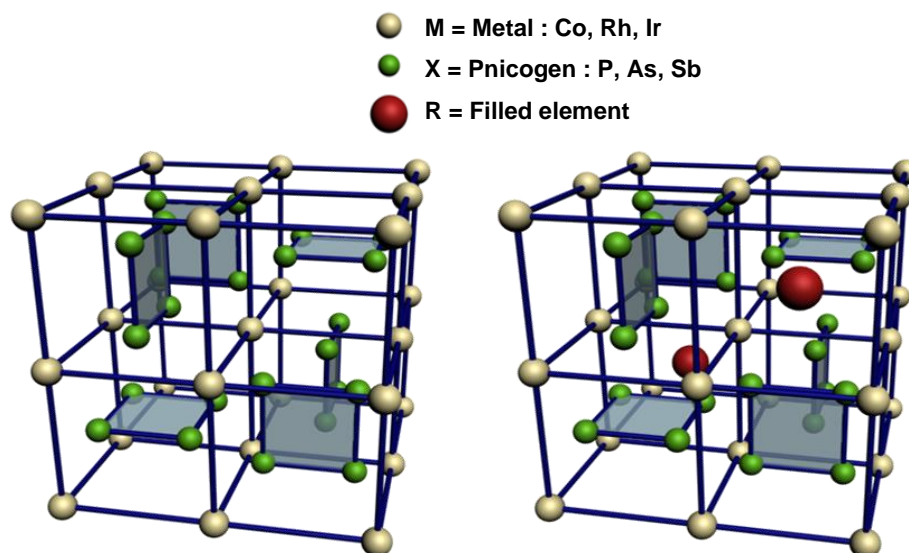

Figure 1.5 Crystal structures of skutterudite(left) and filled skutterudite(right)

The origin of the name skutterudite derives from, Skutterud (Norway), the place of finding, where the mineral $CoAs_3$ was firstly discovered.[13] The bare Skutterudite have a composition MX_3, where the M is one of the group 8 transition metals such as Co, Rh, or Ir and the X represents the pnicogen atom such as P, As, or Sb.(Figure 1.5)[13,14] It consists of 32 atoms and corresponds to the space group Im-3 (#204), where the transition metals and the pnicogen atoms occupy the 8c-sites (1/4, 1/4, 1/4) and the 24g-sites (0, y, z), respectively.[14] The pnicogen atoms form a rectangle ring consisting of four atoms and include the transition metal in an octahedral coordination. Oftedal assumed that the rectangle ring of pnicogen atoms is strongly constrained and follows the structural rule, i.e. $y + z = 0.5$, although it shows a little rectangular distortion. As a unique feature of the bare-skutterudite structure, it is well known that the skutterudite structure has cage-like two 2a void sites (0,0,0) as the interstitial site in an unit cell. The voids are large sizes and thus the additional atoms can be inserted. There is a huge variety of elements, such as rare earths, which can be selected as a "filler R" for the void sites. The filling the filler R elements into the void sites of skutterudites forms the compounds with composition RMX_3 which is called filled skutterudites.(Figure 1.5) Constraints for the selection are mainly the ion radii and the electronegativity of the relevant element.[15]
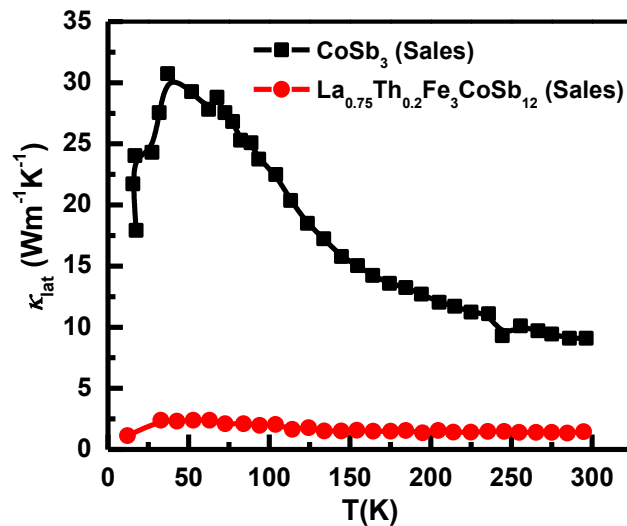

Figure 1.6 The reduction of lattice thermal conductivity by rattling effect.[13]

In the year 1997, a first attempt to explain the effectiveness of the filler elements with regard to the lattice thermal conductivity was done by Sales et al..[13] According to the paper, the large atomic displacement parameter of the void filling elements is believed to describe an independent Einstein oscillation and was subsequently denoted as "rattling" in this context.

Figure 1.6 shows the reduction of lattice thermal conductivity by rattling effect from the filling process. This oscillation of the filler element is capable of scattering the heat carrying phonons efficiently, which is reflected in a considerable reduction of the thermal conductivity.[16]
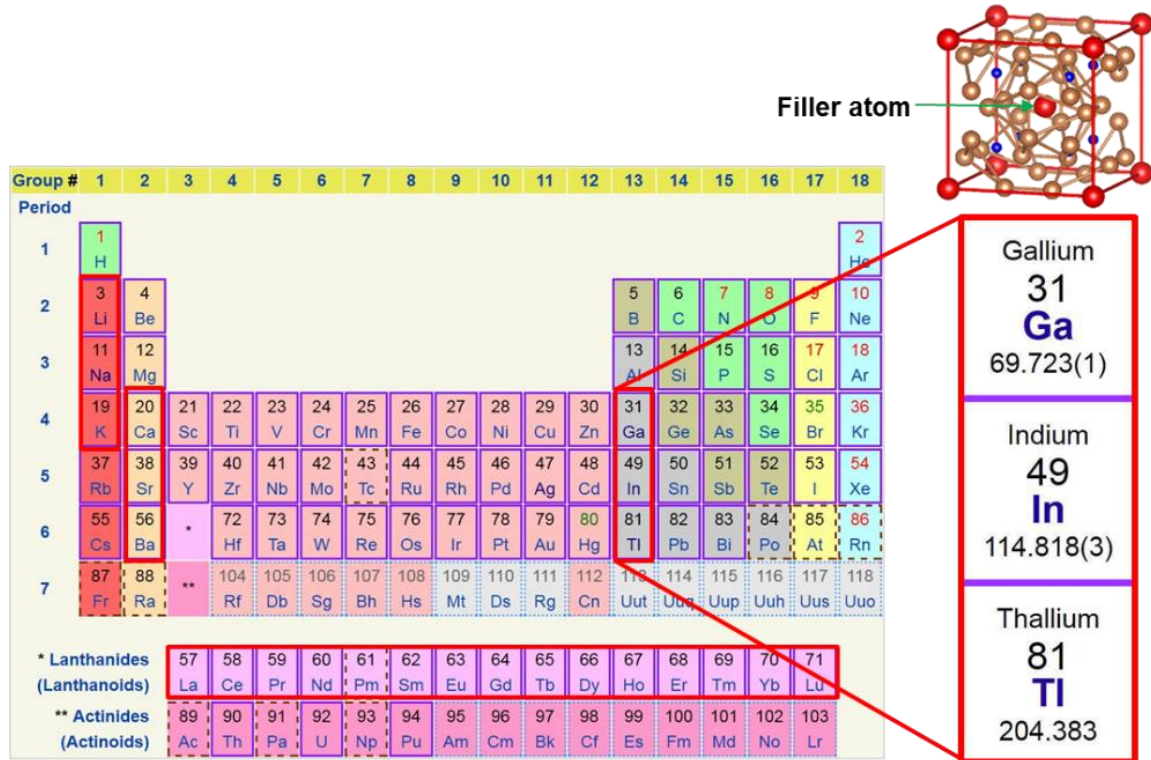
1.5 Motivations

Figure 1.7 Periodic table

Since filled skutterudites have such a big potential to be a good TE materials, it has been widely reported that the voids of skutterudite structures could be filled with a variety of different atoms such as rare earth, alkaline, and alkaline earth groups.[17-30] These elements have been studied so far. However, the reports on the TE properties of group 13 elements filled skutterudites have been limited.

In particular, reports on high temperature TE properties of group 13 elements filled p-type skutterudites have been scarcely investigated. Figure 1.8 shows the dimensionless figure of merit of p-type filled skutterudites. One can see the In-filled p-type skutterudite with low zT. However, since group 13 elements have shown the excellent properties in n-type skutterudites, one can consider that they are promising filler candidates for p-type skutterudires.
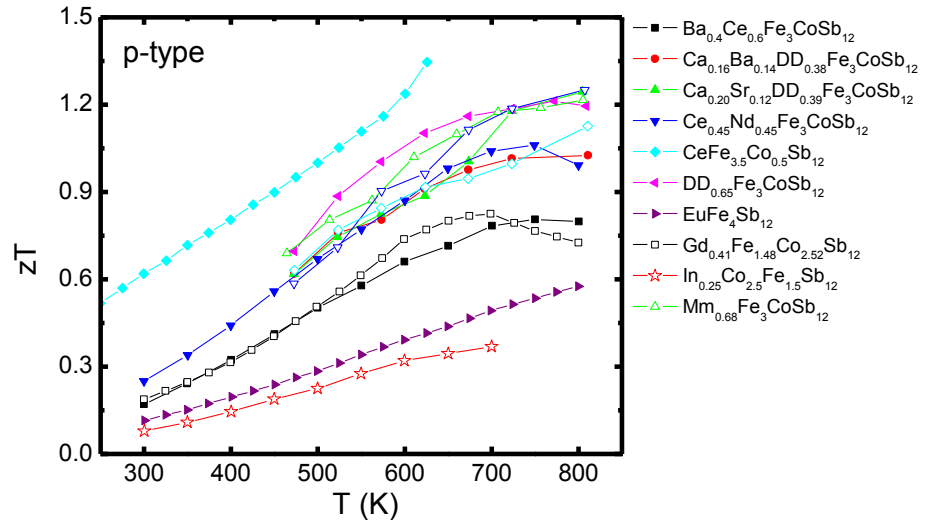
Figure 1.8 The dimensionless figure of merit of *p*-type filled skutterudites[24,31-34]

On the other hand, multiple-filled skutterudites with group 13 elements have yielded good TE properties. Figure 1.9 shows multiple filling with group 13 elements for skutterudites is significantly effective compared to the single filling. In particular, the study for Ga and In co-filled skutterudites has not been performed yet and the combination of both Ga and In is worth investigating for the easily oxidizable other elements.
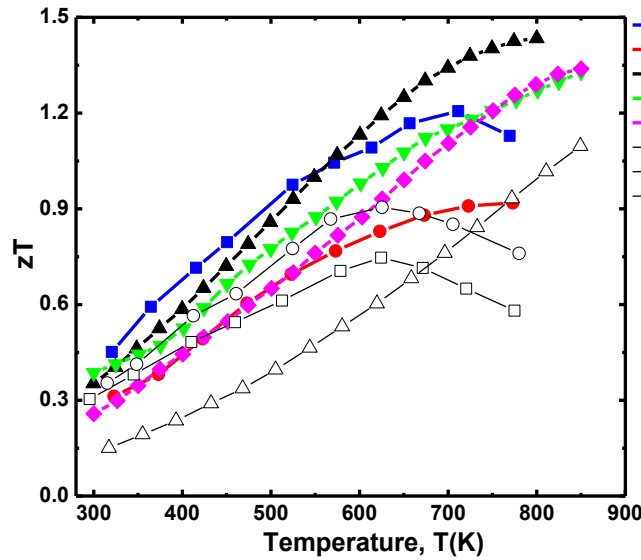
Figure 1.9 The dimensionless figure of merit of *n*-type filled skutterudites[18,35-40]

1.6 Purpose of the present dissertation

The purpose of the present study is to investigate the behaviour of group 13 elements in skutterudites and to develop the materials with high TE properties. As mentioned, the reports of group 13 elements added skutterudites have been limited and the behaviour of group 13 elements in skutterudites is ongoing debate due to the unusual behaviour. Thus, the crystal structure and chemical compositions have been precisely investigated. On the basis of the crystallographic information, the TE properties of the materials have been analysed.

In the present dissertation, group 13 elements added p-type and n-type skutterudites have been investigated. Firstly, the crystallographic and TE properties of $Tl_xFe_{2.5}Ni_{1.5}Sb_{12}$ and $Tl_xFe_{1.5}Co_{2.5}Sb_{12}$ systems as Tl-filled p-type skutterudites were studied. It is known that Tl occupies the void sites in $CoSb_3$-based skutterudites and contributes the enhancement of TE properties.[16,41,42] On the other hand, since Cobalt is a very expensive element, it needs to be replaced by the cheaper elements in order to mass production. Thus, we have investigated $Tl_xFe_{2.5}Ni_{1.5}Sb_{12}$ as Co-free system and $Tl_xFe_{1.5}Co_{2.5}Sb_{12}$ as low Co system. Secondly, the crystallographic and TE properties of $Ga_{0.2}In_xCo_4Sb_{12}$ and $Ga_{0.34}In_{0.11}Co_4Sb_{12}$ systems have been studied. The position and occupation of both Ga and In in $CoSb_3$-based skutterudites is not clear yet, which needs to be revealed experimentally. On the other hand, for $CoSb_3$-based skutterudites, the multiple filling is a very effective approach to enhance the TE properties, which results from the multiple-frequency resonant phonon scattering.[21,30,37,38,43-49] Thus, the TE properties of Ga and In co-added skutterudites had been studied [50] and the advanced study for that has been carried out through the additional analysis in the present study. Furthermore, the optimization study for the enhancement of TE properties was carried out from the modification of the composition and microstructure.

CHAPTER II

Experimental Methods

In the present study, the polycrystalline bulk skutterudites were made by the conventional solid-state reaction and then consolidated by hot pressed sintering. For as-consolidated samples, the microstructural and crystallographic characterizations by both X-ray powder diffraction (XRD) method and Field-emission scanning electron microscopy (FE-SEM) with Energy Dispersive X-ray spectrometry (EDX) were firstly carried out at room temperature and the thermoelectric (TE) properties were evaluated from ZEM-1, Hall effects, and Laser flash method from 300 K to 773 K. The basic principle of such synthesis and analysis methods will be explained in the present chapter.

2.1. Sample Preparation by Solid State Reaction

As shown in Figure 2.1, since the intermetallic phase for pure $CoSb_3$ experiences the decomposition by a peritectic reaction at 1147 K, skutterudites couldn't be obtained from simply melt-growth methods. However, there are various methods to synthesize skutterudites.
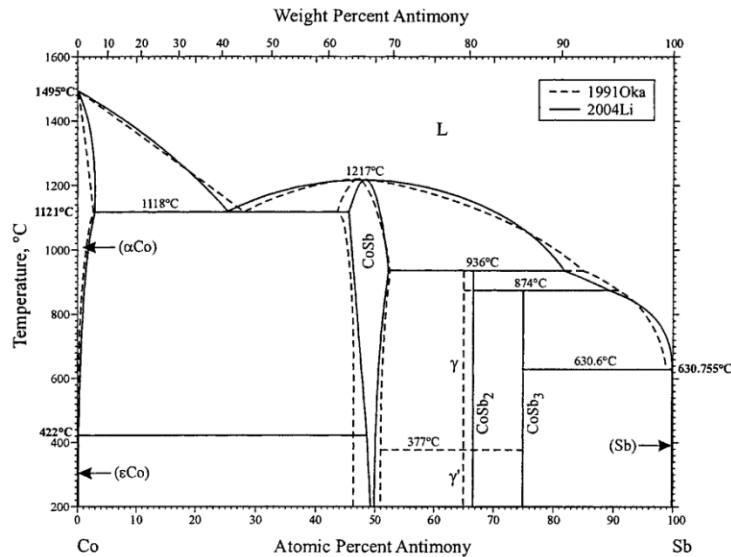
Figure 2.1 Phase diagram of binary Co-Sb system[51]

Among the possible methods, in the present study, the conventional melt-quench-annealing method was performed in order to synthesize the skutterudites.

The synthesis started with putting the start chemicals into silica quartz tube. In particular, since thallium is easy to oxidize, it was placed in a silica tube under argon atmosphere within a glove box system. Then, the evacuated quartz ampoule was sealed with an oxygen/hydrogen torch. The sealed quartz ampoules were placed into the vertical furnace. After the melting process, the ampoules were quenched in cold water. The quenched samples were placed in the vertical furnace and then were long term annealed over 1 week.

The annealed samples were pulverized and then as-prepared powder type samples were firstly cold pressed into a pellet, which was then placed into the graphite die to be heated by a furnace and pressed by upper graphite punch as shown in Figure 2.2.
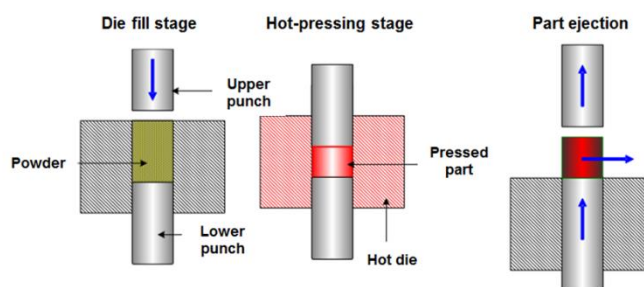
Figure 2.2 Schematic image of hot-pressing technique

2.2. Characterizations Methods

2.2.1 X-ray Powder Diffraction

For all samples, the X-ray diffraction (XRD) analysis was carried out. The incident X-ray interacts with electrons in atoms on the first order. When the X-ray photons collide with the electrons in the orbitals of atoms, some photons are turned away from the direction where they are originally progressing. If the scattered photons keep move without changing the wavelength, this process is called elastic scattering or Thomson scattering. If the electrons are on the propagation path of the incident X-ray, they are vibrated with the same periodic manner of the the incident X-ray wave and thus, with the electron as the center, the electromagnetic wave with the same periodicity spherically occurs. The X-ray intensity I_e for one electron scattering is proportional to the incident X-ray and is varied as the observed direction and the distance for the observed positions, etc. This is expressed as

$$I_{\mathrm{e}} = I_0 \frac{e^4}{r^2 m^2 c^4} \frac{1+\cos^2(2\theta)}{2} \qquad (2\text{-}1)$$

Where I_0 is the intensity of the incident X-ray, r is the distance to observed position, m is the electron mass, e is the fundamental charge, and c is the speed of light.

A crystal generally means a solid material whose constituents, such as atoms, molecules or ions, are arranged in a highly ordered microscopic structure, forming a crystal lattice that extends in all directions.[52] When the X-ray is applied to the crystal, the X-ray is scattered by each phase, which would be satisfy the following Bragg's law.[53]

$$n\lambda = 2d \sin\theta \qquad (2\text{-}2)$$
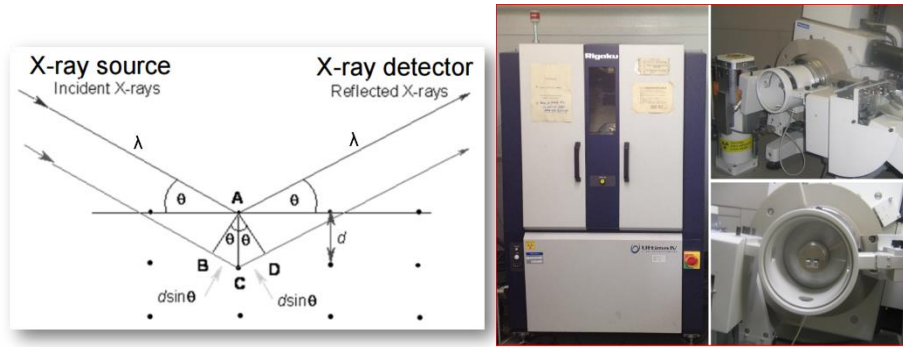
Figure 2.3 Relation between wavelength λ, atomic spacing d and angle θ in Bragg's law (left) and XRD apparatus used in the present study (right)

The powder XRD is the widely used X-ray techniques to characterize the materials. The sample to be characterized is almost the powder form which has the crystalline domains randomly oriented. Thus, when two dimensional diffraction pattern was obtained, it shows the rings of the scattering peaks corresponding to the various spacing d in a lattice. The intensities and positions of peaks are applied for confirming the underlying phases of the materials.

The powder XRD is possible not only to simply use as a screening tool but also to evaluate a structural model. Rietveld refinement is a promising technique used to relate a structural model to an experimental diffraction pattern. As the Rietveld method requires a starting structural model, preferable in reasonably good agreement with the experimental diffraction patterns, it can be considered as a refinement technique.

In this research, the X-ray diffraction (XRD) measurement was performed on Rigaku, Ultima IV X-ray diffractometer using *Cu-Kα* radiation $\left(\lambda = 1.5406\text{Å}\right)$ at room temperature.

The lattice parameter, unit cell volume and theoretical density were calculated from the XRD results using commercial program PDXL. To obtain the good quality diffraction pattern and improved statistics, the measurement for samples was slowly (0.02°/3sec or 0.02°/9sec) carried out with the fixed time mode (FT mode). To get the crystallographic properties from the precise diffraction patterns, we have performed the Rietveld refinements for all samples using Rietan-FP program.[54]

2.2.1.1 Rietveld Refinements[54]

Rietveld refinement is a method to obtain the precise crystallographic information from the relation between a structural model and an experimentally obtained diffraction data. In other words, the Rietveld refinement refines user-selected parameters to minimize the discrepancy between a model and an experimental pattern based on the hypothesized crystal structure. From the technique, we can refine various information about a crystal structure such as lattice parameters, fractional occupancy, atomic positions, and thermal parameters. Thus, it can be used to reasonably understand the transport behavior of both charged carriers and heat carrying phonon in crystal structure. On the other hand, for Rietveld refinement, a high quality experimental diffraction pattern, a structure model that makes chemical and physical sense, and a suitable peak/ background functions are required.

The weighting factor for pattern fitting is expressed as $S(x)$ consisting of statistical weight w_i, observed intensity y_i and calculated intensity $f_i(x)$.

$$S(x) = \sum_i w_i [y_i - f_i(x)]^2 = \sum_i (1/y_i)[y_i - f_i(x)]^2 \qquad (2\text{-}3)$$

In the crystallographic study, the R factor (Reliability factor) is a measure of the agreement between the experimental diffraction data and the crystallographic model. That is, it is a measure of how the refined structure predicts the observed data well. The goodness-of fit indicator and reliability indices for Bragg factor and structure factor are expressed as follows.

$$S = \frac{R_{wp}}{R_e} = \left\{ \frac{\sum_{i=1}^{N} w_i [y_i - f_i(x)]^2}{\sum_{i=1}^{N} w_i y_i^2} \right\}^{\frac{1}{2}} \cdot \left\{ \frac{(N-n)}{\sum_{i=1}^{N} w_i y_i^2} \right\}^{-\frac{1}{2}} \qquad (2\text{-}4)$$

$$R_B = \frac{\sum_K |I_0(h_K) - I(h_K)|}{\sum_K I_0(h_K)} \tag{2-5}$$

$$R_F = \frac{\sum_K \left\| F_0(h_K) \right| - |F(h_K)\right\|}{\sum_K |F_0(h_K)|} \tag{2-6}$$

2.2.2 Surface Microstructure and Elemental Analysis

The surface microstructure and chemical composition were characterized by the Field-Emission Scanning Electron Microscopy (FE-SEM) with the Energy Dispersive X-ray spectrometry (EDX). The schematic of the FE-SEM equipment is shown in Figure 2.4.
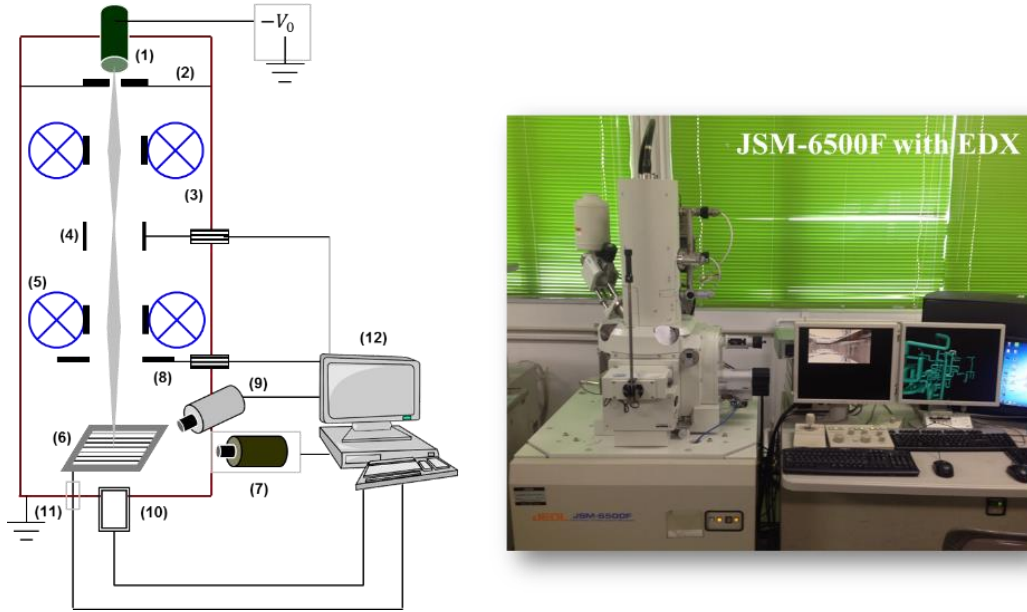

Figure 2.4 (Left) Schematic image of FE-SEM; (1) Incident electron source, (2) grounded electrode, (3) condenser lens, (4) beam deflection system, (5) objective lens, (6) specimen on a goniometric stage, (7) secondary electron detector, (8) backscattered electron detector, (9) X-ray spectrometer (EDX), (10) transmitted electron detector, (11) absorbed current measurement, (12) control unit and display screen [53]. (Right) The photo image of FE-SEM used in the present study.

In a typical FE-SEM, an electron source and multiple condenser lenses produce an incident electron beam whose fluxes at various angles are deflected by condenser lens. The beam detection system deflects the beam back across the optic axis. All the fluxes pass through the final objective lenses and strike the specimen at various points at a time. The emitted signals contain the back scattered electrons, low energy secondary electrons, characteristic X-rays, and luminescent radiations. Scanning electron micrographs and energy dispersive X-ray spectra are obtained by a scanning electron detector, and a characteristic X-ray detector, respectively.

2.2.3 Electrical Resistivity and Seebeck Coefficient

Both the electrical resistivity and the Seebeck coefficient of the samples have simultaneously been obtained from commercially available measurement system (ZEM-1, ULVAC) under the helium atmosphere as shown in Figure 2.5.
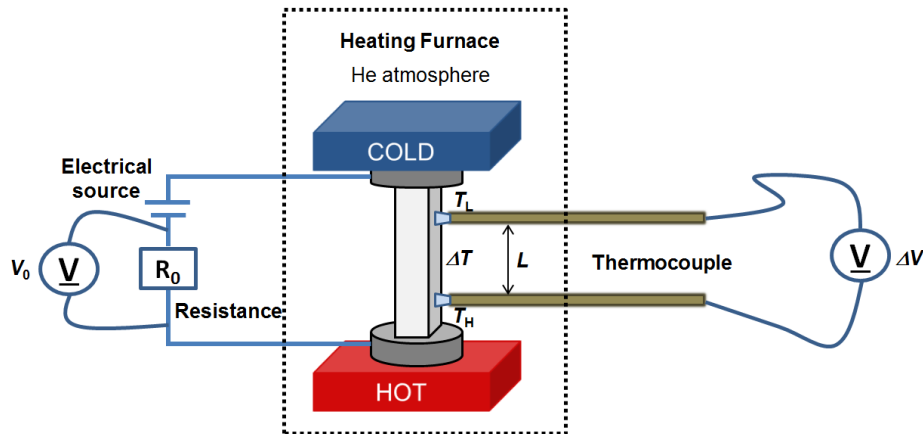
Figure 2.5 Schematic image for the electrical resistivity and Seebeck coefficient measurement system.

The electrical resistivity have been obtained by the standard four probe method. A thermocouple consisting of two probes was attached to the side surface of a sample to measure the voltage V. At the same time, the temperature was measured between two probes as T_H and T_L. Thus, the measuring temperature T would be

$$T = \frac{(T_H + T_L)}{2} \tag{2.7}$$

There is a voltage across a reference resistance R_0, which was connected in parallel with the sample, was measured as V_0. The V is the measured voltage between two probes contacted on the sample. The sample resistance (R_{sample}) would be

$$R_{sample} = \frac{V}{V_0} \times R_0 \tag{2.8}$$

During the measurement, the electric current applied to the sample is reversed in order to exclude the influence of the thermopower at the contact point between the probe and the sample. The electrical resistivity can be derived by measuring the resistance value of the sample and taking the dimensions into account as following:

$$\rho = R_{sample} \frac{A}{L} \tag{2.9}$$

where R_{sample}, A and L are is the sample resistance, cross-sectional area of the sample and L is the distance between the two thermocouples. The Seebeck coefficients (S) is obtained by the following

$$S = \frac{V}{\Delta T} \tag{2.10}$$

V is the Seebeck voltage developed between two thermocouples on the sample, across the direction of the temperature gradient. T_H and T_L are the measured absolute temperatures at the two points. The measurement was carried out by applying three temperature gradients of $\Delta T = 20, 30,$ and 40 K between two blocks at each temperature T, the average value of three data is used as the experimental value.

2.2.4 Carrier Concentration and Mobility

Hall measurement was carried out by van der Pauw method at room temperature using the magnetic field of 0.5 T.[55] Hall carrier concentration (n_H) and Hall mobility (μ_H) were estimated with the measured R_H under single parabolic band models and Hall factor of unity with following equations;

$$n_H = \frac{\gamma_H}{eR_H} \quad \text{and} \quad \mu_H = \frac{R_H}{\rho} \tag{2.11}$$

where R_H and ρ is the Hall coefficient and the resistivity, respectively, and γ_H is the Hall factor which is given by

$$\gamma_{\mathrm{H}} = \frac{3\sqrt{\pi}}{4} \frac{(2r+3/2)!}{\left[(r+3/2)!\right]^2} \qquad (2.12)$$

For acoustic deformation potential scattering r where $r = -1/2$, the hall factor becomes $\gamma_H = 1.18$, while for ionized impurity scattering where $r = 3/2$, we find $\gamma_H = 1.93$. Obviously the order of magnitude of γ_H is 1.

The Hall coefficient is given by the following equation using the magnetic field B, Hall voltage V, the current I, and the sample's thickness δ.

$$R_{\mathrm{H}} = \frac{|V_{23}|\delta}{I_{14}B} = \frac{\delta}{B} R_{12,34} \qquad (2.13)$$

Here, twice measurements give two resistances:

$$R_{12,34} = \frac{|V_{23}|}{I_{14}} \quad \text{and} \quad R_{23,41} = \frac{|V_{41}|}{I_{23}} \qquad (2.14)$$

The numbers indicate proves shown in Figure 2.7. Then, the resistivity is calculated from

$$\rho = \frac{\pi}{\ln 2} \delta \frac{R_{12,34} + R_{23,41}}{2} f \qquad (2.15)$$

The factor f depends on the ratio $R_{12,34}/R_{23,41}$ as shown in Figure. 2.6.
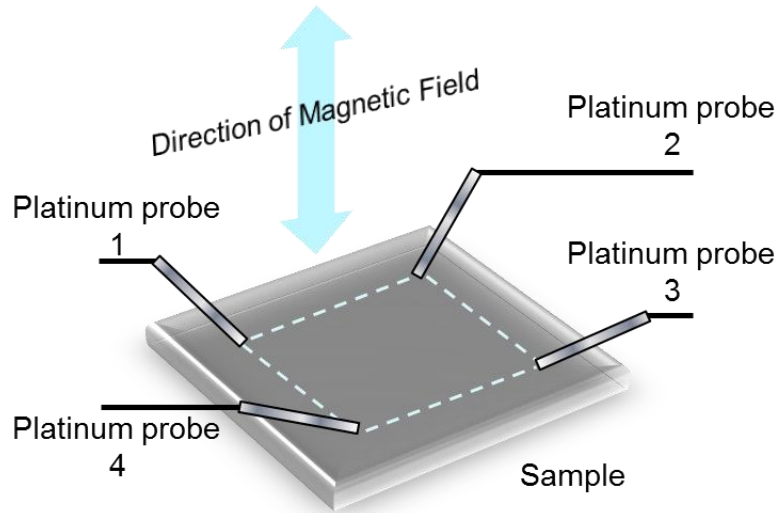
Figure 2.6 Schematic image of van der Pauw's method.

2.2.5 Thermal Conductivity

The thermal conductivity of the bulk samples was measured by the laser flash method which measures the thermal diffusivity (α) of the sample. The thermal conductivity is determined by

$$\kappa = \alpha D C_P \qquad (2.16)$$

where D and C_P are the density and the heat capacity of the bulk sample, respectively. The heat capacity (C_P) of the sample approaches the classical value $3nR$ of Durong-Petit at high temperature, i.e. above the Debye temperature, while C_P depends on the T^3 law of Debye at low temperature. Thus, in the present study, $C_P = 3nR$ is applied for the estimation of the heat capacity for the samples, where R is the gas constant and n is the number of atoms per a formula unit.[2]

The thermal diffusivity was measured three times at each temperature and the average value was used for the estimation. As shown in Figure 2.7, pulse laser causes the temperature change at the back surface of the sample and the changed temperature is detected by the infrared sensor. The sample surface was coated with graphite spray to impede the reflection of the pulse laser from the surface. The thermal diffusivity is estimated in the followings.[56]

When the initial temperature distribution in an insulated solid with the uniform thickness L is $T(x, 0)$, the temperature distribution at the elapse time t is given as following relation,

$$T(x,t) = \frac{1}{L}\int_0^L T(x,0)dx + \frac{2}{L}\sum_{n=1}^{\infty}\exp\left(\frac{-n^2\pi^2\alpha l}{L^2}\right)\cos\frac{n\pi x}{L}\int_0^L T(x,0)\cos\frac{n\pi x}{L}dx \qquad (2.17)$$

where α is the thermal diffusivity. If the pulse with the radiant energy Q is entered into the small depth g at the surface $x = 0$ for the insulated solid with the thickness L,
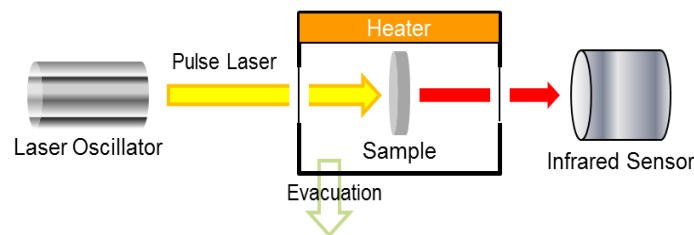

Figure. 2.7 Schematic image for the laser flash measurement.

temperature distribution at the instant is given by $T(x, 0) = Q/DC_g$ for $0 < x < g$ and $T(x, 0) = 0$ for $g < x < L$. With this initial condition, equation (2.17) can be written as following.

$$T(x,t) = \frac{Q}{DC_p L}\left[1 + 2\sum_{n=1}^{\infty}\cos\frac{n\pi x}{L}\frac{\sin(n\pi g/L)}{n\pi g/L}\exp\left(\frac{-n^2\pi^2\alpha l}{L^2}\right)\right] \tag{2.18}$$

Since the g is very small figure for opaque materials, it is following that $\sin(n\pi g/L) \approx n\pi g/L$. At the rear surface where $x = L$, the temperature gradient can be expressed as following.

$$T(L,t) = \frac{Q}{DC_p L}\left[1 + 2\sum_{n=1}^{\infty}(-1)^n\exp\left(\frac{-n^2\pi^2\alpha l}{L^2}\right)\right] \tag{2.19}$$

Two dimensionless parameters, V and ω can be defined as following relationships, where T_M represents the maximum temperature at the rear surface.

$$V(L,t) = T(L,t)/T_M \tag{2.20}$$

$$\omega = \pi^2\alpha l/L^2 \tag{2.21}$$

The combination of equations (2.19), (2.20) and (2.21) yields the equation (2.22).

$$V = 1 + 2\sum_{n=1}^{\infty}(-1)^n\exp\left(-n^2\omega\right) \tag{2.22}$$

Equation (2.22) is plotted in Figure 2.8. From equation (2.22) and Figure 2.8, thermal diffusivity α is deduced: when V is 0.5, ω is 1.38 and the following relationship is obtained.

$$\alpha = (1.38L^2/\pi^2 t_{1/2}) \tag{2.23}$$

The parameter $t_{1/2}$ is the time needed for a back surface to come to a half of the maximum temperature rise.

Without attempting a rigorous analysis, an effective temperature T_e is picked as the time average of the mean of the front and back surface reaches one-half of its maximum value. The dimensionless parameter $V(L,t)$ at the rear surface was given by equation (2.24). The dimensionless parameter $V(0,t)$ at the front surface obtained in a similar fashion is given by the following.

$$V(0,t) = 1 + 2\sum_{n=1}^{\infty}\exp(-n^2\omega) \tag{2.24}$$

The mean value of $V(L,t)$ and $V(0,t)$ is

$$\frac{V(0,t) + V(L,t)}{2} = 1 + 2\sum_{n=1}^{\infty}\exp(-4n^2\omega) \tag{2.25}$$

and the effective value of V is expressed as equation (2.26).

$$V_e = 1 + \frac{2}{\omega_{1/2}} \int_0^{\omega_{1/2}} \sum_{n=1}^{\infty} \exp(-4n^2\omega)d\omega$$

$$= 1 + \frac{2}{4(1.38)} \left[\sum_{n=1}^{\infty} \frac{1}{n^2} \left(1 - \exp(-4n^2 \times 1.38) \right) \right] = 1.6$$

(2.26)

Finally, the effective temperature is given by
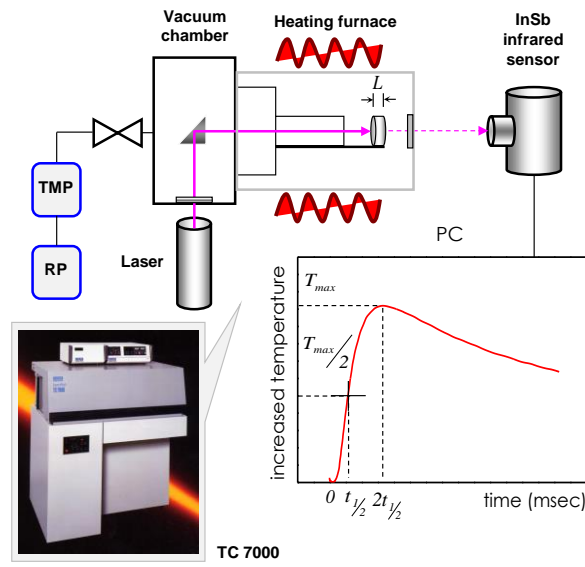
$$T_e = V_e T_M = 1.6 T_M$$

(2.27)

Figure 2.8 Schematic image of the laser flash method.

CHAPTER III

Thermoelectric Properties of Tl-filled *p*-type Skutterudites

The general composition of filled-skutterudites are XM_4Sb_{12}, where *X* is a filler atom in the cage-like void of unit cell, *M* is the transition metals such as Fe, Co, and Ni, etc. Compared to *n*-type filled skutterudites with excellent thermoelectric (TE) properties, *p*-type filled skutterudites still have poor TE properties. However, to make a powerful TE module, the performance of *p*-type materials have to be nearly equal to that of *n*-type materials. For the needs, we would be able to response by developing the *p*-type skutterudites. On the point of view, $FeSb_3$-based filled skutterudites is the most famous and promising *p*-type skutterudites as much as $CoSb_3$-based filled skutterudites as the *n*-type material. Through the simple valence electron counting, one can know that the $FeSb_3$ unit cell needs the additional electrons in order to be thermodynamically stable, because it has less electron than the valence electron number of the stable $CoSb_3$ unit cell in the same crystal structure, i.e., skutterudite structure. The stable undoped $FeSb_3$ can only be made as a thin film from the molecular beam epitaxy apparatus.[57] However, by filling the electropositive elements into the voids of skutterudite structures, the charge deficiency of $FeSb_3$ frame can be fully or partially compensated, which means that the $FeSb_3$-based skutterudites thermodynamically become stable.[17,31,58] In other words, The $FeSb_3$-based skutterudites would be able to consider as heavily doped *p*-type materials with holes as a majority carrier. For example, if a Thallium (Tl) atom are filled into the voids of $FeSb_3$-based skutterudite structures, it has the valence charge of +1 and compensates an excess hole by supplying an electron. The modification of crystal and electrical structures would influence on the behaviors of charge carriers and heat carrying phonon. Therefore, by control the filling content, one can adjust the electrical property as well as the thermal property by the rattling behavior.[24,58-60] Since, among the Group 13 elements, Tl is chemically close to the other heavy elements such as bismuth and, in other respects, similar with the elements of alkali-metal group, it is known as an unusual element.[41] In particular, the large mass of Tl would lead to low vibrational frequencies *via* the classical relation $\omega = \sqrt{k/m}$ where ω is the vibrational frequency and k is the restoring force constant for the bond strength between the filler and the surrounding Sb atoms. The low frequency vibration of fillers would be beneficial

for heat carrying phonon scattering.[21,58] Thus, Tl have been a research target and, in the case of n-type Tl-filled skutterudite, A. Harnwunggmoung et al. have reported the zT of 0.9 for $Tl_{0.25}Co_4Sb_{12}$ at 600 K.[16,36,39,61,62] However, the reports for p-type Tl-filled skutterudites have been limited. As mentioned, for the application on the module, the balance of performances for p-type and n-type materials is significantly important. So we need to investigate the p-type Tl filled skutterudites with the high performance.

In this chapter, I have studied the crystallographic and TE properties for two series of Tl-filled FeSb$_3$-based p-type skutterudites, $Tl_xFe_{2.5}Ni_{1.5}Sb_{12}$ and $Tl_xFe_{1.5}Co_{2.5}Sb_{12}$.[63,64]

3.1 $Tl_xFe_{2.5}Ni_{1.5}Sb_{12}$ system[63]

The majority carrier (hole) concentration of FeSb$_3$-based p-type skutterudites could be adjusted by partially replacing iron (Fe) with nickel (Ni), since Fe has two less electrons than Ni. As shown in Figure 3.1, the replacement of Fe by equimolar amounts of Ni, might yield the ternary skutterudite compound that is iso-electronic to the binary CoSb$_3$, the prototype of skutterudite.[60] Furthermore, Ni and Fe are cheaper than Co, which is an important issue in respect to the mass production.
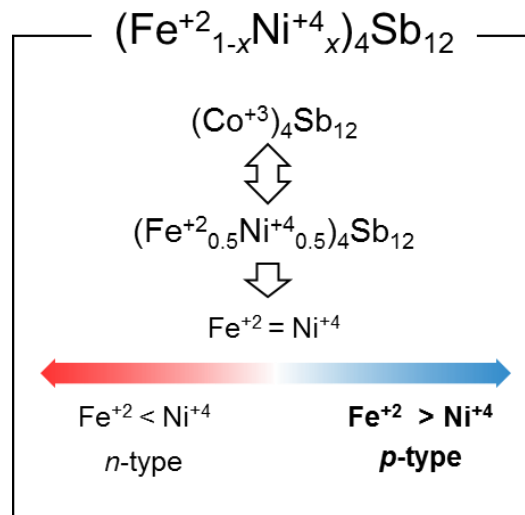
Figure 3.1 Schematic of the isoelectronic substitution of both Fe and Ni in the skutterudite structures.

Table 3.1 Predicted hole number per formula unit of $Tl_xFe_{2.5}Co_{1.5}Sb_{12}$

$Tl_xFe_{2.5}Ni_{1.5}Sb_{12}$ ($0 \leq x \leq 1.0$)						
Tl contents	$x = 0.0$	$x = 0.2$	$x = 0.4$	$x = 0.6$	$x = 0.8$	$x = 1.0$
Predicted no. holes per formula unit	1.0	0.8	0.6	0.4	0.2	0

As shown in Table 3.1, the addition of Tl for $Fe_{1-x}Ni_xSb_{12}$ enables to adjust the carrier concentration by gradually compensating the excessive charge. According to the background, we have investigated the sample with composition $Tl_xFe_{2.5}Ni_{1.5}Sb_{12}$ ($x = 0, 0.2, 0.4, 0.6, 0.8,$ and 1.0).

3.1.1 Experimental Details

The synthesis of the polycrystalline samples of $Tl_xFe_{2.5}Ni_{1.5}Sb_{12}$ was prepared from the starting materials, chunks of Tl (5N), Fe (3N), Ni (3N), and Sb (3N). The precursors have carefully been weighed out with the stoichiometric ratio and loaded in the silica tubes. The silica tubes were sealed under vacuum using an oxygen/hydrogen torch and transferred in the vertical furnace. The silica tubes have been heated with the melting condition (1323 K, 2 K/min, 72 hr holding) and then rapidly quenched by putting the heat treated silica tubes into cold water. The ingots consisting of unstable phases have been annealed for 14 days at 873 K in order to obtain the thermodynamically stable phases. The as-prepared ingots have been finely reduced to powder. The as-prepared powders were sintered using hot-press apparatus at 823 K for 2 hrs by applying the pressure of 45 MPa under flowing Ar. Column and disc shaped bulk samples were prepared for the characterization of microstructure and TE properties.

The X-ray diffraction (XRD) patterns have been collected from the commercial equipment (Ultima IV, Rigaku) with Cu *Ka* radiation at room temperature. The lattice parameters for all samples were estimated from the least-squares fitting to 2θs, using the standard Si, the external reference material, by utilizing PDXL, Rigaku's diffraction software. The occupancies of elements in matrix phases have been obtained with Rietveld refinement by using Rietan-FP program.[54] The fine-structure and quantitative element analysis for samples has been obtained at room temperature from the Field Emission Scanning Electron Microscopy (FE-SEM; JEOL, JSM-6500F) with the Energy Dispersive X-ray (EDX) spectroscopy under

the vacuum. The Seebeck coefficient S and the electrical resistivity ρ have been obtained by measuring the samples with the cylindrical shape in commercial equipment (ZEM-1, ULVAC) in He gas atmosphere. The thermal diffusivity α obtained on the laser flash method by measuring the samples with the disc shape in commercial equipment (ULVAC, TC-7000) under vacuum. The thermal conductivity $\kappa = \alpha C_p d$ have calculated from the conventional relation $\kappa = \alpha C_p d$, where C_p is the heat capacity from the Durong-Petit model, $C_p = 3nR$, and the d is the density. The densities for the samples have been obtained through the manually taken dimensions and weights.

3.1.2 Results and Discussion

The powder XRD pattern of the polycrystalline sample of $Tl_x Fe_{2.5} Ni_{1.5} Sb_{12}$ ($x = 0, 0.2,$ 0.4, 0.6, 0.8, and 1.0) are shown in Figure 3.2. Most of all peaks in XRD patterns have been identified as the peaks obtained from a skutterudite phase as a major phase. However, the XRD patterns shows the peaks of $(Fe, Ni)Sb_2$ and elemental Sb as secondary phases for the samples with $x = 0, 0.2,$ and 0.4, where their peak intensities increase with decreasing x. On the other hand, the XRD patterns for the samples with $x = 0.8$ and 1.0 shows the peaks of Sb phase as a secondary phase and the peak intensity slightly increased with decreasing x. The $x = 0.6$ sample is almost the single phase of the skuttuerudite structure although it contains small amount of Sb phase. The intensity ratio of (211) and (310) peaks for a skutterudite matrix phase increased as Tl content decreased, which is the indication of Tl-filling. It's well known that these peaks gradually become smaller as the voids of the skutterudites are filled by the filling atoms.[17,65] In Table 3.2, the lattice parameter increased with increasing x from $x = 0$ to $x = 0.8$ and after that it remains constant. Therefore, it can be considered the Tl filling limit for the matrix phases would be between $x = 0.6$ and 0.8. All samples had the high density and the relative density of the $x = 0.6$ sample which was nearly close to the skutterudite single phase indicated above 98% T.D. (theoretical density).
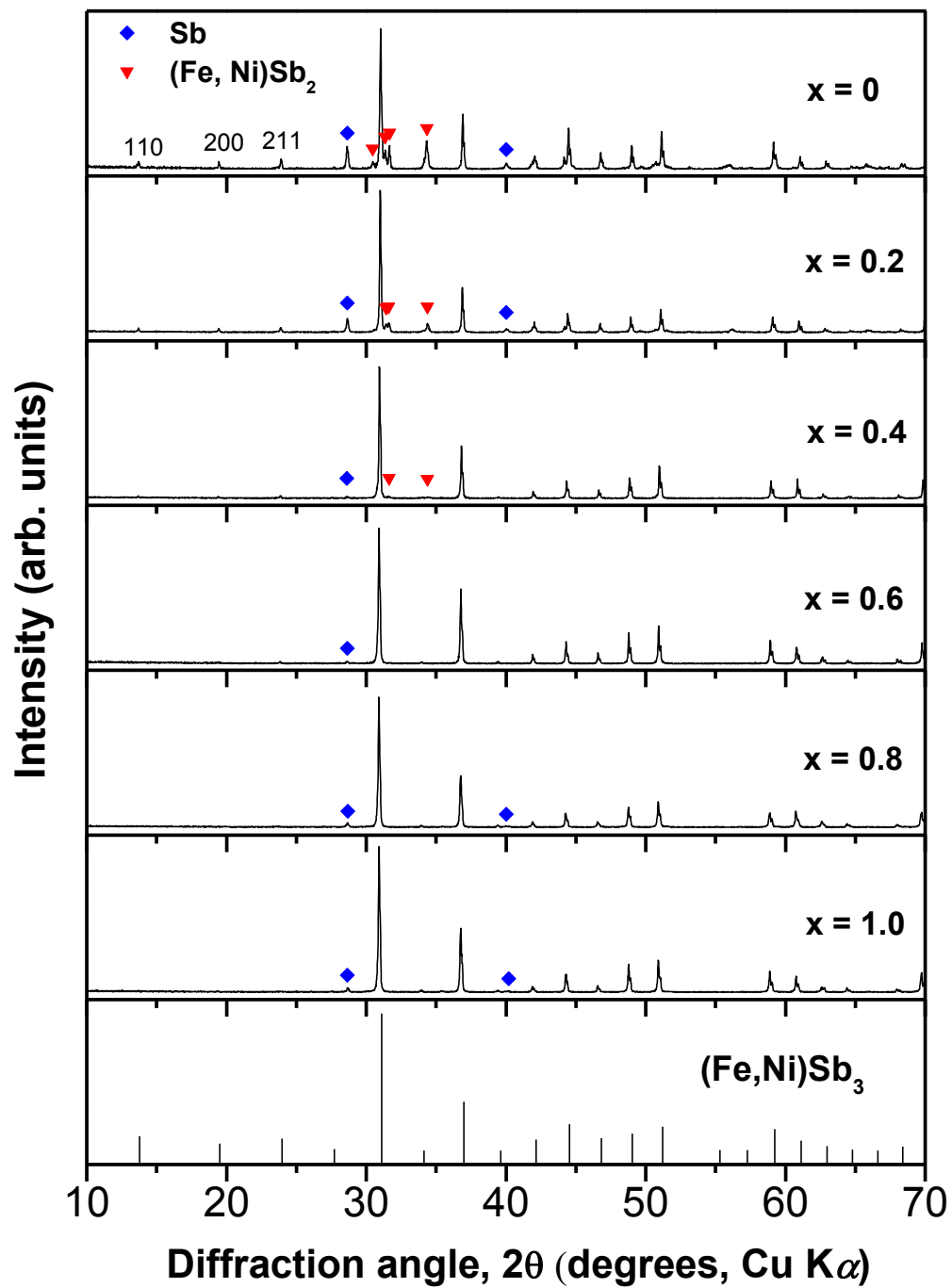
Figure 3.2 Powder XRD patterns of polycrystalline samples with the nominal composition $Tl_xFe_{2.5}Ni_{1.5}Sb_{12}$ ($x = 0$, 0.2, 0.4, 0.6, 0.8, and 1.0).

Table 3.2 Lattice parameter a, and density d, and Hall coefficient R_H for polycrystalline samples of $Tl_x Fe_{2.5} Ni_{1.5} Sb_{12}$ ($x = 0$, 0.2, 0.4, 0.6, 0.8 and 1.0).

x	a (nm)	d (g cm^{-3})	d (% T.D.)	R_H (10^{-8}m^{3}C^{-1})
0	0.9095	7.53	-	5.67
0.2	0.9100	7.56	-	3.03
0.4	0.9126	7.58	-	1.65
0.6	0.9135	7.66	98	3.85
0.8	0.9140	7.81	-	-
1.0	0.9139	7.83	-	-

Table 3.3 Chemical composition at the skutterudite phase of the polycrystalline samples with the nominal compositions $Tl_x Fe_{2.5} Ni_{1.5} Sb_{12}$ ($x = 0$, 0.2, 0.4, 0.6, 0.8 and 1.0), determined by quantitative EDX analysis. All compositions indicate the mean values obtained by repeating the point analysis over 10 times. (Measured compositions were calculated on the basis of the Sb content.)

Nominal composition	Fe/Ni ratio	Chemical composition (at.%)				Measured composition
		Tl	Fe	Ni	Sb	
$Fe_{2.5}Ni_{1.5}Sb_{12}$	1.32	-	14.3	10.7	75.0	$Fe_{2.29}Ni_{1.71}Sb_{12}$
$Tl_{0.2}Fe_{2.5}Ni_{1.5}Sb_{12}$	1.43	1.2	14.9	10.4	73.5	$Tl_{0.20}Fe_{2.43}Ni_{1.70}Sb_{12}$
$Tl_{0.4}Fe_{2.5}Ni_{1.5}Sb_{12}$	1.54	2.7	15.0	9.7	72.6	$Tl_{0.45}Fe_{2.48}Ni_{1.60}Sb_{12}$
$Tl_{0.6}Fe_{2.5}Ni_{1.5}Sb_{12}$	1.56	3.3	14.6	9.4	72.7	$Tl_{0.54}Fe_{2.41}Ni_{1.55}Sb_{12}$
$Tl_{0.8}Fe_{2.5}Ni_{1.5}Sb_{12}$	1.40	3.8	14.0	10.0	72.2	$Tl_{0.63}Fe_{2.33}Ni_{1.66}Sb_{12}$
$Tl_{1.0}Fe_{2.5}Ni_{1.5}Sb_{12}$	1.44	4.0	14.2	9.9	71.9	$Tl_{0.67}Fe_{2.37}Ni_{1.65}Sb_{12}$
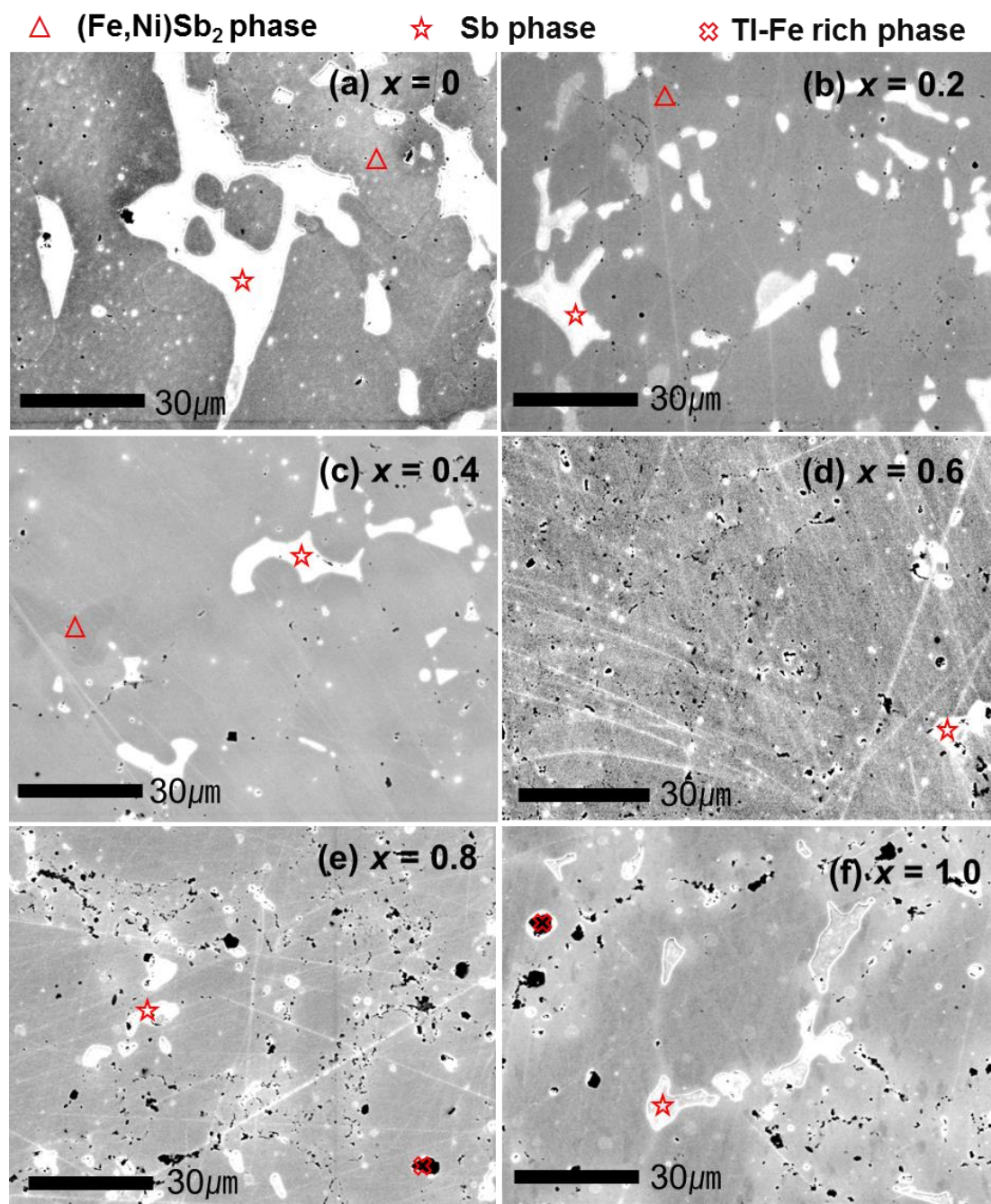
Figure 3.3 FE-SEM image of the samples with the nominal composition $Tl_xFe_{2.5}Ni_{1.5}Sb_{12}$ ($x =$ 0, 0.2, 0.4, 0.6, 0.8, and 1.0).
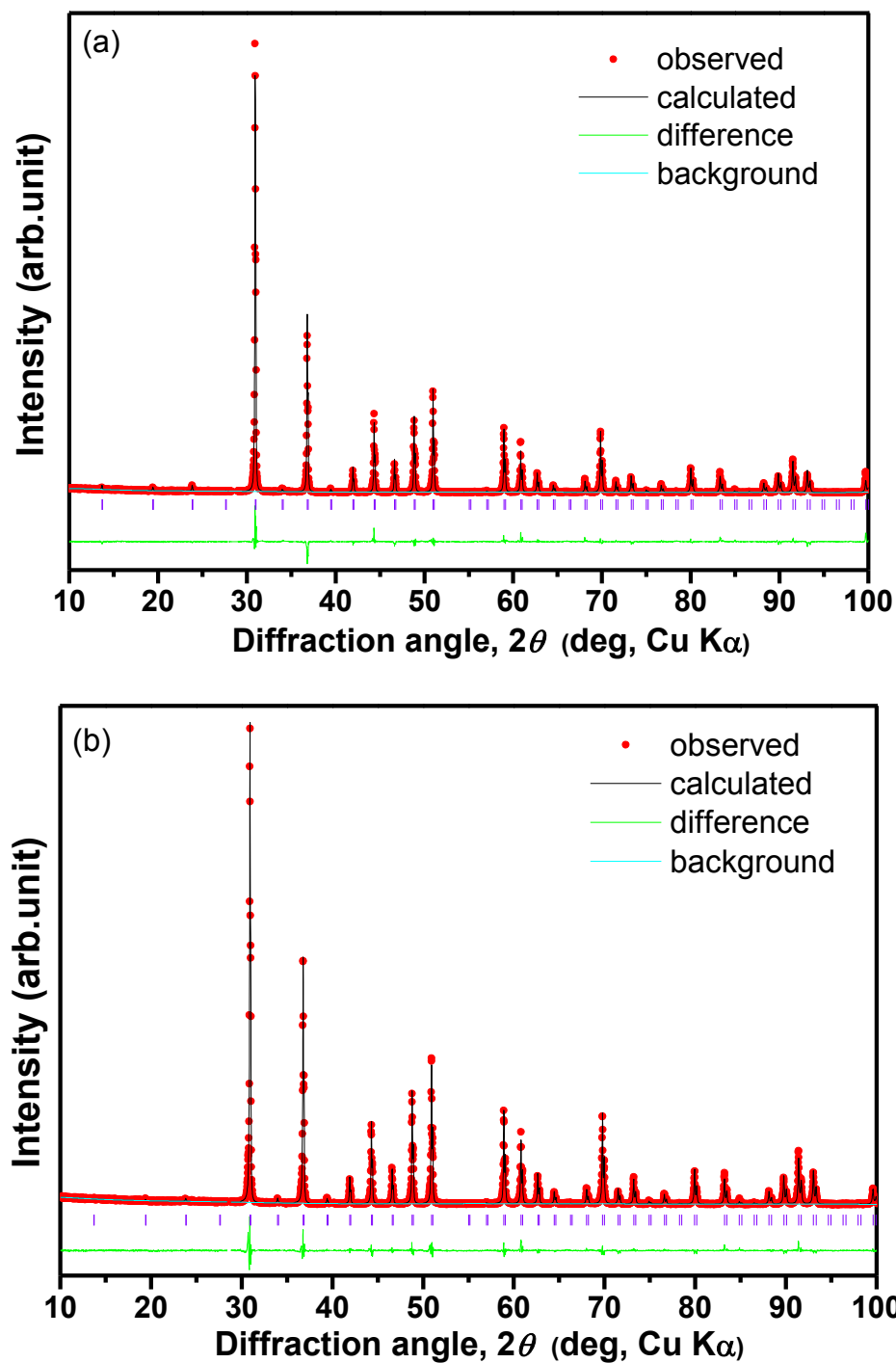
Figure 3.4 Powder XRD patterns of the samples with the nominal composition (a) $Tl_{0.4}Fe_{2.5}Ni_{1.5}Sb_{12}$ and (b) $Tl_{0.6}Fe_{2.5}Ni_{1.5}Sb_{12}$ showing observed, calculated, background, and difference curves at room temperature. The expected peak positions are marked with vertical ticks.
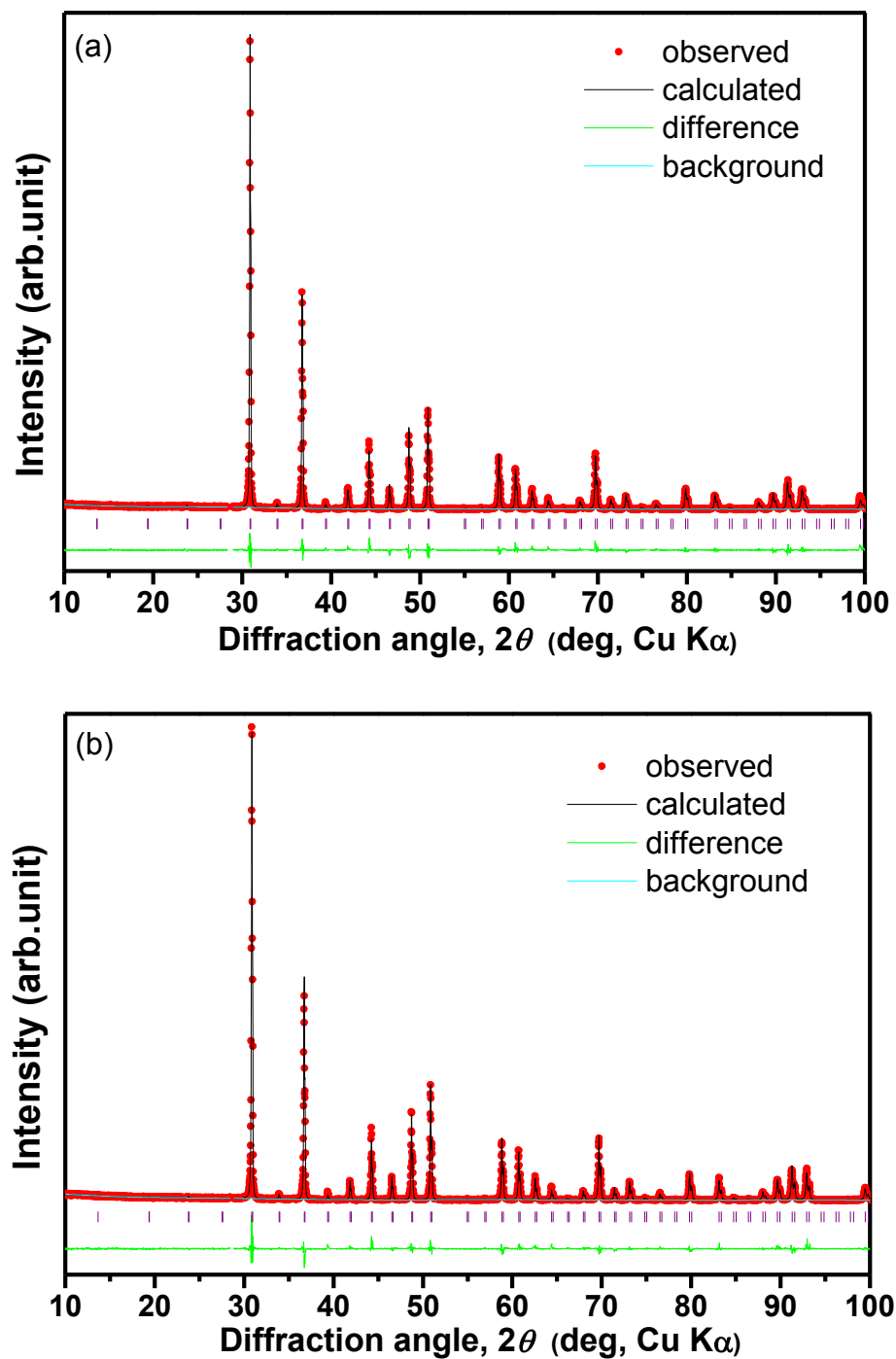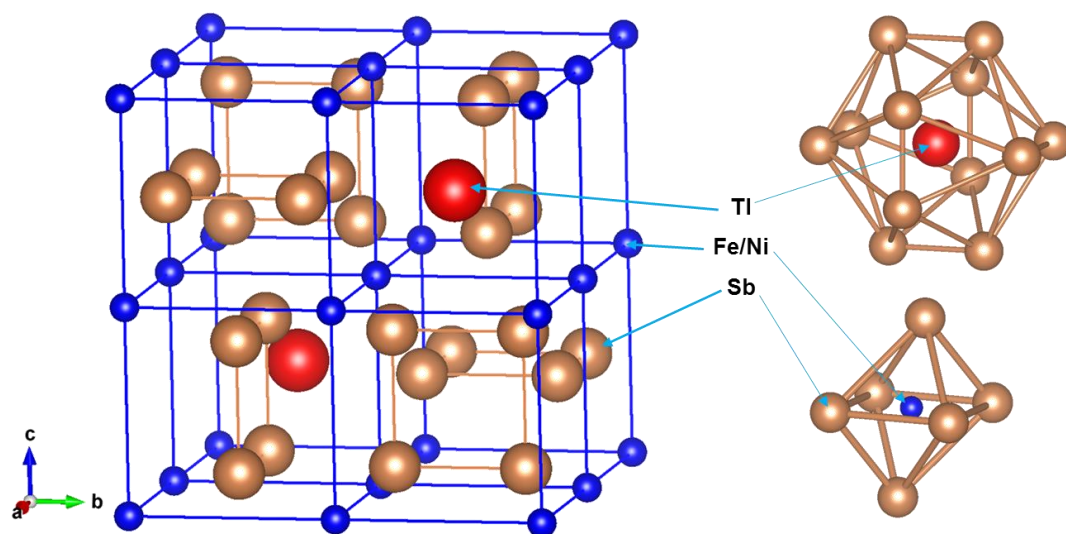
Figure 3.5 Powder XRD patterns of samples with the nominal composition (a) $Tl_{0.8}Fe_{2.5}Ni_{1.5}Sb_{12}$ and (b) $Tl_{1.0}Fe_{2.5}Ni_{1.5}Sb_{12}$ showing observed, calculated, background, and difference curves at room temperature. The expected peak positions are marked with vertical ticks.

Figure 3.6 Crystal structure of $Tl_xFe_{2.5}Ni_{1.5}Sb_{12}$.(left) Tl atoms on the 2a site and Fe/Ni atoms on the 8c site are surrounded by 12 Sb atoms and 6 Sb atoms, respectively.(right)

Figure 3.3 shows the secondary electron image acquired from the FE-SEM for the polycrystalline samples with nominal composition $Tl_xFe_{2.5}Ni_{1.5}Sb_{12}$ ($x = 0, 0.2, 0.4, 0.6, 0.8$, and 1.0). One can see that the content of secondary phases qualitatively has been changed as the Tl content. From the FE-SEM/EDX analysis, it was confirmed that the samples with $x = 0$, 0.2, and 0.4 show two secondary phases which are $(Fe,Ni)Sb_2$ phase and the Sb phase. On the other hand, the samples with $x = 0.6, 0.8$, and 1.0 show one secondary phase of the Sb phase. Furthermore, in the grain boundaries, there are the small black regions consisting of Tl-Fe rich system which was formed because the solubility limit for the crystal phases. These results were well consistent with the result of the X-ray patterns. Additionally, as shown in Table 3.3, the chemical composition of the matrix phase was quantitatively estimated by the EDX analysis. Although a Fe/Ni ratio in a skutterudite phase was fixed for the nominal composition of all samples, it was modified as increasing Tl content. In particular, up to $x = 0.6$, the increase of the nominal Tl content leaded to the increase of the Fe/Ni ratio as well as the increase of Tl filling fraction in the skutterudite phases, which means that the relative content of the stable skutterudite phases increased with increasing Tl by the excessive charge compensation of Tl. However, as increasing Tl more, the Fe/Ni ratio decreased, while the Tl increased as ever. The composition dependence would be described in the part of the electrical property again.

However, the chemical compositions obtained from EDX analysis include an uncertainty of several percentage and thus, in order to correct compositions, it needs to be compared to those obtained from other precise techniques. Accordingly, the Rietveld refinement for the XRD patterns have been carried out.

Table 3.4 Rietveld refinement result for the samples with the nominal composition $Tl_xFe_{2.5}Ni_{1.5}Sb_{12}$ (x = 0.4, 0.6, 0.8, and 1.0). [Atomic positions: Tl, 2a (0, 0, 0); Fe/Ni, 8c (1/4, 1/4, 1/4); Sb, 24g (0, y, z). Fe/Ni ratios are obtained from Table 2.]

Nominal composition	$Tl_{0.4}Fe_{2.5}Ni_{1.5}Sb_{12}$	$Tl_{0.6}Fe_{2.5}Ni_{1.5}Sb_{12}$	$Tl_{0.8}Fe_{2.5}Ni_{1.5}Sb_{12}$	$Tl_{1.0}Fe_{2.5}Ni_{1.5}Sb_{12}$
Composition obtained from Rietveld	$Tl_{0.39}Fe_{2.48}Ni_{1.60}Sb_{12}$	$Tl_{0.54}Fe_{2.41}Ni_{1.55}Sb_{12}$	$Tl_{0.61}Fe_{2.33}Ni_{1.66}Sb_{12}$	$Tl_{0.65}Fe_{2.37}Ni_{1.65}Sb_{12}$
Space group	$Im\bar{3}$ (#204)			
Radiation	Cu Kα (1.54056 Å)			
2θ range (deg.)	10 ~ 100			
Step width (deg.)	0.02			
Counting time (s/step)	9			
U_{iso} (Å^2) for Tl	0.0160	0.0160	0.0160	0.0160
U_{iso} (Å^2) for Fe/Ni	0.0055	0.0047	0.0024	0.0056
U_{iso} (Å^2) for Sb	0.0060	0.0060	0.0060	0.0060
y (Sb)	0.8405	0.8415	0.8414	0.8418
z (Sb)	0.6620	0.6638	0.6624	0.6626
Reliablility factors				
R_B	7.46	3.93	3.77	4.64
R_F	5.13	4.61	4.03	3.98
S	1.62	1.49	1.55	1.47

B.C. Chakoumakos et al. reported on the crystallographic response of fillers in crystal structures of Tl-filled skutterudites through the Rietveld refinement performed using the data obtained from the neutron powder diffraction methods.[15] Based on the information, Rietveld refinements have been performed as following two assumptions. Firstly, the U_{iso} values, the atomic displacement parameter, of Tl and Sb were fixed as that for Tl in $Tl_{0.75}Co_3FeSb_{12}$ reported by B.C. Chakoumakos et al..[15] Secondly, the Fe/Ni ratio was obtained from the quantitative EDX result for the skutterudite matrix phase in Table 3.3. As shown in Figures 3.4 and 3.5, the calculated values is well consistent with the observed ones, though, in Figure 3.4 (a), the sample with nominal composition $Tl_{0.4}Fe_{2.5}Ni_{1.5}Sb_{12}$ has a little discrepancy. One can also confirm the same trend for the reliability factors in Table 3.4. Figure 3.6 shows the crystal structure of the calculated filled-skutterudites.

Table 3.4 shows the result of the Rietveld refinement for the skutterudite matrix phases with the nominal composition $Tl_xFe_{2.5}Ni_{1.5}Sb_{12}$ (x = 0, 0.2, 0.4, 0.6, 0.8, and 1.0). The result indicates that the Tl-filling fractions were similar with that of the measured compositions in Table 3.3 and increased with increasing nominal Tl content. In particular, for the sample with x = 0.4, the Rietveld refinement derived the reasonable Tl filling fraction compared to the overestimated EDX value. The increase of lattice parameter attributed to the increase of Tl filling fraction, although the lattice parameter of the sample with x = 1.0 was smaller than that of the sample with x = 0.8. It would be related with the increase of the Fe/Ni ratio.
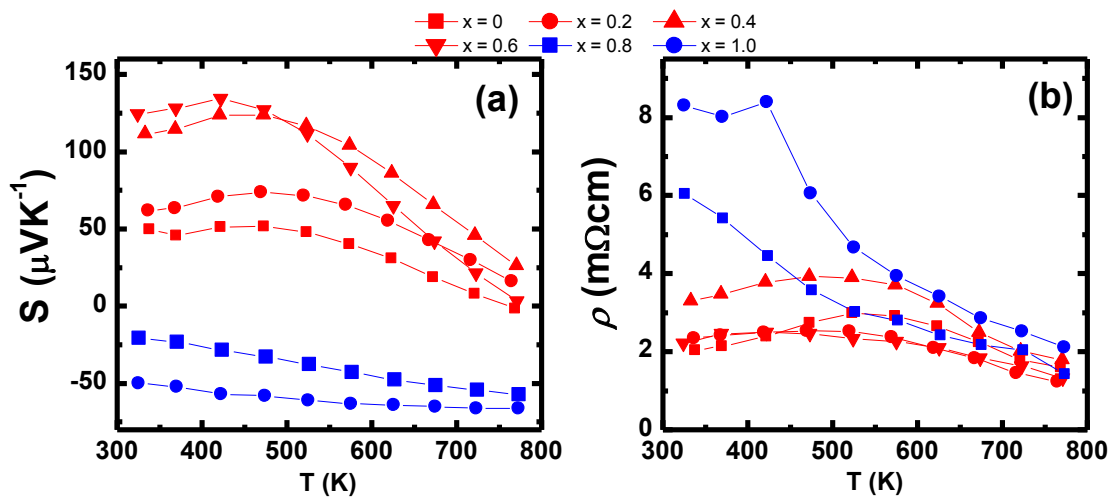

Figure 3.7 (a) Seebeck coefficient S and (b) electrical resistivity ρ as a function of temperature for polycrystalline samples with nominal composition $Tl_xFe_{2.5}Ni_{1.5}Sb_{12}$ (x = 0, 0.2, 0.4, 0.6, 0.8, and 1.0).

The S and ρ as a function of temperature for polycrystalline samples with nominal composition $Tl_xFe_{2.5}Ni_{1.5}Sb_{12}$ ($x = 0$, 0.2, 0.4, 0.6, 0.8, and 1.0) is shown in Figure 3.7. The samples with $x = 0$, 0.2, and 0.4 showed the positive S, which means p-type conduction. The absolute S values increased with increasing the Tl content up to $x = 0.6$, which was because the hole was compensated by Tl-filling. On the other hand, the samples with $x = 0.8$ and 1.0 showed the negative S, which means n-type conduction. Although, as shown in Figure 3.1, we firstly designed the p-type materials for all samples, the samples with $x > 0.6$ were the n-type materials. It can be simply comprehended from the actual composition obtained from EDX-Rietveld analyses. By counting the valence electrons for the actual compositions, we can know that the samples with $x = 0$, 0.2, 0.4, 0.6, 0.8, and 1.0 have the hole number of 0.58, 0.14, 0.18, 0.43, 0.07, and -0.02 (the minus figure means the electron number) per formula unit, respectively. Therefore, it can be considered that the samples with $x > 0.6$ might be the n-type skutterudites because of the increase of both Tl filling fraction in the voids and Ni contents in the matrix frame as the electron donors. For the p-type samples with $x \leq 0.6$, the S values increases with increasing Tl filling fraction and have the maximum values between 400 K and 500 K. The temperature with the maximum S is the onset of bipolar diffusion which seems to be shifted left due to the decrease of the hole with increasing Tl filling fraction. It would be the reason to promote the intrinsic transport behavior by minority carriers (in this case, electrons). From the simple principle, the Goldsmid-Sharp band gap (E_g) can be discretely estimated from the following equation.[66]

$$E_g = 2eS_{max}T_{max} \tag{3.1}$$

Where the e is the electron charge, the S_{max} is a maximum S at an onset point, and T_{max} is the corresponding temperature. Although, in the recent report, Z. M. Gibbs et al. found that it is not valid for the materials with $E_g < 10\,k_BT$, it is still effective to understand the carrier transport property.[64,67-69] From the relation, E_g values of the samples with $x = 0.2$, 0.4, and 0.6 were approximately gotten as 0.07, 0.10, and 0.11 eV, respectively, which were smaller than the values of 0.2, 0.37, and 0.42 for Yb-, Ca-, and Sr-filled Fe_3NiSb_{12}.[69] According to the band structure calculation by R. Liu et al., the valence band edge corresponds to Sb $5p$ state and the conduction band edge is triple degenerated by $3d$ states of transition metals and Sb $5p$ state. Compared with Co substitution, the relatively low energy level of Ni $3d$ state used to push the bottom of the conduction band down, which might lead to the reduction of the E_g.[26]

As shown in Figure 3.7 (b), the ρ increased with increasing the Tl content up to $x = 0.6$ because the hole concentration decreased due to the increase of Fe/Ni ratio. In the case of the samples with $x > 0.6$, since their hole was over-compensated by both low Fe/Ni ratio and high Tl filling fraction, the excessive electrons became the majority carrier. In other words, one can think that the Fermi level of the samples with $x > 0.6$ put into the conduction band. Therefore, it is considered that the high ρ resulted from the Fermi level close to conduction band edge. The reduced carrier concentration for the samples with $x > 0.6$ is also supported by the as-counted hole numbers for actual compositions of skutterudite matrix phases. On the other hand, as the other important reason for the high ρ, we can consider that the secondary phases such as (Fe,Ni)Sb$_2$ and Sb phases would have the side effect for the transport properties of both charge carrier and phonon.
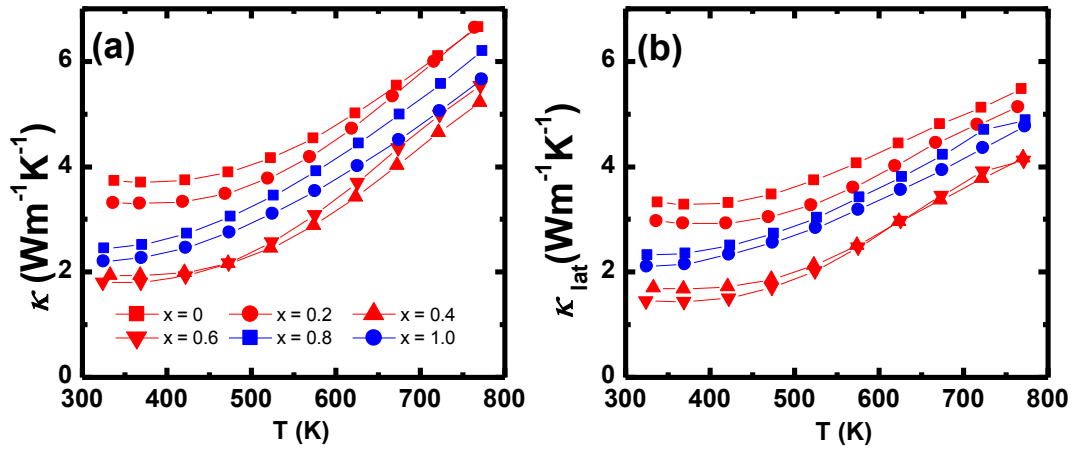
Figure 3.8 (a) Thermal conductivity κ, (b) lattice thermal conductivity κ_{lat} as a function of temperature for polycrystalline samples with nominal composition Tl$_x$Fe$_{2.5}$Ni$_{1.5}$Sb$_{12}$ ($x = 0$, 0.2, 0.4, 0.6, 0.8, and 1.0).

Figure 3.8 (a) and (b) shows the thermal conductivity κ and the lattice thermal conductivity κ_{lat} as a function of temperature, respectively. The κ_{lat} was calculated by using the Wiedemann-Franz law, i.e. $\kappa_{lat} = \kappa - LT\rho^{-1}$, where L is the Lorentz number (2.45×10^{-8} W Ω K^{-2}). Within the same conduction type, the κ_{lat} decreases with increasing Tl content, which resulted from the rattling effect of Tl filled into the voids of skutterudite phases. On the other hand, considering the actual compositions obtained from EDX-Rietveld refinements, one can understand that the Fe/Ni ratio is an important phonon scattering factor as much as the rattling behavior of the Tl filled into voids.[16,61] In particular, although the samples with $x > 0.6$ have

the most Tl filling fraction, they show lower κ_{lat} than the sample with $x = 0.4$ due to the relatively low Fe/Ni ratio.
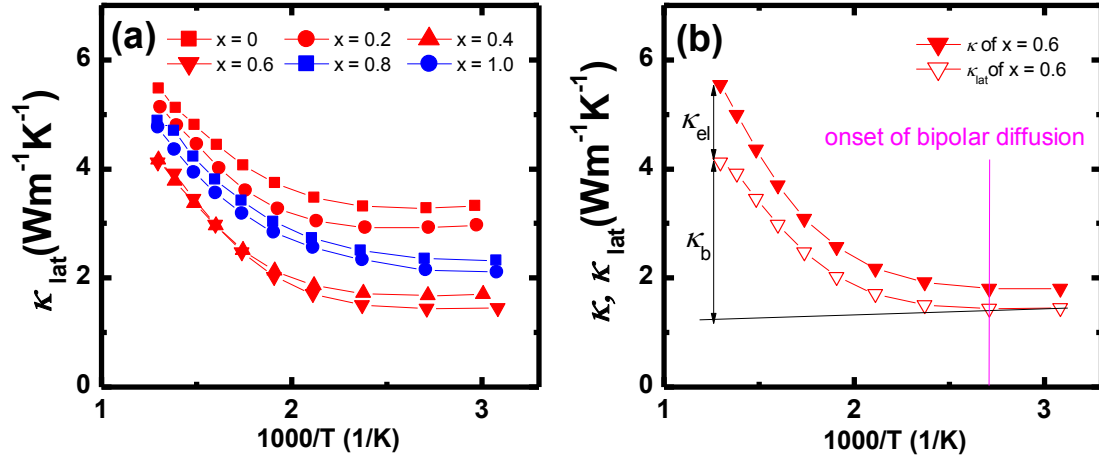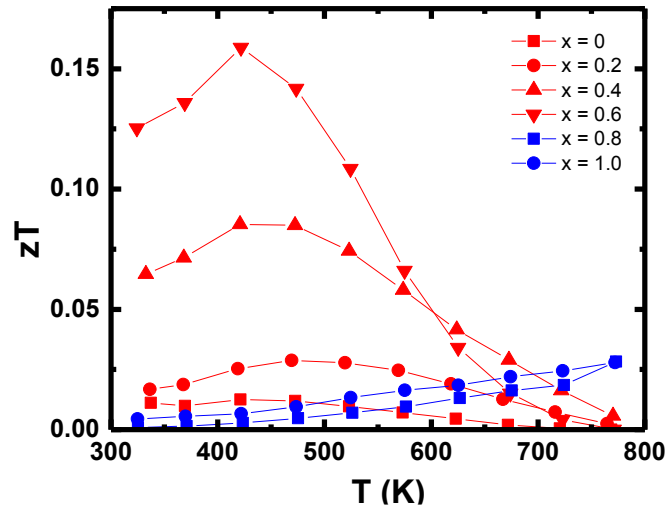

Figure 3.9 (a) κ_{lat} and (b) κ, κ_{lat} as a function of inverse temperature for polycrystalline samples with nominal composition $Tl_xFe_{2.5}Ni_{1.5}Sb_{12}$ ($x = 0$, 0.2, 0.4, 0.6, 0.8, and 1.0).

Figure 3.10 Dimensionless figure of merit zT as a function of temperature for polycrystalline samples with nominal composition $Tl_xFe_{2.5}Ni_{1.5}Sb_{12}$ ($x = 0$, 0.2, 0.4, 0.6, 0.8, and 1.0).

Figure 3.9 (a) and (b) shows κ_{lat} and κ, κ_{lat} as a function of inverse temperature, respectively. It shows that all samples have the considerable contribution of the bipolar

diffusion by the intrinsic excitation. The bipolar diffusion contribution in thermal conductivity can be expressed as

$$\kappa_B = \frac{\sigma_e \sigma_h}{\sigma_e + \sigma_h} \left(S_e - S_h \right)^2 T \tag{3.2}$$

Where the subscript e and h are the electron and hole, respectively.[24] Therefore, above the temperature corresponding to the onset of bipolar diffusion, total thermal conductivity is consisting of three contributions, carrier, lattice, and bipolar diffusion.

Finally, Figure 3.10 shows dimensionless figure of merit zT as a function of temperature. The sample with $x = 0.6$ exhibited the best zT values among all samples and the maximum zT value was 0.16 at 422 K.

3.1.3 Summary

In this study, polycrystalline samples of $Tl_x Fe_{2.5} Ni_{1.5} Sb_{12}$ ($x = 0$, 0.2, 0.4, 0.6, 0.8, and 1.0) were prepared. Their crystallographic properties were precisely characterized from the FE-SEM/EDX and Rietveld refinements. Based on the techniques, their TE properties were studied in the temperature range from 300 K to 773 K. The Tl filling fraction increased with increasing the nominal Tl content and the Tl filling limit was 0.65 for the sample with nominal composition $Tl_{1.0}\ Fe_{2.5} Ni_{1.5} Sb_{12}$ though it indicated the n-type material. The increase of Tl filling fraction contributed to the stabilization of the crystal structure by the compensation of excessive charge, which leaded to the enhancement of the carrier transport property and the heat carrying phonon scattering. Furthermore, it was confirmed that the Fe/Ni ratio have a strong influence on the heat carrying phonon scattering as well as the adjustment of hole concentration. In the present study, the optimal Tl ratio was $x = 0.6$. So the maximum zT value was 0.16 at 422 K obtained for the sample of $Tl_{0.6} Fe_{2.5} Ni_{1.5} Sb_{12}$.

3.2 $Tl_xFe_{1.5}Co_{2.5}Sb_{12}$ system[64]

It is well known that the $(Fe,Co)Sb_3$-based p-type skutterudites are most promising materials in terms of applications because they show the stable and high performances compared to the other p-type skutterudites.[24,27,58,70-73] Furthermore, the reports of the thermoelectric properties for group 13 elements-filled $(Fe,Co)Sb_3$-based p-type skutterudites have been limited.[42,59] Thus, it need to be studied more. Based on the simple valence electron counting scheme as done in Chapter 3.1, one can predict the carrier concentration by counting the valence charge of each element, which is so useful for the design the nominal compositions of skutterudites as well as other Zintl compounds.[14,63,69] The Fe substitution for Co in $CoSb_3$- based skutterudites would lead to p-type materials with hole as a majority carrier because one Fe atom has smaller one electron than one Co atom. The concentration of the hole can be modified by controlling the Fe/Co ratio. Additionally, the Fe is even cheaper than Co, which is beneficial for mass production.

Table 3.5 Predicted hole number per formula unit of $Tl_xFe_{2.5}Co_{1.5}Sb_{12}$

$Tl_xFe_{1.5}Co_{2.5}Sb_{12}$ ($0 \leq x \leq 0.7$)						
Tl contents	$x = 0.0$	$x = 0.2$	$x = 0.4$	$x = 0.5$	$x = 0.6$	$x = 0.7$
Predicted no. holes per formula unit	1.5	1.3	1.1	1.0	0.9	0.8

As shown in Table 3.5, the addition of Tl for $Fe_{1-x}Co_xSb_{12}$ enables to adjust the carrier concentration by gradually compensating the excessive charge. In this chapter, according to the background, we have investigated the sample with composition $Tl_xFe_{1.5}Co_{2.5}Sb_{12}$ ($x = 0$, 0.2, 0.4, 0.5, 0.6, and 0.7).

3.2.1 Experimental Details

The synthesis of the polycrystalline samples of $Tl_xFe_{1.5}Co_{2.5}Sb_{12}$ was prepared from the starting materials, chunks of Tl (5N), Fe (3N), Co (3N), and Sb (3N). The precursors have carefully been weighed out with the stoichiometric ratio and loaded in the silica tubes. The silica tubes were sealed under vacuum using an oxygen/hydrogen torch and transferred in the vertical furnace. The silica tubes have been heated with the melting condition (1323 K, 2 K/min, 72 hr holding) and then rapidly quenched by putting the heat treated silica tubes into cold water. The ingots consisting of unstable phases have been annealed for 14 days at 873 K in order to obtain the thermodynamically stable phases. The as-prepared ingots have been finely reduced to powder. The as-prepared powders were sintered using hot-press apparatus at 823 K for 2 hrs by applying the pressure of 45 MPa under flowing Ar. Column and disc shaped bulk samples were prepared for the characterization of microstructure and TE properties.

The X-ray diffraction (XRD) patterns have been collected from the commercial equipment (Ultima IV, Rigaku) with Cu Ka radiation at room temperature. The lattice parameters for all samples were estimated from the least-squares fitting to 2θs, using the standard Si, the external reference material, by utilizing PDXL, Rigaku's diffraction software. The occupancies of elements in matrix phases have been obtained with Rietveld refinement by using Rietan-FP program.[54] The fine-structure and quantitative element analysis for samples has been obtained at room temperature from the Field Emission Scanning Electron Microscopy (FE-SEM; JEOL, JSM-6500F) with the Energy Dispersive X-ray (EDX) spectroscopy under the vacuum. The Seebeck coefficient S and the electrical resistivity ρ have been obtained by measuring the samples with the cylindrical shape in commercial equipment (ZEM-1, ULVAC) in He gas atmosphere. The thermal diffusivity α obtained on the laser flash method by measuring the samples with the disc shape in commercial equipment (ULVAC, TC-7000) under vacuum. The thermal conductivity $\kappa = \alpha C_p d$ have calculated from the conventional relation $\kappa = \alpha C_p d$, where C_p is the heat capacity from the Durong-Petit model, $C_p = 3nR$, and the d is the density. The densities for the samples have been obtained through the manually taken dimensions and weights.
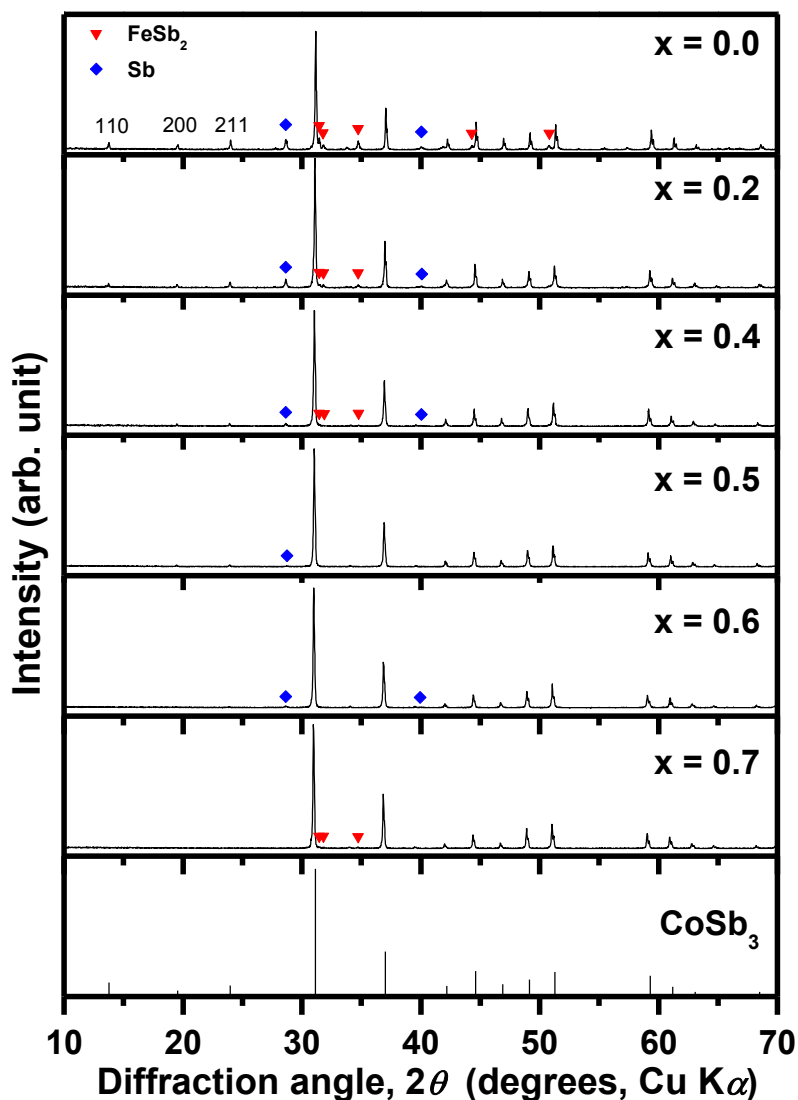
3.2.2 Results and Discussion

Figure 3.11 Powder XRD patterns of polycrystalline samples with nominal composition $Tl_xFe_{1.5}Co_{2.5}Sb_{12}$ ($x = 0$, 0.2, 0.4, 0.5, 0.6, and 0.7).

The powder XRD patterns of the polycrystalline samples of $Tl_xFe_{1.5}Co_{2.5}Sb_{12}$ ($x = 0$, 0.2, 0.4, 0.5, 0.6, and 0.7) are shown in Figure 3.11. Most of all the peaks in the XRD patterns were identified as peaks derived from the skutterudite phase as a major phase. However, the XRD patterns for the samples with $x = 0$, 0.2, and 0.4 shows the peaks of $FeSb_2$ and Sb as secondary phases, where their peak intensities increase with decreasing x. The samples with $x = 0.5$ and 0.6 have Sb and the sample with $x = 0.7$ includes $FeSb_2$ as a secondary phase. Particularly, the samples with $x = 0.5$ and 0.6 were most close to the single skutterudite phase.

Kitagawa et al. reported the composition and crystal structure dependences of the skutterudite phases, where a single skutterudite phase exists within the specific composition area.[17] In the rest area, a single skutterudite phase and secondary phases such as $FeSb_2$ and Sb coexist. It is consistent with the result of the samples of $Tl_xFe_{1.5}Co_{2.5}Sb_{12}$.

The intensity ratio of (211) and (310) peaks for the skutterudite phase increased as Tl content decreased, which is an evidence of Tl-filling.[17] It's well known that these peaks gradually become smaller as the voids of the skutterudites are filled by the filling atoms. Based on the filling behaviour in skutterudite structures, for all samples, as shown in Table 3.6, one can know that the Tl filling fraction increased with increasing the nominal Tl content x. In Table 3.6, the the lattice parameter continuously increased with increasing x, which means that the Tl filling fraction limit might be over $x = 0.7$. All samples had the high density and the relative density of the samples with $x = 0.5$ and 0.6 which was nearly close to the skutterudite single phase indicated above 97% T.D.

Table 3.6. Lattice parameter a, XRD peak ratio I_{211}/I_{013}, and density d, for polycrystalline samples of $Tl_xFe_{1.5}Co_{2.5}Sb_{12}$ ($x = 0$, 0.2, 0.4, 0.5, 0.6, and 0.7).

Nominal x	a (nm)	I_{211}/I_{013}	d	
			(g cm^{-3})	(% T.D.)
0	0.90630(2)	0.077	7.56	-
0.2	0.90783(2)	0.039	7.68	-
0.4	0.90942(2)	0.020	7.80	-
0.5	0.91034(5)	0.015	7.82	99
0.6	0.91071(5)	0.012	7.76	97
0.7	0.91090(4)	~ 0	7.95	-
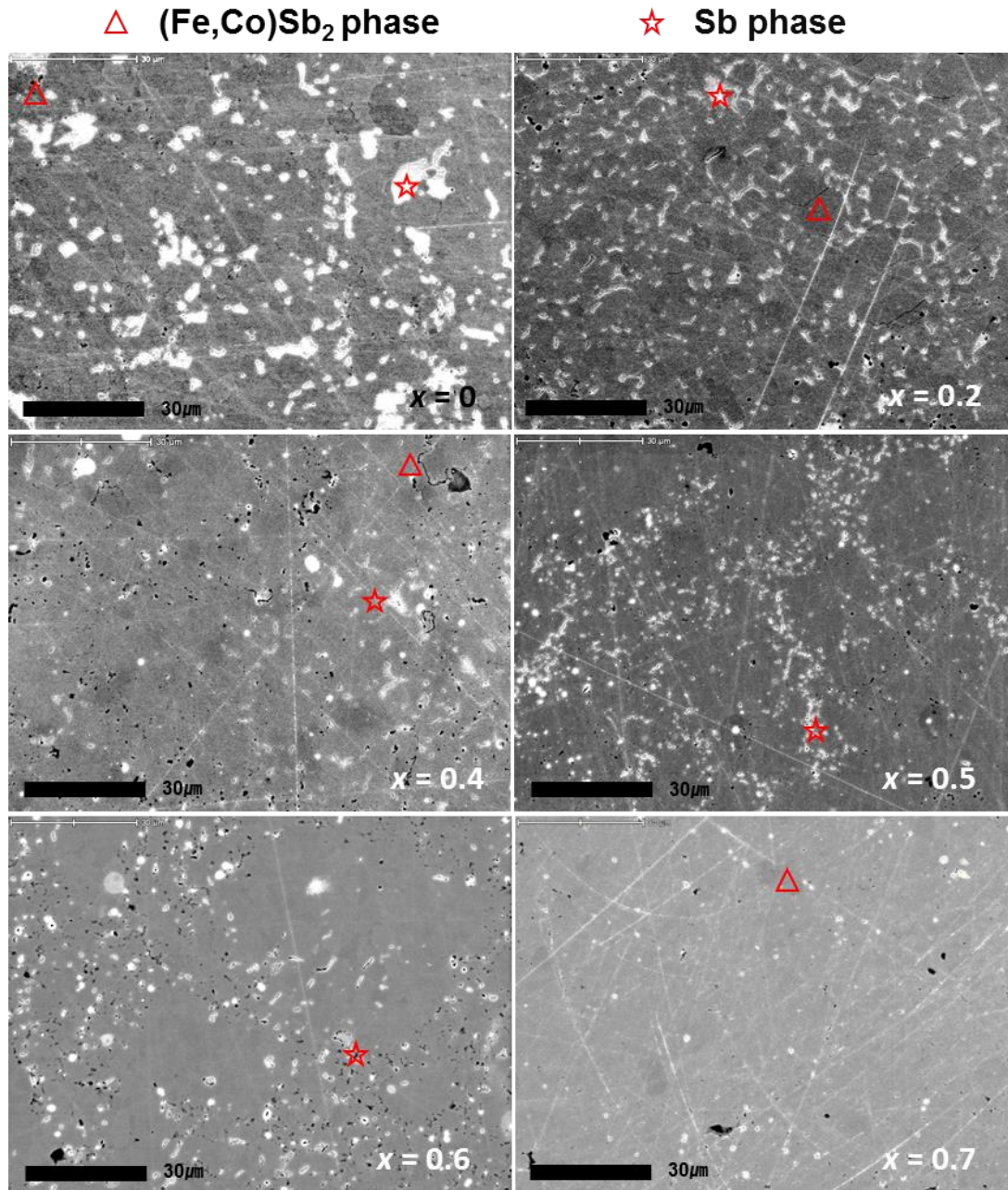
Figure 3.12 FE-SEM images of polycrystalline samples with nominal composition $Tl_xFe_{1.5}Co_{2.5}Sb_{12}$ ($x = 0$, 0.2, 0.4, 0.5, 0.6, and 0.7).

Figure 3.12 shows the secondary electron images obtained from FE-SEM for the polycrystalline samples with nominal composition $Tl_xFe_{1.5}Co_{2.5}Sb_{12}$ ($x = 0$, 0.2, 0.4, 0.5, 0.6 and 0.7). One can see that the content of secondary phases qualitatively has been changed as the Tl content. From the FE-SEM/EDX analysis, it was confirmed that the samples with $x \leq$

0.4 show two secondary phases which are the $(Fe,Co)Sb_2$ phase, and the Sb phase. On the other hand, the samples with $x = 0.5$ and 0.6 included the Sb phase and the sample with $x = 0.7$ included the $(Fe,Co)Sb_2$ phase as the secondary phase. Furthermore, the black spots below 5 μm indicates the Tl-Fe rich system, which is that the atoms not being incorporated into the structure must be pushed out in front of the growth front. The results are well consistent with the XRD result.

Table 3.7 Chemical compositions at the skutterudite matrix-phase regions of polycrystalline samples with nominal composition $Tl_xFe_{1.5}Co_{2.5}Sb_{12}$ ($x = 0$, 0.2, 0.4, 0.5, 0.6 and 0.7), determined by quantitative EDX analysis. All compositions show the average values obtained by repeating the point analysis at least 10 times.

Nominal composition	Fe/Co ratio	Chemical composition (at.%)				Measured composition
		Tl	Fe	Co	Sb	
$Fe_{1.5}Co_{2.5}Sb_{12}$	0.37	-	6.5	17.7	75.7	$Fe_{1.03}Co_{2.81}Sb_{12}$
$Tl_{0.2}Fe_{1.5}Co_{2.5}Sb_{12}$	0.52	1.1	7.8	15.1	76.0	$Tl_{0.17}Fe_{1.03}Co_{2.81}Sb_{12}$
$Tl_{0.4}Fe_{1.5}Co_{2.5}Sb_{12}$	0.52	2.4	8.1	15.7	73.8	$Tl_{0.39}Fe_{1.32}Co_{2.38}Sb_{12}$
$Tl_{0.5}Fe_{1.5}Co_{2.5}Sb_{12}$	0.59	2.8	8.8	15.0	73.3	$Tl_{0.46}Fe_{1.44}Co_{2.46}Sb_{12}$
$Tl_{0.6}Fe_{1.5}Co_{2.5}Sb_{12}$	0.58	3.3	8.7	15.0	73.0	$Tl_{0.54}Fe_{1.43}Co_{2.47}Sb_{12}$
$Tl_{0.7}Fe_{1.5}Co_{2.5}Sb_{12}$	0.52	3.9	8.1	15.4	72.6	$Tl_{0.64}Fe_{1.34}Co_{2.55}Sb_{12}$

Additionally, as shown in Table 3.7, the chemical compositions of the matrix phases were quantitatively determined by the EDX analysis. Although the Fe/Co ratio in the skutterudite phases was fixed (Fe/Co = 0.6) for the nominal composition of all samples, it was modified as increasing Tl content. In particular, up to $x = 0.5$, the increase of the nominal Tl content leaded to the increase of the Fe/Ni ratio as well as the increase of Tl filling fraction in the skutterudite phases, which means that the relative content of the stable skutterudite phases increased with increasing Tl by the excessive charge compensation of Tl. However, as increasing Tl more, the Fe/Ni ratio decreased, while the Tl increased as ever. Additionally, the

decrease of Fe/Co ratio in the sample with $x = 0.7$ leaded to the formation of the $(Fe,Co)Sb_2$ phase. This is the similar trend with $Tl_xFe_{2.5}Ni_{1.5}Sb_{12}$ system of Chapter 3.1. Thus, to precisely investigate the chemical compositions and the crystallography, we have performed the Rietveld refinement for the XRD patterns.

Table 3.8 Rietveld refinement results for polycrystalline samples with nominal composition $Tl_xFe_{1.5}Co_{2.5}Sb_{12}$ ($x = 0.4$, 0.5, 0.6, and 0.7). [Atomic positions: Tl, 2a (0, 0, 0); Fe/Co, 8c (1/4, 1/4, 1/4); Sb, 24g (0, y, z). Fe/Co ratios are obtained from Table 2.]

Nominal composition	$Tl_{0.4}Fe_{1.5}Co_{2.5}Sb_{12}$	$Tl_{0.5}Fe_{1.5}Co_{2.5}Sb_{12}$	$Tl_{0.6}Fe_{1.5}Co_{2.5}Sb_{12}$	$Tl_{0.7}Fe_{1.5}Co_{2.5}Sb_{12}$
Composition obtained from Rietveld	$Tl_{0.41}Fe_{1.36}Co_{2.64}Sb_{12}$	$Tl_{0.51}Fe_{1.48}Co_{2.52}Sb_{12}$	$Tl_{0.59}Fe_{1.47}Co_{2.53}Sb_{12}$	$Tl_{0.66}Fe_{1.38}Co_{2.62}Sb_{12}$
Space group	$Im\bar{3}$ (#204)			
Radiation	Cu Kα (1.54056 Å)			
2θ range (deg.)	10 ~ 100			
Step width (deg.)	0.02			
Counting time (s/step)	3			
U_{iso} (Å^2) for Tl	0.0160	0.0160	0.0160	0.0160
U_{iso} (Å^2) for Fe/Ni	0.0043	0.0018	0.0020	0.0045
U_{iso} (Å^2) for Sb	0.0060	0.0060	0.0060	0.0060
y (Sb)	0.8416	0.8415	0.8412	0.8418
z (Sb)	0.6636	0.6640	0.6636	0.6634
Reliablility factors				
R_B	2.99	2.78	2.59	3.11
R_F	3.58	3.88	2.86	4.97
S	1.16	1.10	1.12	1.13
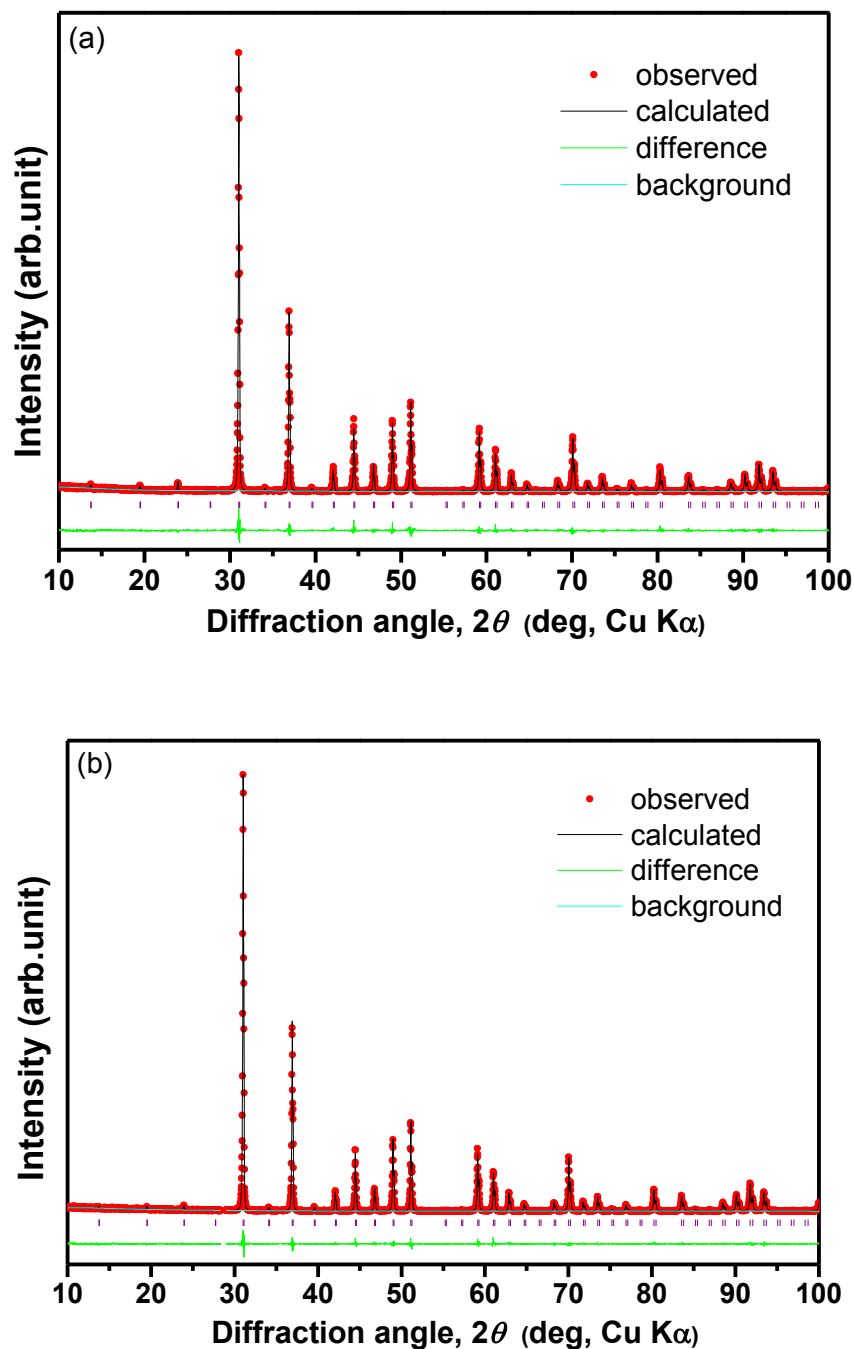
Figure 3.13 Powder XRD patterns of polycrystalline samples with nominal composition (a) $Tl_{0.4}Fe_{1.5}Co_{2.5}Sb_{12}$ and (b) $Tl_{0.5}Fe_{1.5}Co_{2.5}Sb_{12}$ showing observed, calculated, background, and difference curves at room temperature. The expected peak positions are marked with vertical ticks.
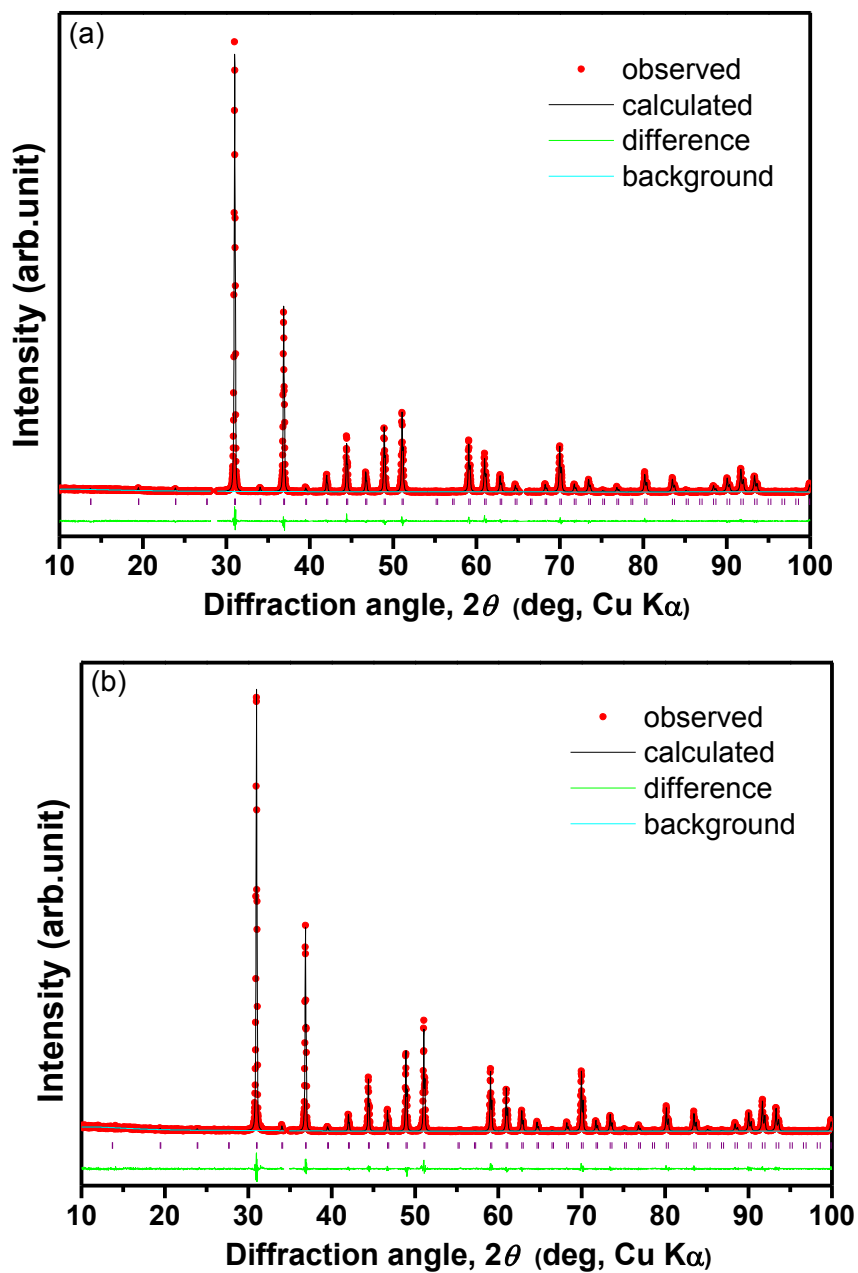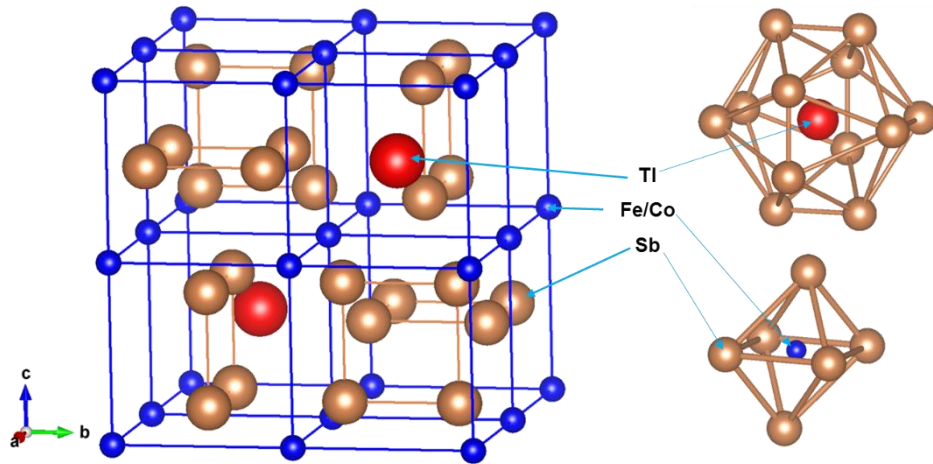
Figure 3.14 Powder XRD patterns of polycrystalline samples with nominal composition (a) $Tl_{0.6}Fe_{1.5}Co_{2.5}Sb_{12}$ and (b) $Tl_{0.7}Fe_{1.5}Co_{2.5}Sb_{12}$ showing observed, calculated, background, and difference curves at room temperature. The expected peak positions are marked with vertical ticks.

Figure 3.15 Crystal structure of $Tl_xFe_{1.5}Co_{2.5}Sb_{12}$.(left) Tl atoms on the 2a site and Fe/Co atoms on the 8c site are surrounded by 12 Sb atoms and 6 Sb atoms, respectively.(right)

In the same way with the analysis for $Tl_xFe_{2.5}Ni_{1.5}Sb_{12}$ system, Rietveld refinements have been performed as following two assumptions. Firstly, the U_{iso} values, the atomic displacement parameter, of Tl and Sb were fixed as that for Tl in $Tl_{0.75}Co_3FeSb_{12}$ reported by B.C. Chakoumakos et al..[15] Secondly, the Fe/Co ratio was taken from the quantitative EDX result for the skutterudite matrix phases in Table 3.7. As shown in Figures 3.13 and 3.14, the calculated values is well consistent with the observed ones. Figure 3.15 shows the crystal structure of the calculated filled-skutterudites.

Table 3.8 shows the result of the Rietveld refinement for the skutterudite matrix phases with nominal composition $Tl_xFe_{1.5}Co_{2.5}Sb_{12}$ ($x = 0$, 0.2, 0.4, 0.5, 0.6, and 0.7). The result indicates that the Tl-filling fractions were similar with that of the measured compositions in Table 3.6 and increased with increasing Tl content. In particular, in the case of the sample with $x = 0.4$ and 0.5, the Tl filling fractions obtained from Rietveld refinement were overestimated compared to the Tl content in the nominal composition, which means that the formation of secondary phases leaded to the reduction of the skutterudite phase and thus most of the Tl atoms were nearly filled into the voids of the skutterudite matrix phases. On the other hand, it is considered that the increase of Tl filling fraction dominantly affected the increase of lattice parameter.
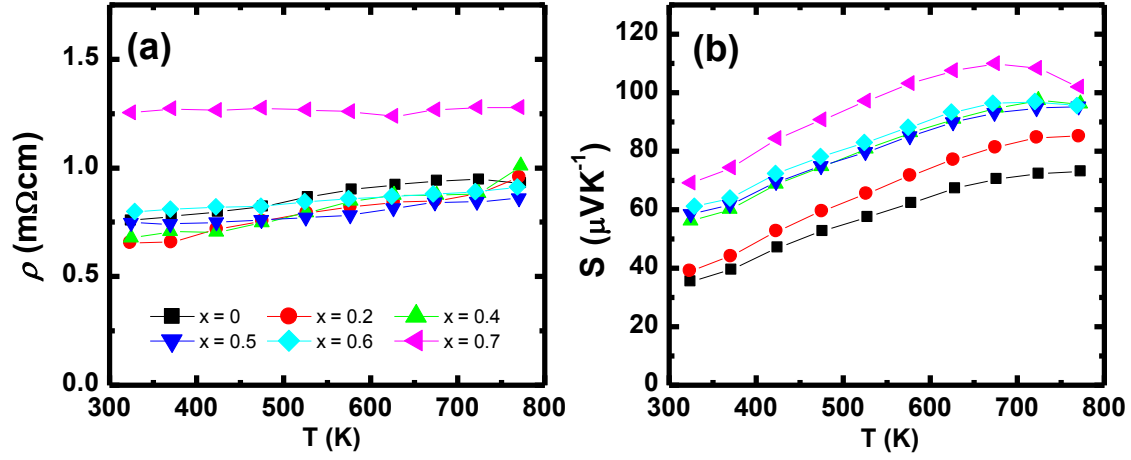
Figure 3.16 (a) The electrical resistivity ρ and (b) Seebeck coefficient S as a function of temperature for polycrystalline samples with nominal composition $Tl_xFe_{1.5}Co_{2.5}Sb_{12}$ ($x = 0$, 0.2, 0.4, 0.5, 0.6, and 0.7).
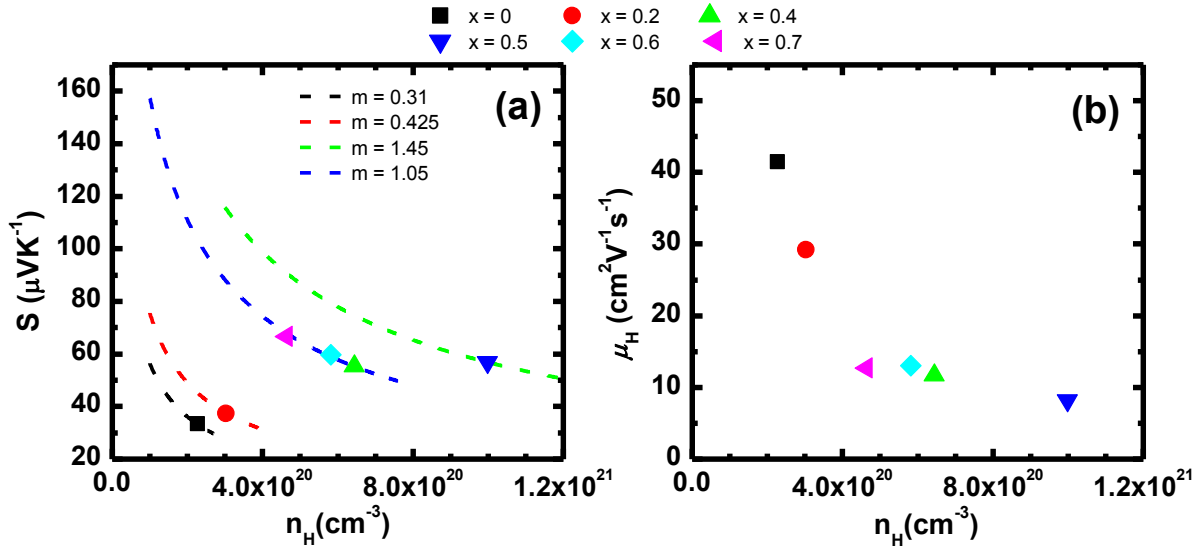

Figure 3.17 Carrier concentration dependences of (a) Seebeck coefficient S and (b) Hall mobility μ_H for polycrystalline samples with nominal composition $Tl_xFe_{1.5}Co_{2.5}Sb_{12}$ ($x = 0$, 0.2, 0.4, 0.5, 0.6, and 0.7).

Table 3.9 Hall coefficient R_H (300 K), electrical resistivity ρ (300 K), and thermal band gap E_g, reduced effective mass m for polycrystalline samples with nominal composition $Tl_xFe_{1.5}Co_{2.5}Sb_{12}$ (x = 0, 0.2, 0.4, 0.5, 0.6 and 0.7). [r is a carrier scattering factor.]

x	R_H $(10^{-8}m^3C^{-1})$	ρ $(10^{-2}m\Omega m)$	E_g (eV)	m (= m^*/m_0)		
				$r = 0$	$r = 1$	$r = 2$
0	2.74	0.66	-	0.62	0.31	0.21
0.2	2.06	0.70	-	0.84	0.42	0.28
0.4	0.97	0.83	0.14	2.06	1.03	0.69
0.5	0.63	0.76	-	2.83	1.42	0.94
0.6	1.07	0.83	0.14	2.07	1.03	0.69
0.7	1.34	1.06	0.15	2.00	0.99	0.66

The temperature dependence of the ρ and S for the samples with nominal composition $Tl_xFe_{1.5}Co_{2.5}Sb_{12}$ (x = 0, 0.2, 0.4, 0.5, 0.6, and 0.7) is shown in Figure 3.16. As shown in Figure 3.16 (a), the ρ values of the samples with $x \leq 0.6$ was nearly same within the error range and linearly increased with increasing temperature, which means the metallic behavior. However, the ρ of the sample with x = 0.7 was considerably high and nearly independent on the temperature. As shown in Figure 3.16 (b), the S increased with increasing Tl content and the samples with x = 0.4, 0.5, and 0.6 have the similar S values each other over the entire temperature range. The S values increase with temperature, reach a maximum near 700 K, and then decrease with the onset of thermally activated intrinsic bipolar diffusion. The bipolar diffusion, the electron-hole dual contribution, affects the samples with low carrier concentration more severely. We could confirm that the samples with x = 0.4, 0.6, and 0.7 just showed the specific maximum S value as the onset of an intrinsic bipolar diffusion in the measured temperature range. The onset of bipolar diffusion moved to low temperature with increasing Tl content, which increases the effect of electron as a minority carrier. From the onset values, one can estimate the thermal band gap (E_g) from the equation (3.1) in Chapter 3.1. Thus, as shown in Table 3.8, we estimated the E_g values for the samples with x = 0.4, 0.6, and 0.7 which indicated the narrow E_g values of ~ 0.15 eV. The E_g values of $Tl_xFe_{1.5}Co_{2.5}Sb_{12}$ are lower than E_g ~ 0.2 eV of $Tl_xFeCo_3Sb_{12}$.[42,74]
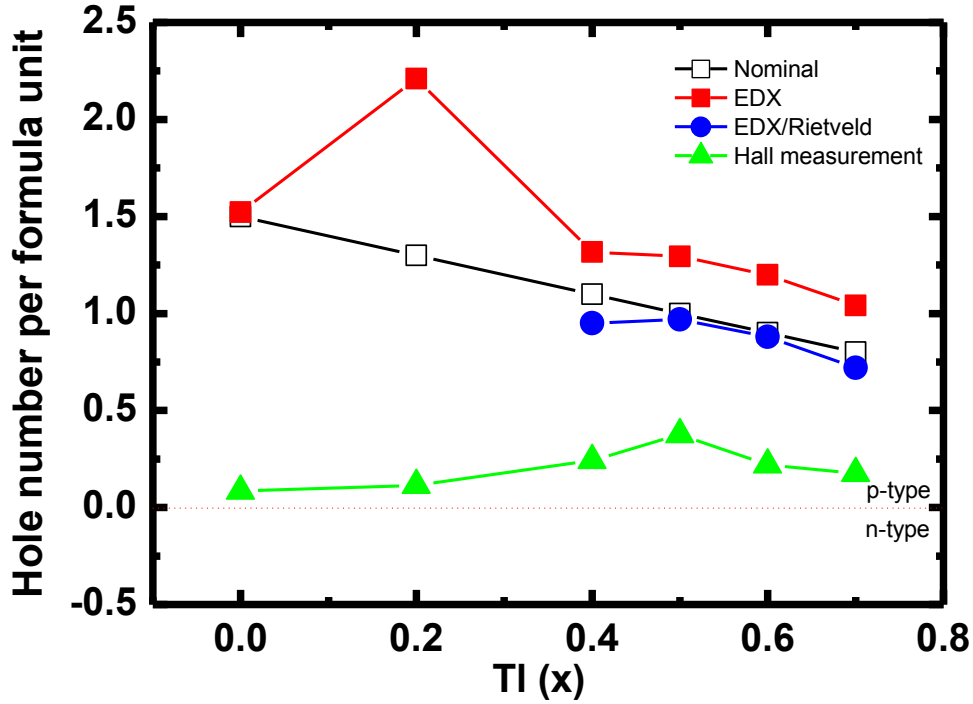
Figure 3.18 Tl content dependences of hole number per formula unit counted from compositions designed (as starting materials, empty rectangle), observed from EDX analysis (for matrix phases, red rectangle), calculated from EDX/Rietveld analyses (for matrix phases, blue circle), and measured from Hall measurement (green triangle) for polycrystalline samples with nominal composition $Tl_xFe_{1.5}Co_{2.5}Sb_{12}$ (x = 0, 0.2, 0.4, 0.5, 0.6, and 0.7).

Figure 3.17 shows the carrier concentration dependence of S and μ_H for for the samples with nominal composition $Tl_xFe_{1.5}Co_{2.5}Sb_{12}$ (x = 0, 0.2, 0.4, 0.5, 0.6, and 0.7). The S values at 300 K are also shown, which were obtained by extrapolating the S vs T curves in Figure 3.16 (b). The S and n_H increased with increasing x up to x = 0.5 and then, in the case of $x > 0.5$, the n_H considerably decreased with slight enhancement of S. The μ_H decreased with increasing n_H. As shown in Figure 3.18, the hole number obtained from the Hall measurement is even smaller than that of actual compositions obtained from EDX/Rietveld. In that regard, J. Yang et al. observed that Fe doping for $CoSb_3$ causes only a small rate of change in carrier concentration.[75] On the other hand, in the electronic structure of the $CoSb_3$-based p-type skutterudites, it have been reported that the Co substitution by Fe leads to the introduction of Fe 3d band in the vicinity of valence band edge and the Fe 3d band, a heavy band, give rise to the increase of the hole effective masses.[58,69] Thus, we need to estimate the carrier effective

mass. Thus, we estimated the reduced density of state (DOS) effective mass $m = m^*/m_0$ of the carriers using the experimental result of the S and n_H from a single parabolic band model based on Fermi statistics, where m_0 is the free electron mass. The S, hole concentration p, and Fermi integral $F_i(\eta)$ can be expressed as:[21,26,27]

$$S = \frac{k_B}{e}\left(\frac{(2+r)F_{1+r}(\eta)}{(1+r)F_r(\eta)} - \eta\right) \tag{3.3}$$

$$p = \sqrt{\frac{2}{\pi}}\left(\frac{m^* k_B T}{\hbar^2}\right)^{3/2} F_{1/2}(\eta) \tag{3.4}$$

$$F_i(\eta) = \int_0^\infty \frac{x^i dx}{1+\exp(x-\eta)} \tag{3.5}$$

where k_B is Boltzmann constant, r is the scattering factor, $\eta = E_F/k_B T$ is the reduced chemical potential, and $\hbar$ is reduced Planck constant. Based on the carrier scattering mechanism, it is assumed that the r value as $r = 0$ for both acoustic phonon scattering and alloy disorder scattering, $r = 2$ for scattering by ionized impurities. Here, the intermediate value of $r = 1$ for those mixed mechanism was mainly used and all m values for the three mechanisms is shown in Table 3.9. The m values of all samples were even larger than $m = 0.175$ of an undoped-$CoSb_3$.[26] As a matter of fact, the estimation for the samples with $x = 0$ and 0.2 is not desirable because they noticeably have large amount of secondary phases. However, it might be meaningful because it enable to understand the side effects of secondary phases for the carrier transport behavior.

Figure 3.19 shows the Fe content dependence Temperature dependences of the m and the PF for all samples. Figure 3.19 (a) specifically shows that the m is dependent on the Fe content, which results from the increment of the influence by the heavy Fe $3d$ band in the vicinity of the valence band edge. From the proportional relation between the weighted mobility $\mu_H(m^*)^{3/2}$ and the PF in the single parabolic band model, one can know that the increase of the Fe/Co ratio leads to the enhancement of the PF. It is comparable to the PF of the $Tl_{0.2}FeCo_3Sb_{12}$ sample of Kim et al..[42]

Figure 3.20 (a) and (b) shows the thermal conductivity κ and the lattice thermal conductivity κ_{lat} as a function of temperature, respectively. The κ_{lat} was calculated by using the

Wiedemann-Franz law, i.e. $\kappa_{lat} = \kappa - LT\rho^{-1}$, where L is the Lorentz number (2.45×10^{-8} W Ω K^{-2}). The κ decreases with increasing Tl content up to $x = 0.4$, then increases for $x = 0.5$, and then decreases up to $x = 0.7$. The κ_{lat} shows the different trend with the κ, where the κ decreases with increasing Tl content up to $x = 0.4$, then increases up to $x = 0.7$. The trend of κ_{lat} is consistent with that of the Fe/Co ratio, which means that the alloy scattering considerably has an influence on the scattering of heat carrying phonon as well as the rattling effect of Tl filled into the voids of skutterudite phases. [16,58,61]
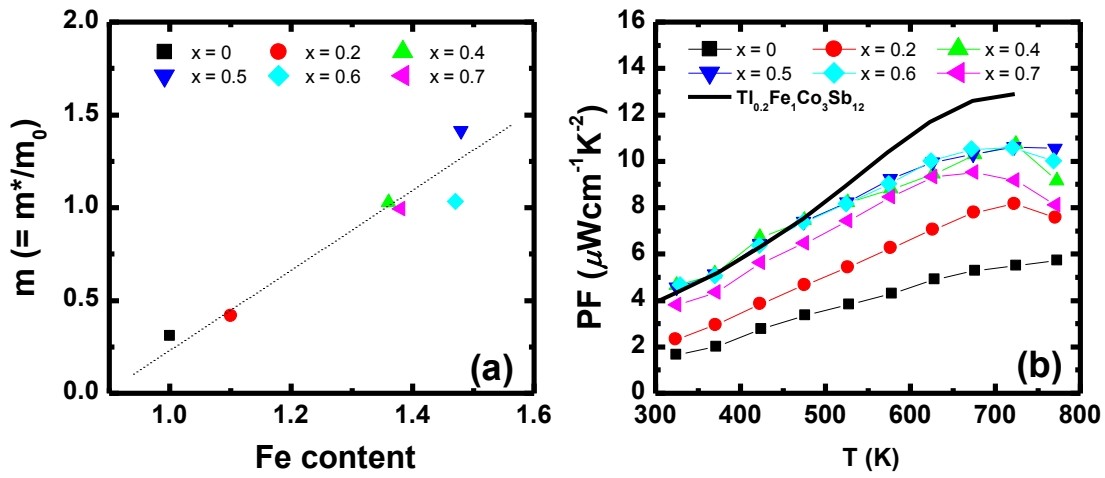
Figure 3.19 Fe content dependence Temperature dependences of (a) the reduced DOS effective mass m and (b) Power Factor PF for polycrystalline samples with nominal composition Tl$_x$Fe$_{1.5}$Co$_{2.5}$Sb$_{12}$ ($x = 0$, 0.2, 0.4, 0.5, 0.6, and 0.7). The dot line is the guide line.
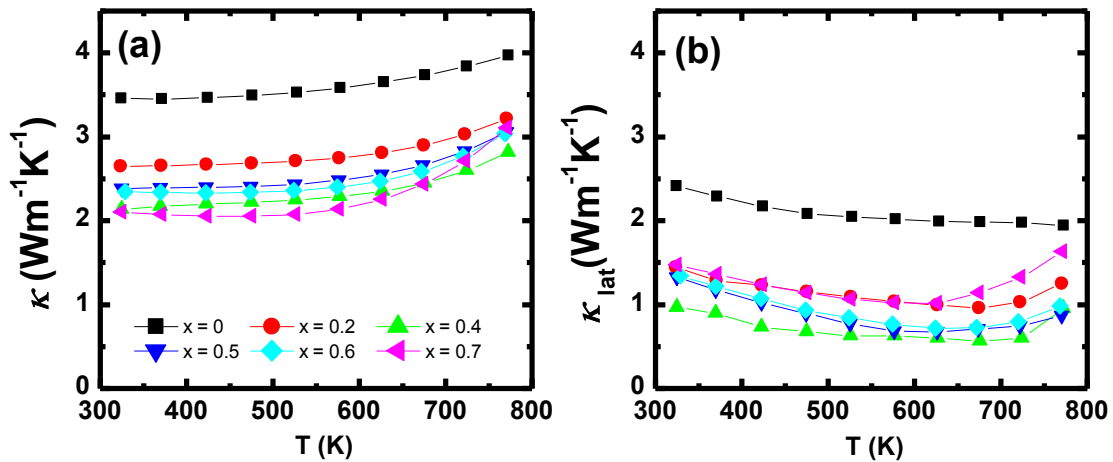
Figure 3.20 (a) The thermal conductivity κ, (b) lattice thermal conductivity κ_{lat} as a function of temperature for polycrystalline samples with nominal composition Tl$_x$Fe$_{1.5}$Co$_{2.5}$Sb$_{12}$ ($x = 0$, 0.2, 0.4, 0.5, 0.6, and 0.7).
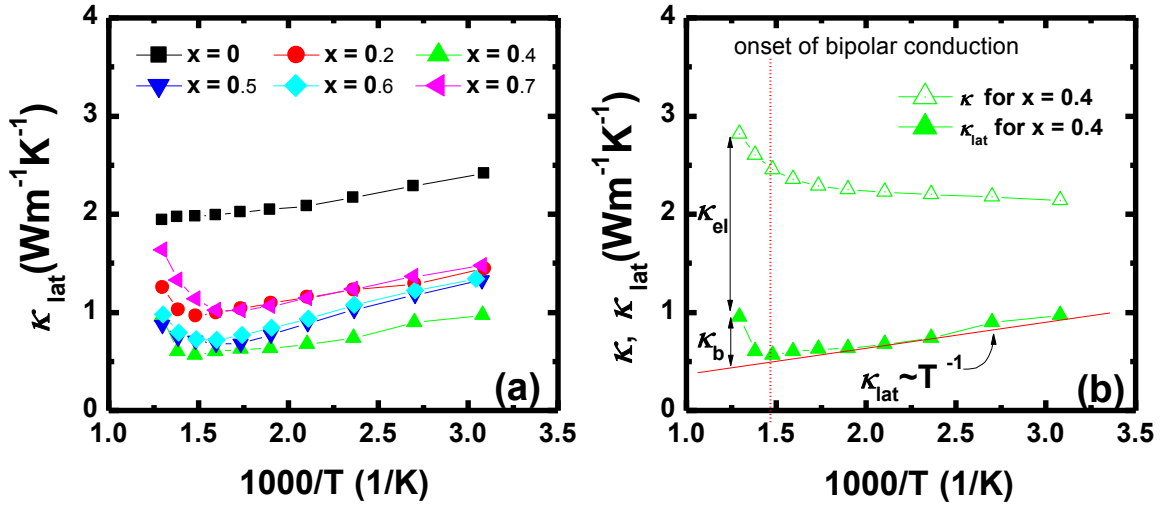
Figure 3.21 (a) κ_{lat} and (b) κ, κ_{lat} as a function of temperature for polycrystalline samples with nominal composition $Tl_xFe_{1.5}Co_{2.5}Sb_{12}$ ($x = 0$, 0.2, 0.4, 0.5, 0.6, and 0.7).
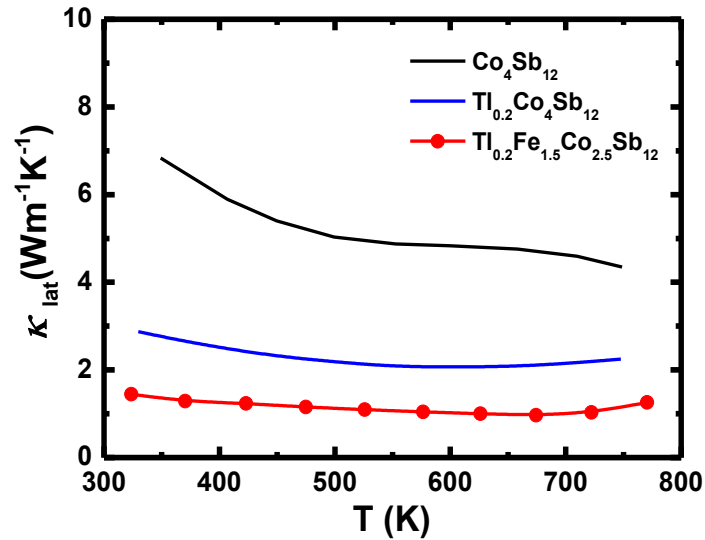
Figure. 3.22 Lattice thermal conductivity of Co_4Sb_{12}, $Tl_{0.2}Co_4Sb_{12}$, and $Tl_{0.2}Fe_{1.5}Co_{2.5}Sb_{12}$.[39]

Figure 3.21 (a) and (b) shows the inverse temperature dependence of κ_{lat} and κ, κ_{lat}, respectively. It shows that all samples have the considerable contribution of the bipolar diffusion by the intrinsic excitation. The bipolar diffusion contribution in thermal conductivity can be expressed as the equation (3.2).[24] Therefore, above the temperature corresponding to the onset of bipolar diffusion, total thermal conductivity is consisting of three contributions, carrier, lattice, and bipolar diffusion. As shown in Figure 3.22, it can be considered that the

remarkable reduction of κ_{lat} is mainly caused by the rattling effect of the filled Tl atoms.[39] Additionally, it is thought that the point defects from Fe doping also scattered heat carrying phonons, leading to further reduction of κ_{lat}.
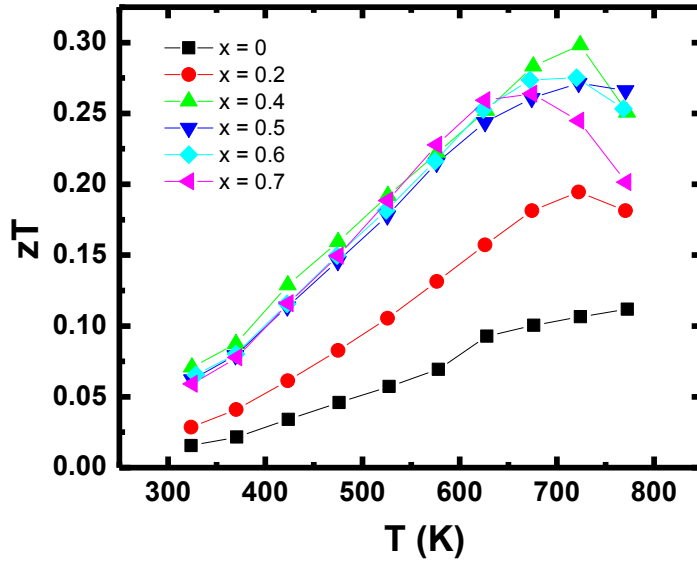
Figure 3.23 Dimensionless figure of merit zT as a function of temperature for polycrystalline samples with nominal composition $Tl_xFe_{1.5}Co_{2.5}Sb_{12}$ ($x = 0$, 0.2, 0.4, 0.5, 0.6, and 0.7).

Finally, Figure 3.23 shows the temperature dependence of dimensionless figure of merit zT. The sample with $x = 0.4$ exhibited the best zT values among all samples and the maximum zT value was ~ 0.3 at 724 K.

3.2.3 Summary

In this study, polycrystalline samples of $Tl_xFe_{1.5}Co_{2.5}Sb_{12}$ ($x = 0$, 0.2, 0.4, 0.5, 0.6, and 0.7) were prepared. Their crystallographic properties were precisely characterized from the FE-SEM/EDX and Rietveld refinements. Based on the techniques, their TE properties were studied in the temperature range from 300 K to 773 K. The Tl filling fraction increased with increasing the nominal Tl content and the maximum Tl filling fraction was 0.66 for the sample with nominal composition $Tl_{0.7}Fe_{1.5}Ni_{2.5}Sb_{12}$. All samples showed p-type conduction. The increase

of Tl filling fraction contributed to the stabilization of the crystal structure by the compensation of excessive charge, which leaded to the enhancement of the carrier transport property and the heat carrying phonon scattering. Furthermore, it was confirmed that the Fe/Co ratio have a strong influence on the heat carrying phonon scattering as well as the adjustment of hole concentration. In the present study, the optimal Tl ratio was $x = 0.4$. So the maximum zT value was around 0.3 at 724 K obtained for the sample of $Tl_{0.4}Fe_{1.5}Ni_{2.5}Sb_{12}$.

CHAPTER IV

Thermoelectric properties of Ga and In co-added *n*-type Skutterudites

For a while, it was considered that Ga and In among Group 13 elements is not suitable as a filler for the voids, since it was predicted they should have no chance to fill into the voids of skutterudites from the thermodynamic calculation based on the Gibbs free energy of the chemical reaction.[76] However, recently, Ga and In among Group 13 elements is receiving the spotlight as a filler of $CoSb_3$-based skutterudites because it is confirmed that they play a role as a filler despite of the unusual behavior and could lead to high zT.[35,38,47,77-86] Furthermore, they are the suitable elements for mass production because they are non-toxic and antioxidant. Nonetheless, we essentially need to shed light on their unusual behavior in skutterudite structures for the stable application in a TE module. In particular, among the single-filled skutterudites, In-filled $CoSb_3$-based skutterudites have been reported as a material showing high TE performances.[40,82,87] Furthermore, for double filling, Li et al. reported zT of 1.43 for $In_{0.25}Ce_{0.15}Co_4Sb_{12}$.[37] However, there is a room to improve the TE performances through the several methods such as the multiple doping with other elements, the synthesis by more rapid cooling rate, etc. On the point of view, in the present study, we have been investigated Ga and In co-doping process for $CoSb_3$-based skutterudites.

4.1 $Ga_{0.2}In_xCo_4Sb_{12}$ system[88]

The behavior of group 13 elements in $CoSb_3$-based skutterudites, has been the debate topic.[38,79,80,84,86] Specially, the occupation of Ga and In doped into $CoSb_3$ is still so vague, which is important crystallographic information to analyze the TE properties.[84] One of the biggest arguments would be the position and the occupancy of the Ga because Ga has all potentials to be a filler, Co substituted one, and Sb substituted one. Furthermore, Ga might simultaneously occupy more than two sites. In the present study, it is assumed that Ga could occupy the two sites, a filler site in void and Sb site. Additionally, high zT values ($zT > 1$) were

achieved in the In-CoSb$_3$ system when x above 0.2 in In$_x$Co$_4$Sb$_{12}$.[87] According to the report, here, the Ga content has been fixed to be $y = 0.2$ and the In content has varied from $x = 0.15$ to 0.30 in Ga$_y$In$_x$Co$_4$Sb$_{12}$, in which the Ga content exceeding the filling limit was expected to be formed as the GaSb nanoparticles.[37,87,89]

4.1.1 Experimental Details

The synthesis of the polycrystalline samples of Ga$_{0.2}$In$_x$Co$_4$Sb$_{12}$ was prepared from the starting materials, chunks of GaSb (4N), In (4N), Co (2N), and Sb (3N). The precursors have carefully been weighed out with the stoichiometric ratio and loaded in the silica tubes. The silica tubes were sealed under vacuum using an oxygen/hydrogen torch and transferred in the vertical furnace. The silica tubes have been heated with the melting condition (1323 K, 2 K/min, 72 hr holding) and then rapidly quenched by putting the heat treated silica tubes into cold water. The ingots consisting of unstable phases have been annealed for 7 days at 723 K in order to obtain the thermodynamically stable phases. The as-prepared ingots have been finely reduced to powder. The as-prepared powders were sintered using hot-press apparatus at 923 K for 2 hrs by applying the pressure of 45 MPa under flowing Ar. Column and disc shaped bulk samples were prepared for the characterization of microstructure and TE properties.

The X-ray diffraction (XRD) patterns have been collected from the commercial equipment (Ultima IV, Rigaku) with Cu Ka radiation at room temperature. The lattice parameters for all samples were estimated from the least-squares fitting to 2θs, using the standard Si, the external reference material, by utilizing PDXL, Rigaku's diffraction software. The occupancies of elements in matrix phases have been obtained with Rietveld refinement by using Rietan-FP program.[54] The fine-structure and quantitative element analysis for samples has been obtained at room temperature from the Field Emission Scanning Electron Microscopy (FE-SEM; JEOL, JSM-6500F) with the Energy Dispersive X-ray (EDX) spectroscopy under the vacuum. The Seebeck coefficient S and the electrical resistivity ρ have been obtained by measuring the samples with the cylindrical shape in commercial equipment (ZEM-1, ULVAC) in He gas atmosphere. The Hall coefficient (R_H) was measured from the van der Pauw method under an applied magnetic field of 0.5 T in vacuum at room temperature. The Hall carrier

67

concentration (n_H) and Hall mobility (μ_H) were obtained from the R_H based on the assumptions of a single parabolic band model and a Hall factor of 1, i.e., $\mu_H = R_H/\rho$, and $n_H = 1/(eR_H)$, where e is the elementary charge. The thermal diffusivity α obtained on the laser flash method by measuring the samples with the disc shape in commercial equipment (ULVAC, TC-7000) under vacuum. The thermal conductivity $\kappa = \alpha C_p d$ have calculated from the conventional relation $\kappa = \alpha C_p d$, where C_p is the heat capacity from the Durong-Petit model, $C_p = 3nR$, and the d is the density. The densities for the samples have been obtained through the manually taken dimensions and weights.

4.1.2 Results and Discussion

The powder XRD patterns of the polycrystalline samples of $In_{0.2}Ga_xCo_4Sb_{12}$ ($x = 0.15$, 0.20, 0.25, and 0.30) are shown in Figure 3.2.1. All the peaks of the XRD patterns were identified as the skutterudite phase. However, in the XRD patterns of the samples of $x = 0.20$, 0.25, and 0.30, negligible peaks of the (Ga,In)Sb phase as the impurity phase have been observed. As shown in Table 3.2.1, the lattice parameter a of all samples increased with increasing In content x, which might indicate that the In filling fraction increased with increasing x. For all sample, high density of >98 %T.D. was obtained.

Figure 3.2.3 shows the secondary electron images obtained from FE-SEM for the polycrystal5line samples with nominal composition $In_{0.2}Ga_xCo_4Sb_{12}$ ($x = 0.15$, 0.20, 0.25, and 0.30). The size of grains were around 10 μm and the nanoparticles were observed in the grain and at the grain boundaries for all samples as shown in the enlarged images. Table 3.2.2 shows the chemical compositions for both matrix phases (X) and the grain boundaries nanoparticles (Y) gathered, which roughly notify what the nanoparticles is consisting of. From the information, one can qualitatively understand that the nanoparticles for all samples would be consisting of (Ga,In)Sb system with Ga-rich composition. In order to more accurately re-evaluate for skutterudite matrix phases, the point analysis by EDX was performed at least 10 times on several different grains and the average values are shown in Table 3.2.3. As expected, the Ga filling was nearly fixed and the In filling increased with increasing x. In order to analyse precisely more, we have performed the Rietveld refinement for the XRD patterns.
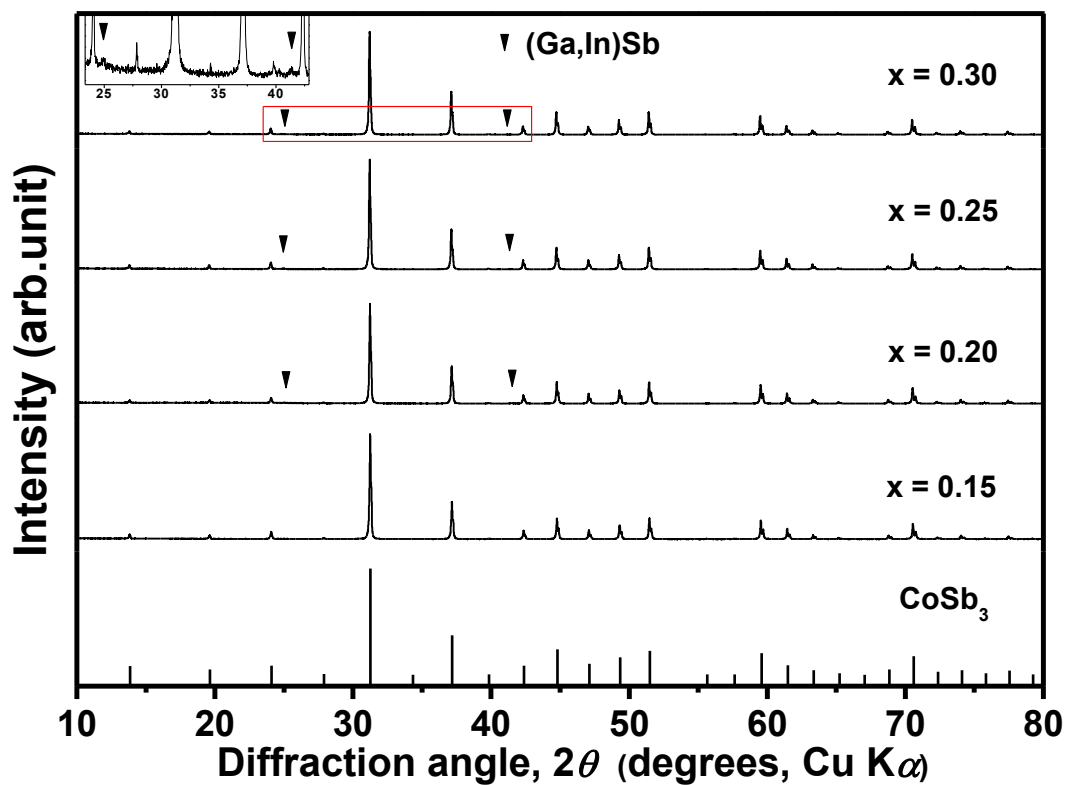
Figure 4.1. Powder XRD patterns of polycrystalline samples of $Ga_{0.2}In_xCo_4Sb_{12}$ ($x = 0.15$, 0.20, 0.25, and 0.30), together with the peak positions calculated from the crystal structure of $CoSb_3$.

Table 4.1. Lattice parameter a, sample bulk density d, relative density %T.D., Hall coefficient R_H at room temperature for polycrystalline samples of $Ga_{0.2}In_xCo_4Sb_{12}$ ($x = 0.15$, 0.20, 0.25, and 0.30).

x	a (nm)	d (gcm^{-3})	%T.D.	R_H (10^{-2}cm^{3}C^{-1})
0.15	0.9042	7.65	99	-3.96
0.20	0.9045	7.62	98	-3.33
0.25	0.9047	7.66	98	-2.75
0.30	0.9048	7.67	98	-2.36
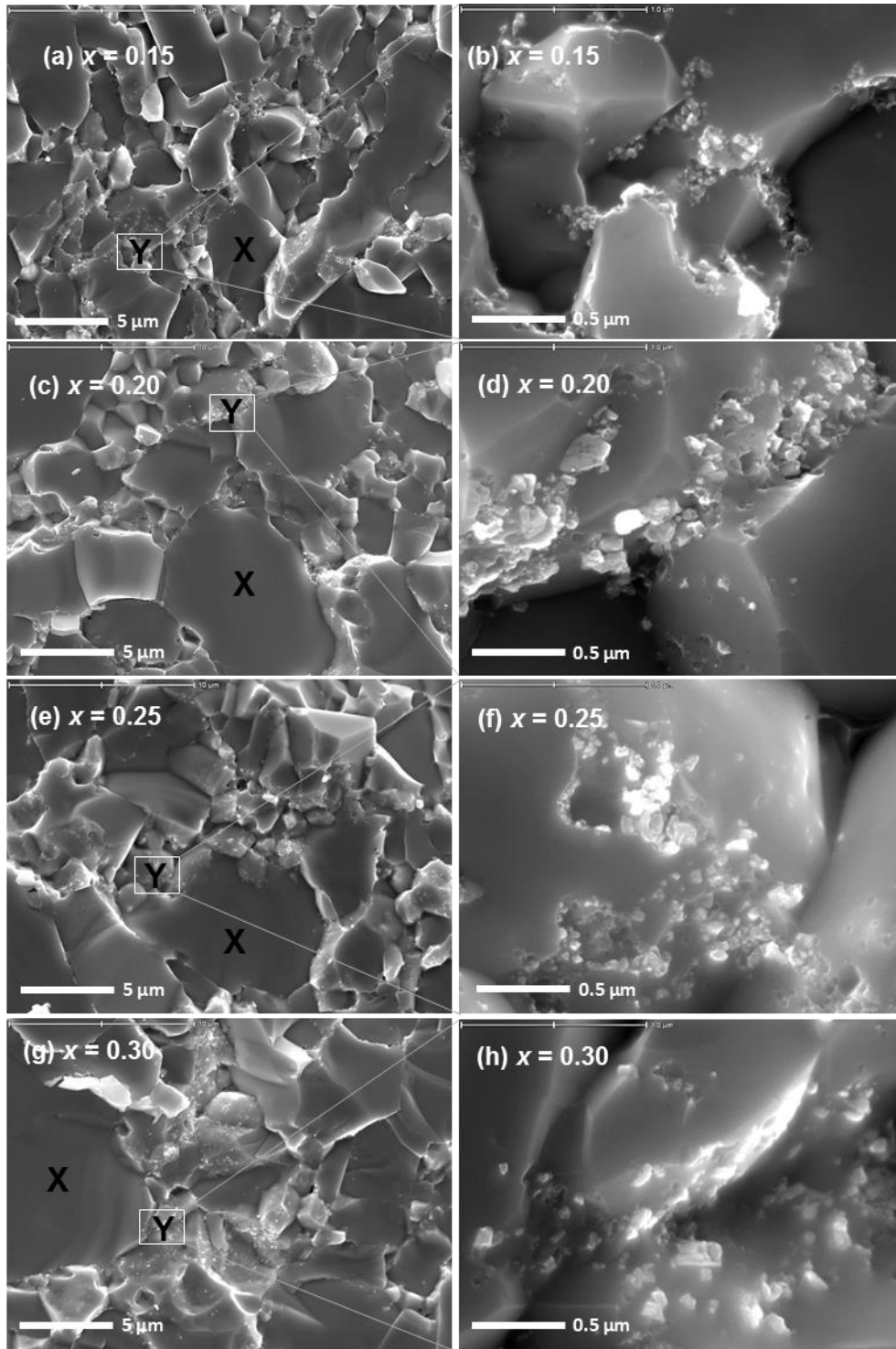
Figure 4.3 FE-SEM images of the polycrystalline $Ga_{0.2}In_xCo_4Sb_{12}$ samples; (**a**) $x = 0.15$, (**b**) $x = 0.20$, (**c**) $x = 0.25$, and (**d**) $x = 0.30$. The (**b**), (**d**), (**f**) and (**h**) are the enlarged images of white rectangle region.

Table 4.2. Chemical compositions at points 1-4 in Fig. 2, as determined by the quantitative EDX point analysis for polycrystalline samples with nominal composition $Ga_{0.2}In_xCo_4Sb_{12}$ (x = 0.15, 0.20, 0.25, and 0.30),.

Nominal composition	position	Chemical composition (at.%)			
		Ga	In	Co	Sb
$Ga_{0.2}In_{0.15}Co_4Sb_{12}$	X	0.4	1.6	24.3	73.8
	Y	6.2	1.9	22.5	69.4
$Ga_{0.2}In_{0.20}Co_4Sb_{12}$	X	0.4	1.6	23.9	74.1
	Y	7.5	3.0	21.5	68.0
$Ga_{0.2}In_{0.25}Co_4Sb_{12}$	X	0.4	1.7	24.0	74.0
	Y	9.3	4.4	19.6	66.6
$Ga_{0.2}In_{0.30}Co_4Sb_{12}$	X	0.4	1.8	23.9	74.0
	Y	9.3	2.9	21.4	66.4

Table 4.3 Chemical compositions at the skutterudite matrix-phase regions of polycrystalline samples with nominal composition $Ga_{0.2}In_xCo_4Sb_{12}$ (x = 0.15, 0.20, 0.25, and 0.30), determined by quantitative EDX analysis. All compositions show the average values obtained by repeating the point analysis at least 10 times.

Nominal composition	Ga/In ratio	Chemical composition (at.%)			
		Ga	In	Co	Sb
$Ga_{0.2}In_{0.15}Co_4Sb_{12}$	0.28	0.4	1.4	24.1	74.1
$Ga_{0.2}In_{0.20}Co_4Sb_{12}$	0.25	0.4	1.6	23.9	74.1
$Ga_{0.2}In_{0.25}Co_4Sb_{12}$	0.23	0.4	1.7	24.0	74.0
$Ga_{0.2}In_{0.30}Co_4Sb_{12}$	0.22	0.4	1.8	23.9	74.0

Table 4.4 Rietveld refinement results for polycrystalline samples of $Ga_{0.2}In_xCo_4Sb_{12}$ ($x = 0.15$, 0.20, 0.25, and 0.30). Ga/In ratio was obtained from EDX analysis and the U_{iso} ($Å^2$) values for (Ga_{VF}, In) were fixed with the value reported by A. Grytsiv et al..[Atomic positions: Ga/In, 2a (0, 0, 0); Co, 8c (1/4, 1/4, 1/4); Sb, 24g (0, y, z).]

Nominal composition	$Ga_{0.20}In_{0.15}Co_4Sb_{12}$	$Ga_{0.20}In_{0.20}Co_4Sb_{12}$	$Ga_{0.20}In_{0.25}Co_4Sb_{12}$	$Ga_{0.20}In_{0.30}Co_4Sb_{12}$
Composition obtained from Rietveld	$Ga_{0.03}In_{0.11}Co_4Sb_{11.99}$	$Ga_{0.03}In_{0.12}Co_4Sb_{11.99}$	$Ga_{0.03}In_{0.14}Co_4Sb_{11.99}$	$Ga_{0.04}In_{0.15}Co_4Sb_{11.99}$
$(Ga_{VF})/(Ga_{Sb})$	0.019/0.09	0.020/0.010	0.021/0.011	0.024/0.012
Space group	$Im\bar{3}$ (#204)			
Radiation	Cu Kα (1.54056 Å)			
2θ range (deg.)	10 ~ 100			
Step width (deg.)	0.02			
Counting time (s/step)	3			
U_{iso} ($Å^2$) for (Ga_{VF}, In)	0.0208	0.0208	0.0208	0.0208
U_{iso} ($Å^2$) for Co	0.0105	0.0061	0.0081	0.0063
U_{iso} ($Å^2$) for (Sb, Ga_{Sb})	0.0077	0.0071	0.0075	0.0072
y (Sb)	0.8424	0.8416	0.8419	0.8421
z (Sb)	0.6649	0.6644	0.6649	0.6647
Reliablility factors				
R_B	3.93	4.54	4.25	4.03
R_F	3.83	4.22	4.31	4.38
S	1.18	1.19	1.19	1.16
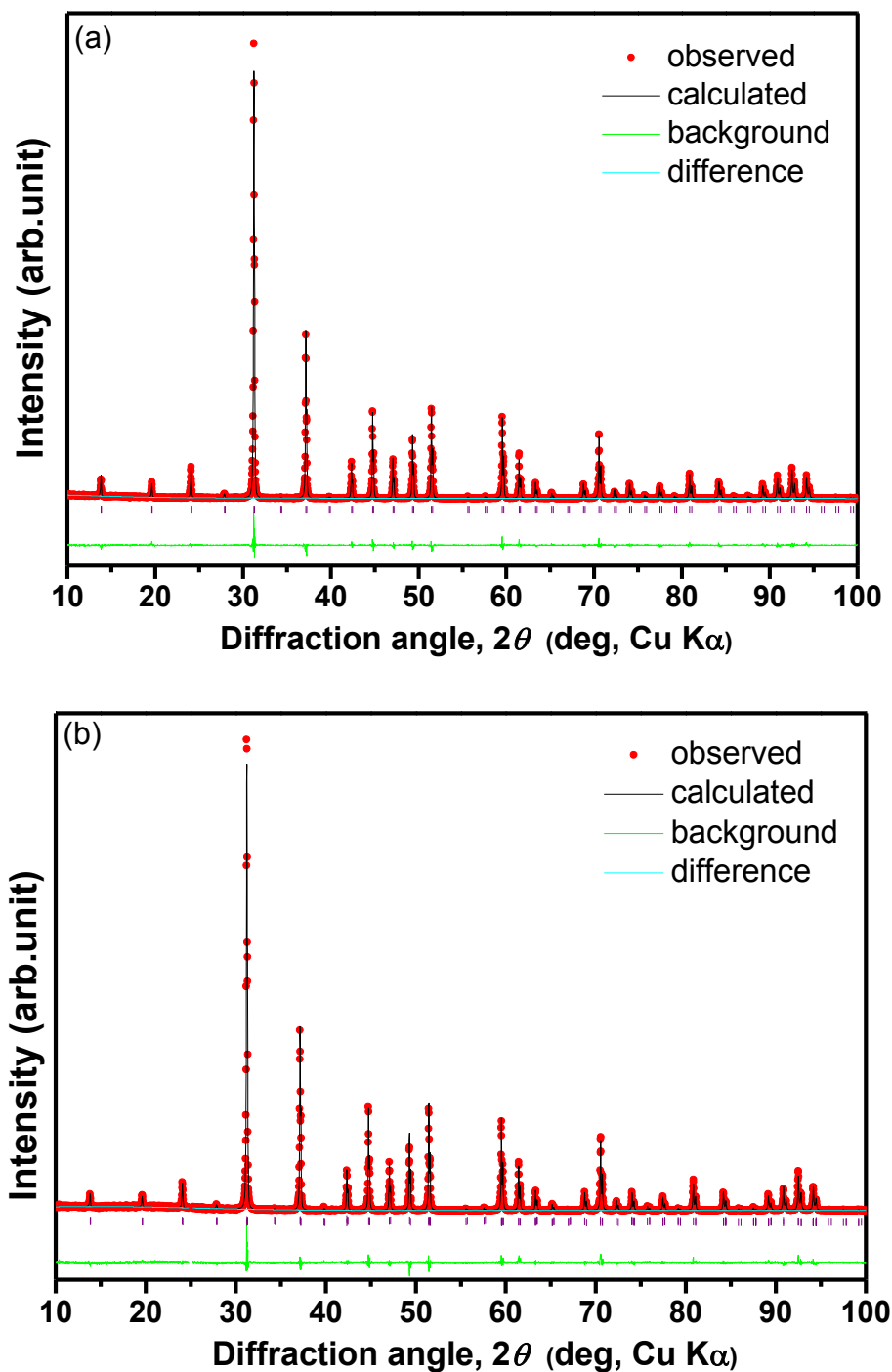
Figure 4.4 Powder XRD patterns of polycrystalline samples with nominal composition (a) $Ga_{0.2}In_{0.15}Co_4Sb_{12}$ and (b) $Ga_{0.2}In_{0.20}Co_4Sb_{12}$ showing observed, calculated, background, and difference curves at room temperature. The expected peak positions are marked with vertical ticks.
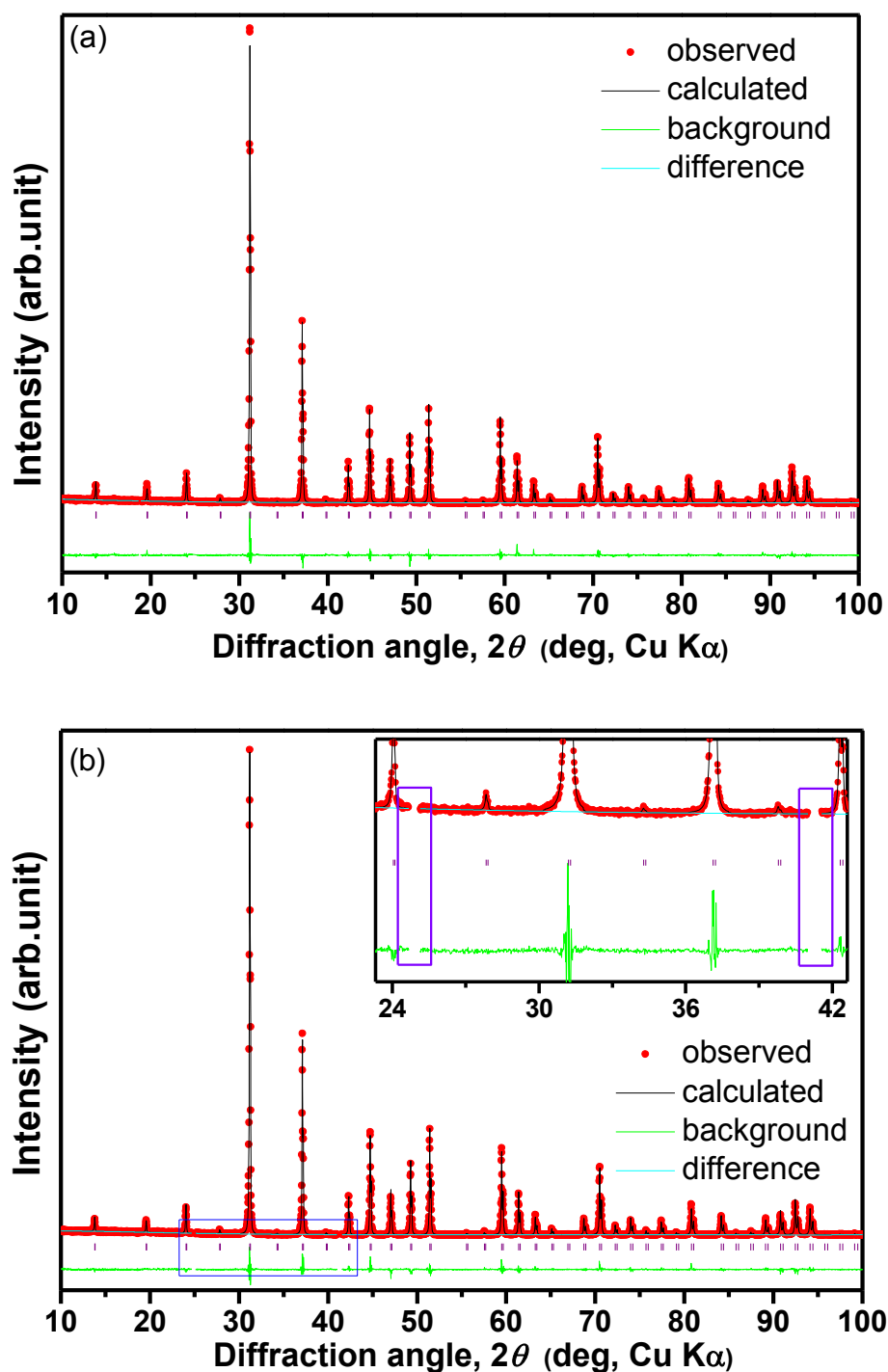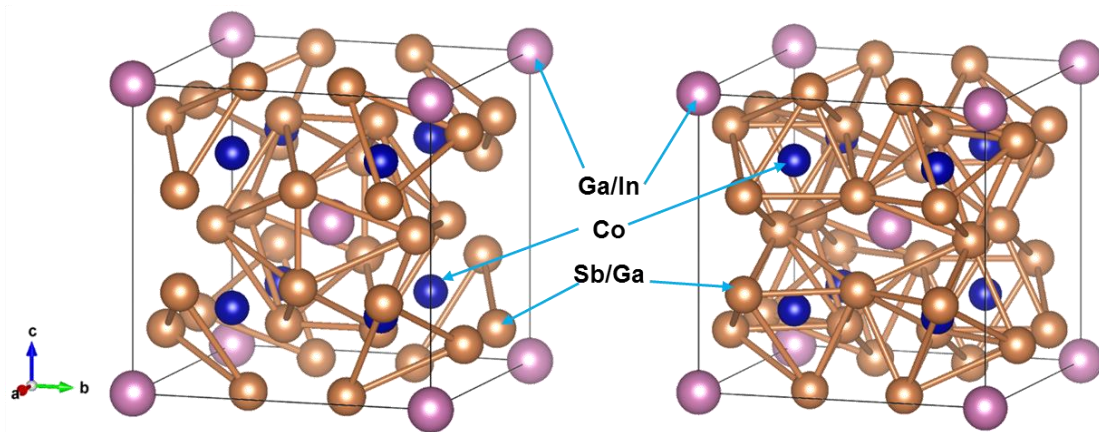
Figure 4.5 Powder XRD patterns of polycrystalline samples with nominal composition (a) $Ga_{0.2}In_{0.25}Co_4Sb_{12}$ and (b) $Ga_{0.2}In_{0.30}Co_4Sb_{12}$ showing observed, calculated, background, and difference curves at room temperature. The expected peak positions are marked with vertical ticks.

Figure 4.6 Crystal structures of $Ga_{0.2}In_xCo_4Sb_{12}$. (a) Ga/In atoms on the 2a site and (b) Co atoms on the 8c site are surrounded by 12 Sb atoms and 6 Sb atoms partially substituted by Ga, respectively.

It has been known that the doping behaviour of group 13 elements for the skutterudite phase remains unclear.[79] In particular, it has been considered that the elemental Ga and In among them may be able to occupy the void and Sb site at the same time. Recently W. Zhao et al. found that the In atoms stably fill the voids in skutterudite structure through the X-ray absorption fine structure analysis, while it has been reported that the Ga atoms are thermodynamically easy to occupy the dual site of both the void and the Sb site.[79,85] Based on the reports, we have carried out the Rietveld refinement as the following assumptions: Firstly, In can occupy only the void site, while Ga can occupy both the void and Sb sites in the ratio of 2:1.[79] Thus, the refined composition can be set as $(Ga_{VF})_yIn_xCo_4(Ga_{Sb})_{y/2}Sb_{1-y/2}$. Secondly the Ga/In ratio ($= 3y/2x$) was taken from the EDX results for the matrix phases in Table 3.2.3.[79] Thirdly, the values of U_{iso}, the thermal vibration parameter, of both Ga_{VF} and In were assumed to be the equally fixed as that for In in $In_{0.13}Co_4Sb_{12}$ reported by Grytsiv et al.[77] Fourthly, the U_{iso} values of Sb and Ga_{Sb} were postulated as same value because the Sb sites (24g) in the skutterudite structure are covalently bonded and are the stable positions compared with the void site (2a). Finally, as shown in Figure 4.5 (b), the peaks for the (Ga,In)Sb phase were excluded. Since the peaks for the (Ga,In)Sb phase did not overlap with the peaks of the skutterudite phase, the exclusion would not influence on the refinement results.

The Rietveld refinement result or polycrystalline samples of $Ga_{0.2}In_xCo_4Sb_{12}$ ($x = 0.15$, 0.20, 0.25, and 0.30) is shown in Table 3.2.4. The result shows that the Ga filling faction is nearly constant and the In filling fraction increases with increasing x, though the Ga filling

fraction of the sample with $x = 0.30$ was slightly larger than those of the others. Thus, we can say that the increment of lattice parameter is responsible to the In filling fraction. Furthermore, both Ga and In contents exceeding the filling fraction participated in the formation of nanoparticles which are expected as a scattering point for heat carrying phonon.
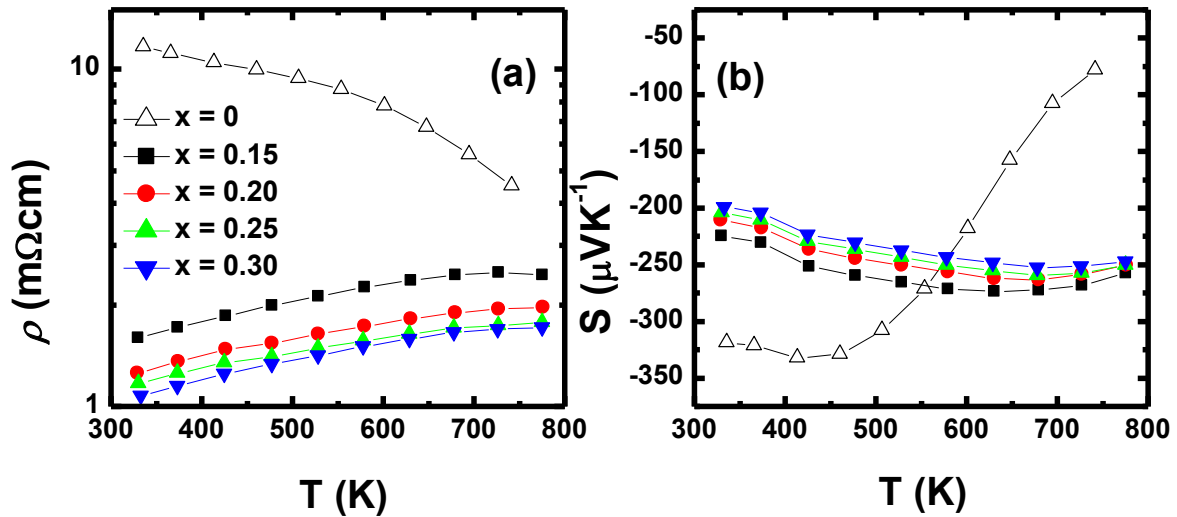

Figure 4.7 (a) Electrical resistivity ρ, (b) Seebeck coefficient S as a function of temperature for polycrystalline samples of $Ga_{0.2}In_xCo_4Sb_{12}$ ($x = 0$, 0.15, 0.20, 0.25, and 0.30). The data of the sample with $x = 0$ was obtained from Ref. [90].

The ρ and S as a function of temperature for the samples with nominal composition $Ga_{0.2}In_xCo_4Sb_{12}$ ($x = 0$, 0.15, 0.20, 0.25, and 0.30) is shown in Figure 3.2.7. The ρ values decreased with increasing x and gradually increased with increasing temperature, which indicates the heavily doped semiconductor behavior. It means that the carrier concentration increases with increasing x. The absolute values of S for all sample show n-type conduction and slightly increase with increasing x except for the sample with $x = 0$. Also, over the entire temperature range, The absolute values of S for the In filled samples have the values between 200 μV/K and 275 μV/K, while that of the sample with $x = 0$ drastically decreases. The maximum S value, the onset of thermal bipolar diffusion, shifted to high temperature with increasing x, indicating that the increase of In filling fraction increases the carrier concentration and impedes the effect of the minority carriers.

As shown in Figure 3.2.8, the n_H increases with increasing x. Hall mobilities of In filled samples is superior to the sample with $x = 0$ and decrease with increasing x. Specifically, the

In in CoSb$_3$ behave as a electron donor and the increase of charge carriers by In addition gives rise to the carrier-carrier scattering which leads to the reduction of Hall mobility.
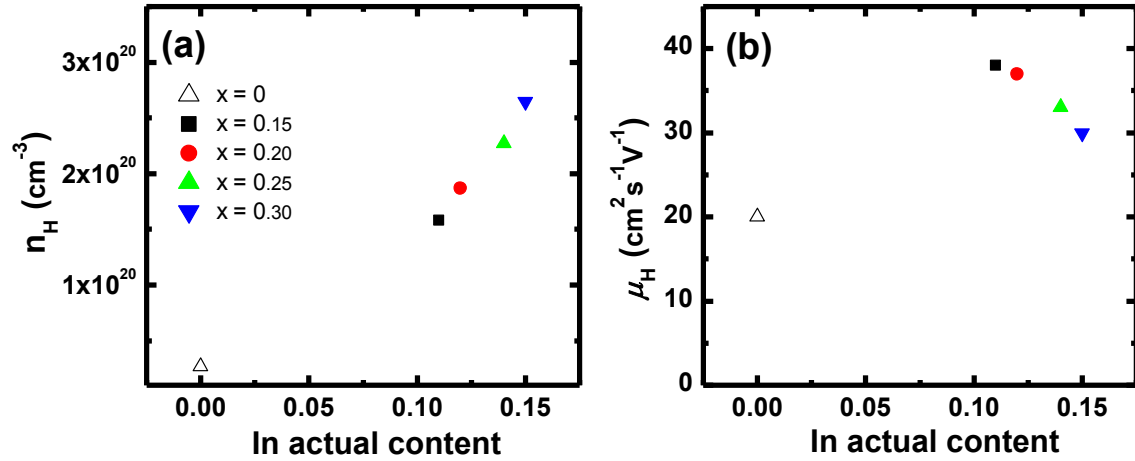

Figure 4.8 Indium content (x) dependences of (a) carrier concentration n_H and (b) carrier mobility μ_H for polycrystalline samples of Ga$_{0.2}$In$_x$Co$_4$Sb$_{12}$ (x = 0, 0.15, 0.20, 0.25, and 0.30) at room temperature.
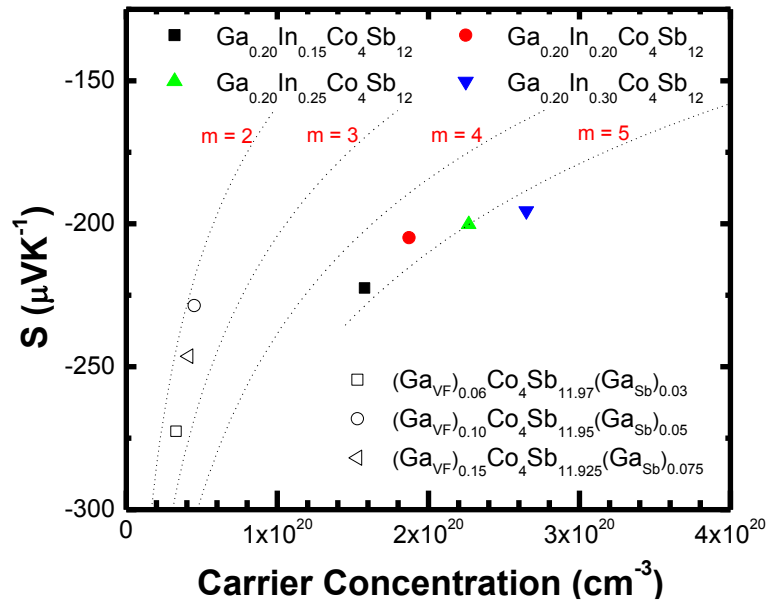
Figure 4.9 Carrier concentration dependence of Seebeck coefficient S for the samples with composition Ga$_{0.2}$In$_x$Co$_4$Sb$_{12}$ (x = 0.15, 0.20, 0.25, and 0.30), (Ga$_{VF}$)$_{0.06}$Co$_4$Sb$_{11.97}$(Ga$_{Sb}$)$_{0.03}$, (Ga$_{VF}$)$_{0.10}$Co$_4$Sb$_{11.95}$(Ga$_{Sb}$)$_{0.05}$, and (Ga$_{VF}$)$_{0.15}$Co$_4$Sb$_{11.925}$(Ga$_{Sb}$)$_{0.075}$ at room temperature.

The room-temperature values of both carrier concentration n_H and Hall mobility μ_H in Figure 4.8 (a) and (b) were measured by the van der Pauw method and the S values at 300K were obtained by extrapolating the S vs T curves in Figure 4.7 (b). Assuming a single parabolic band model dominated by acoustic phonon scattering, we can describe S and true carrier concentration n as follows:[38]

$$S = \frac{k_e}{e}\left\{\eta - \frac{2F_1(\eta)}{F_0(\eta)}\right\}$$ (4.1)

$$n = \sqrt{\frac{2}{\pi}}\left(\frac{m^* k_B T}{\hbar^2}\right)^{3/2} F_{1/2}(\eta)$$ (4.2)

$$F_i(\eta) = \int_0^\infty \frac{x^i dx}{1 + \exp(x - \eta)}$$ (4.3)

Where k_B is the Boltzmann constant, e is the elementary charge, F_i is the Fermi integral of order i, $\eta = E_F/k_B T$ is the reduced chemical potential, m^* is the DOS effective mass of carrier, and $\hbar$ is the reduced Planck constant. The measured Hall carrier concentration n_H is linked to n by $n_H = n / r_H$ with the Hall scattering factor given by $r_H = (1.5F_{0.5}F_{-0.5}) / 2F_0^2$. As mentioned, using room temperature values of the measured transport parameters, we have estimated the reduced effective mass $m = m^* / m_0$, where m_0 is the electron mass. As shown in Figure 4.9, the introduction of In resulted in the significant increase of the m and the m increases with increasing x. As a result, the results of the m and μ_H leaded to the enhancement of $S^2\rho^{-1}$ because the $S^2\rho^{-1}$ is generally proportionate to the weighted mobility $\mu_H m^{3/2}$.

Figure 4.10 (a) and (b) shows the temperature dependence of the thermal conductivity κ and the lattice thermal conductivity κ_{lat}, respectively. The κ_{lat} was calculated by using the Wiedemann-Franz law, i.e. $\kappa_{lat} = \kappa - LT\rho^{-1}$, where L is the Lorentz number (2.45×10^{-8} W Ω K^{-2}). As shown in Figure 4.10 (b), the introduction of In content significantly decreased the κ_{lat}, which resulted from the rattling effect of Ga and In as well as the precipitated nanoparticles. The sample with $x = 0.30$ shows the lowest κ_{lat}, which is due to the scattering of heat carrying phonon by the additional filling of Ga and In.

As a result, as shown in Figure 4.11, the zT increased with increasing In content and the sample with $x = 0.30$ shows the maximum value of 0.95 at 725 K.
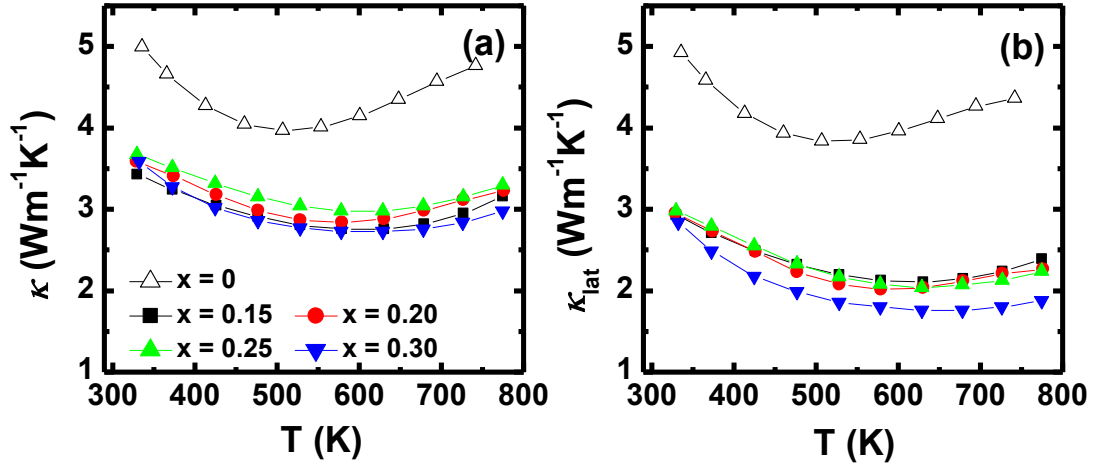
Figure 4.10 (a) Total thermal conductivity κ and (b) the lattice thermal conductivity κ_{lat} (= κ - $LT\rho^{-1}$) as a function of temperature for polycrystalline samples of $Ga_{0.2}In_xCo_4Sb_{12}$ (x = 0, 0.15, 0.20, 0.25, and 0.30).
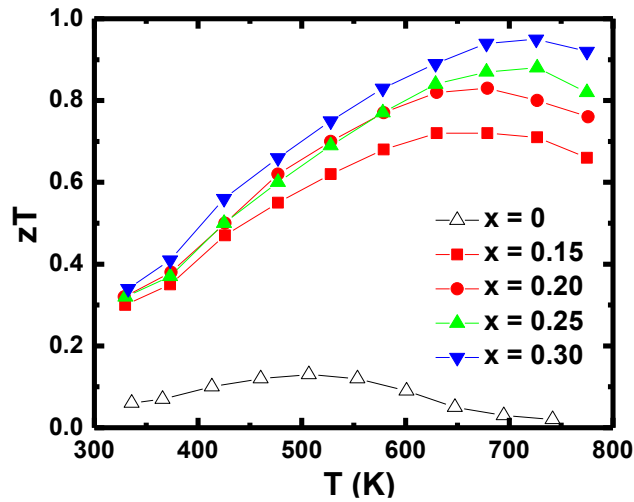

Figure 4.11 Dimensionless figure of merit zT as a function of temperature for polycrystalline samples of $Ga_{0.2}In_xCo_4Sb_{12}$ (x = 0, 0.15, 0.20, 0.25, and 0.30).

4.1.3 Summary

The polycrystalline samples with the nominal composition $Ga_{0.2}In_xCo_4Sb_{12}$ (x = 0.15, 0.20, 0.25, and 0.30) were prepared. All samples have shown the similar morphology in the microstructure and the nano-sized precipitates with the sizes of under around 100 nm at the

grain boundaries. From the crystallographic analyses, we could know that the large amount of In contents can be filled into the voids of skutterudite phases and the small amount of Ga can simultaneously behave as both a filler for the voids and a substituent for Sb site. Both Ga and In contents exceeded the solubility limit formed the nano-sized precipitates with composition (Ga,In)Sb. The In filling significantly-increased the carrier concentration with slight decrease of the carrier mobility, leading to the increase of $S^2\rho^{-1}$. The samples with x = 0.20, 0.25, and 0.30 showed quite high $S^2\rho^{-1}$ in the range of 3.5 to 4.0 mWm^{-1}K^{-2}. The κ_{lat} decreased with increasing In content due to the phonon scattering effects from both of the void filling with In and the (Ga,In)Sb nanoparticles. The enhanced zT values were obtained. The sample with x = 0.30 exhibited the maximum zT of 0.95 at 725 K.

4.2 $Ga_{0.34}In_{0.11}Co_4Sb_{12}$ system

Recently, our group has investigated the microstructures and TE properties of Ga and In co-added $CoSb_3$-based skutterudites.[88] In the previous work, we confirmed the simultaneous filling behaviour of Ga and In in the $CoSb_3$-based skutterudites, indicating the double-filling for the voids and the Ga substitution for Sb sites. Additionally, the nano-precipitates with composition (Ga, In)Sb was confirmed, which came from the excessive Ga and In. As a result, we could get the maximum zT of ~ 0.95 for the Ga and In co-added sample. However, it was not high zT in n-type skutterudite system.[27-29,37,91] In the present study, we have tried to optimize the TE properties of Ga and In co-added $CoSb_3$-based skutterudites. Polycrystalline bulk sample with the nominal composition of $Ga_{0.34}In_{0.11}Co_4Sb_{12}$ were prepared and its phase state and high-temperature TE properties were examined.

4.2.1 Experimental Details

The synthesis of the polycrystalline sample of $Ga_{0.34}In_{0.11}Co_4Sb_{12}$ was prepared from the starting materials, chunks of Ga-In alloy (5N), Co (3N), and Sb (4N). The precursors were carefully weighed out according to the stoichiometric ratio and loaded into the quartz ampoules. The quartz ampoule was sealed under vacuum and transferred into a vertical furnace. The quartz ampoule was heated to 1323 K and kept for 72 h followed by rapid quenching in a water bath. The quenched sample consisting of unstable phases were annealed at 873 K for 1 week to obtain the thermodynamically stable phases. The as-prepared ingots were crushed into fine powders. The as-prepared powders were sintered by spark plasma sintering (SPS) in graphite dies under the pressure of 50 MPa at 923 K for 15 minute in an argon flow atmosphere. Disc shaped bulk sample was prepared for the characterization of microstructure and TE properties.

The X-ray diffraction (XRD) patterns have been collected from the commercial equipment (Ultima IV, Rigaku) with Cu Ka radiation at room temperature. The lattice parameters for all samples were estimated from the least-squares fitting to 2θs, using the standard Si, the external reference material, by utilizing PDXL, Rigaku's diffraction software. The occupancies of elements in matrix phases have been obtained with Rietveld refinement by using Rietan-FP program.[54] The fine-structure and quantitative element analysis for samples has been obtained at room temperature from the Field Emission Scanning Electron Microscopy

(FE-SEM; JEOL, JSM-6500F) with the Energy Dispersive X-ray (EDX) spectroscopy under the vacuum. The Seebeck coefficient S and the electrical resistivity ρ have been obtained by measuring the samples with the column shape in commercial equipment (ZEM-3, ULVAC) in He gas atmosphere. The Hall coefficient (R_H) was measured from the van der Pauw method under an applied magnetic field of 0.5 T in vacuum at room temperature. The Hall carrier concentration (n_H) and Hall mobility (μ_H) were obtained from the R_H based on the assumptions of a single parabolic band model and a Hall factor of 1, i.e., $\mu_H = R_H/\rho$, and $n_H = 1/(eR_H)$, where e is the elementary charge. The thermal diffusivity α obtained on the laser flash method by measuring the samples with the disc shape in commercial equipment (NETZSCH, LFA457) under vacuum. The thermal conductivity $\kappa = \alpha C_p d$ have calculated from the conventional relation $\kappa = \alpha C_p d$, where C_p is the heat capacity from the Durong-Petit model, $C_p = 3nR$, and the d is the density. The densities for the samples have been obtained through the manually taken dimensions and weights.

4.2.2 Results and Discussion

Figure 4.12 shows the FE-SEM and EDX mapping images for the polycrystalline sample with the nominal composition $Ga_{0.34}In_{0.11}Co_4Sb_{12}$ in comparison with the FE-SEM image of $Ga_{0.20}In_{0.15}Co_4Sb_{12}$. As shown in Figure 4.12 (a), (d), and (e), the $Ga_{0.34}In_{0.11}Co_4Sb_{12}$ sample was relatively composed of large grains over 30 μm compared to the $Ga_{0.20}In_{0.15}Co_4Sb_{12}$ sample, which would be due to the further grain growth by the sintering process with high temperature and high pressure. Figure 4.12 (b) and (c) show that the precipitated nanoparticles below 100 nm are in the grain and at the grain boundaries. On the whole, the $Ga_{0.34}In_{0.11}Co_4Sb_{12}$ sample has had smaller nanoparticles than the $Ga_{0.20}In_{0.15}Co_4Sb_{12}$ sample. Based on Chapter 4.1.2, we can consider that the nanoparticles must have composed of (Ga,In)Sb system because the Ga and In content exceeding filling fraction easily form GaSb and InSb by reacting with Sb. Additionally, the EDX mapping images show that the compositions were homogeneously dispersed well, although some Ga not being incorporated into the structure must have pushed out at the grain boundaries.
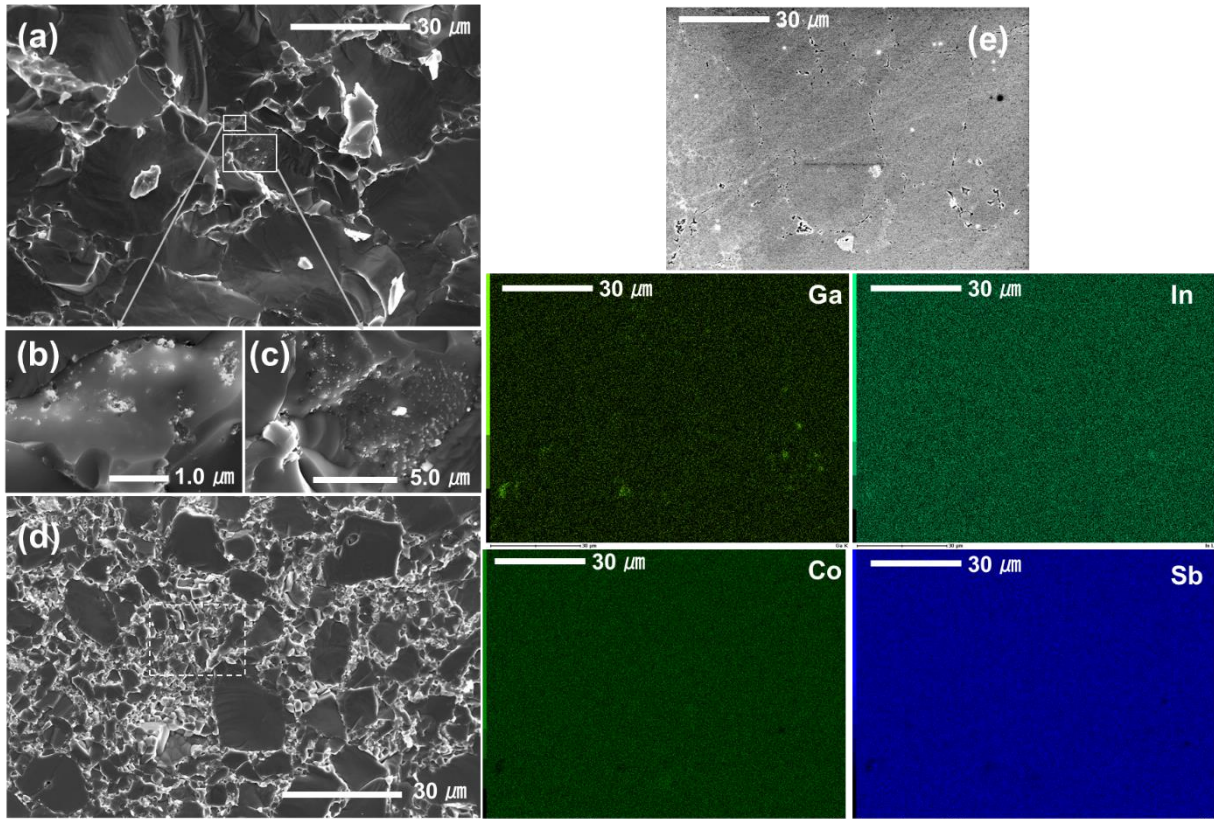
Figure 4.12. FE-SEM images for polycrystalline samples with the nominal compositions of (a), (b), (c), and (e) $Ga_{0.34}In_{0.11}Co_4Sb_{12}$ and (d) $Ga_{0.20}In_{0.15}Co_4Sb_{12}$. EDX mapping images is for (e) a polished sample. (Right) The square dotted area in (d) have shown in Figure 3.2.2.

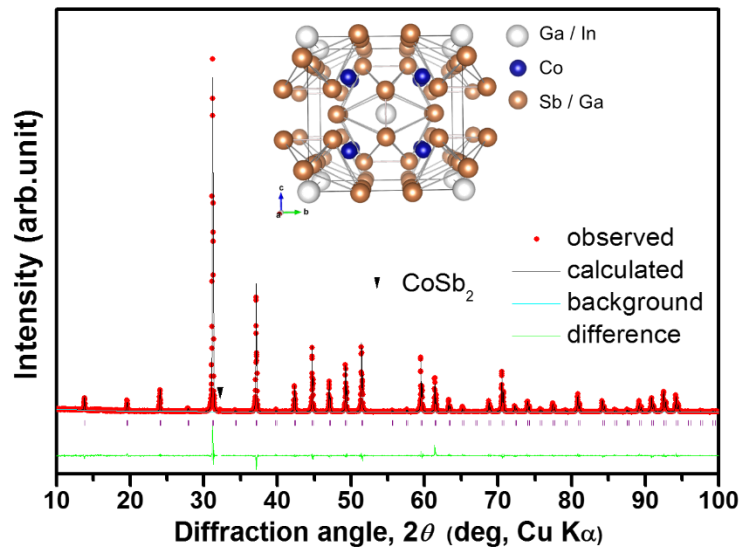Figure 4.13 Powder XRD pattern for $Ga_{0.34}In_{0.11}Co_4Sb_{12}$ polycrystalline sample showing observed, calculated, background, and difference curves at room temperature. The expected peak positions were marked with vertical ticks.

Table 4.5 Lattice parameter *a*, sample bulk density *d*, relative density %T.D., and Rietveld refinement results at room temperature for polycrystalline samples with nominal composition $Ga_{0.34}In_{0.11}Co_4Sb_{12}$. Atomic positions: Ga/In, 2*a* (0, 0, 0); Co, 8*c* (0.25, 0.25, 0.25); Sb, 24*g* (0, *y*, *z*).

Nominal composition	$Ga_{0.34}In_{0.11}Co_4Sb_{12}$
a (nm)	0.9045
d (gcm^{-3})	7.77
%T.D.	98
Rietveld refinement	
Actual composition	$Ga_{0.07}In_{0.10}Co_4Sb_{11.98}$
$(Ga_{VF})/(Ga_{Sb})$	0.043/0.022
Space group	*Im*-3 (#204)
Radiation	Cu *K*α
2θ range (deg.)	10~100
Step width (deg.)	0.02
Counting time (sec./step)	3
U_{iso} (Å) for Ga_{VF} and In	0.0199
U_{iso} (Å) for Co	0.0081
U_{iso} (Å) for Sb and Ga_{Sb}	0.0067
y (Sb)	0.8420
z (Sb)	0.6644
R_B (%)	4.89
R_F (%)	3.80
S	1.24

      Figure 4.13 shows XRD pattern for the $Ga_{0.34}In_{0.11}Co_4Sb_{12}$ sample with the curves obtained from Rietveld refinement. One can see that the calculated pattern is well agreement with the experimentally observed one, where the secondary peak for $CoSb_2$ was excluded for the calculation. For the Rietveld refinement, the assumption in Chapter 4.1.2 was adopted as it

is: Firstly, In can occupy only the void site, while Ga can occupy both the void and Sb sites in the ratio of 2:1.[79] Thus, the refined composition can be set as $(Ga_{VF})_y In_x Co_4 (Ga_{Sb})_{y/2} Sb_{1-y/2}$.[79] Secondly the Ga/In ratio ($= 3y/2x$) was taken from the EDX results for the matrix phases. Thirdly, the values of U_{iso}, the thermal vibration parameter, of both Ga_{VF} and In were assumed to be the equally fixed as that for In in $In_{0.13}Co_4Sb_{12}$ reported by Grytsiv et al.[77] Fourthly, the U_{iso} values of Sb and Ga_{Sb} were postulated as same value because the Sb sites (24g) in the skutterudite structure are covalently bonded and are the stable positions compared with the void site (2a). Finally, the peaks for the (Ga,In)Sb phase were excluded. Since the peaks for the (Ga,In)Sb phase nearly did not overlap with the peaks of the skutterudite phase, the exclusion would not influence on the refinement results.

The Rietveld refinement result for polycrystalline sample with nominal composition $Ga_{0.34}In_{0.11}Co_4Sb_{12}$ is shown in Table 4.5. The result shows that the $Ga_{0.34}In_{0.11}Co_4Sb_{12}$ sample included the dissolved Ga composition more compared to the $Ga_{0.20}In_xCo_4Sb_{12}$ samples. Furthermore, the lattice parameter of the $Ga_{0.34}In_{0.11}Co_4Sb_{12}$ sample was dependent on the In filling fraction, which could understand by comparing with the In-filled skutterudites and Ga-fillled skutterdites.[77,80]
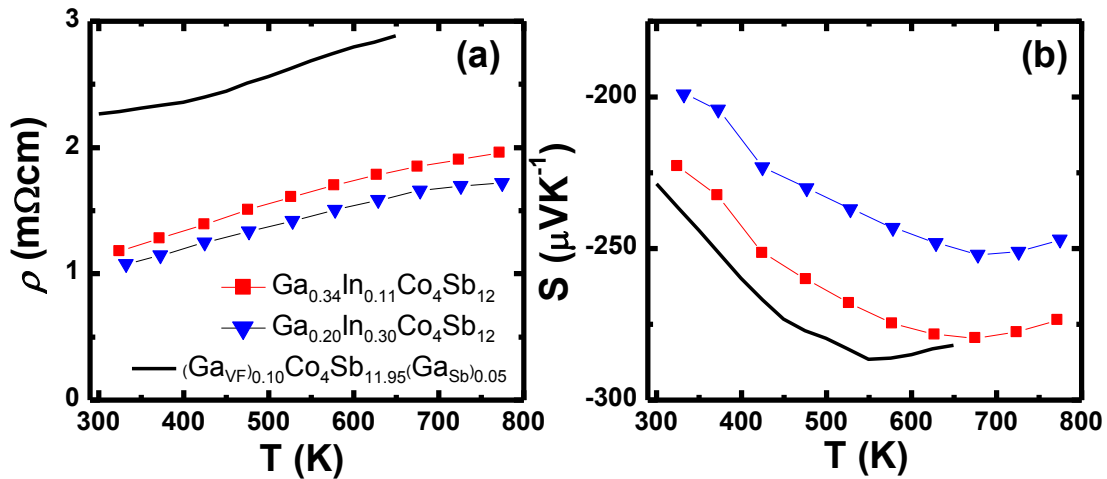
Figure 4.14 (a) Electrical resistivity ρ and (b) Seebeck coefficient S as a function of temperature for the samples with nominal composition $Ga_{0.34}In_{0.11}Co_4Sb_{12}$, $Ga_{0.2}In_{0.30}Co_4Sb_{12}$, and $(Ga_{VF})_{0.10}Co_4Sb_{11.95}(Ga_{Sb})_{0.05}$.

Figure 4.14 shows temperature dependence of ρ and S for the samples with nominal composition $Ga_{0.34}In_{0.11}Co_4Sb_{12}$, $Ga_{0.2}In_{0.30}Co_4Sb_{12}$, and $(Ga_{VF})_{0.10}Co_4Sb_{11.95}(Ga_{Sb})_{0.05}$. Although the $Ga_{0.34}In_{0.11}Co_4Sb_{12}$ sample has slightly higher ρ than the $Ga_{0.2}In_{0.30}Co_4Sb_{12}$ sample due to the low carrier concentration by low In filling fraction, one can see that the In addition is effective to reduce ρ. Also, their ρ shows metallic behaviour increasing with increasing temperature. All samples show n-type conduction and the absolute S of the $Ga_{0.34}In_{0.11}Co_4Sb_{12}$ sample was slightly lower than the $(Ga_{VF})_{0.10}Co_4Sb_{11.95}(Ga_{Sb})_{0.05}$ sample and fairly higher than the $Ga_{0.2}In_{0.30}Co_4Sb_{12}$ sample. Furthermore, the onset of bipolar diffusion shifted to the high temperature, which resulted from the carrier concentration by In filling.
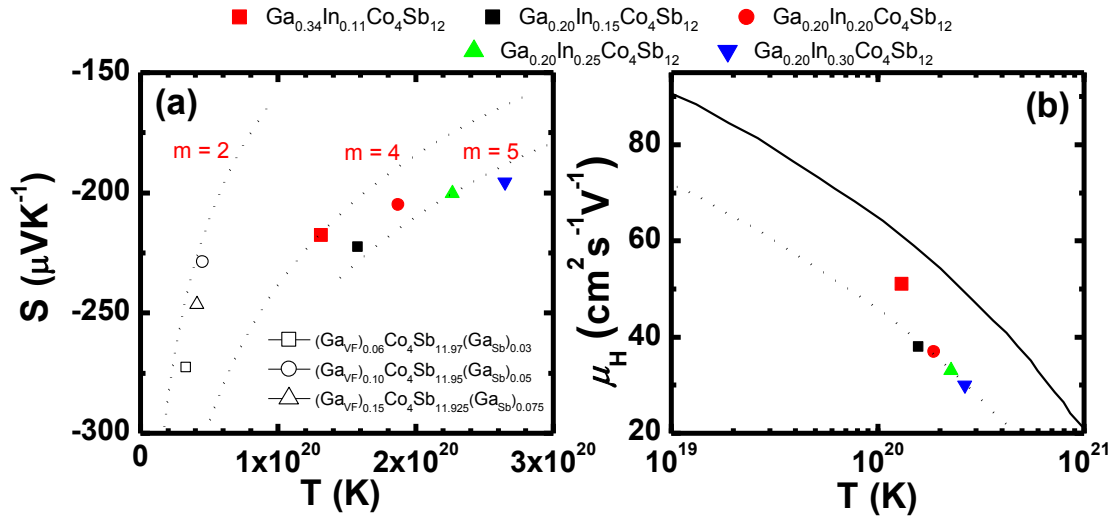
Figure 4.15 Carrier concentration dependence of S and Hall mobility μ_H for the samples with the nominal composition $Ga_{0.34}In_{0.11}Co_4Sb_{12}$, $Ga_{0.2}In_xCo_4Sb_{12}$ ($x = 0, 0.15, 0.20, 0.25, 0.30$), $(Ga_{VF})_{0.06}Co_4Sb_{11.97}(Ga_{Sb})_{0.03}$, $(Ga_{VF})_{0.10}Co_4Sb_{11.95}(Ga_{Sb})_{0.05}$, and $(Ga_{VF})_{0.15}Co_4Sb_{11.925}(Ga_{Sb})_{0.075}$.

The room-temperature values of both carrier concentration n_H and Hall mobility μ_H in Figure 4.15 (a) and (b) were measured by the van der Pauw method and the S values at 300 K were obtained by extrapolating the S vs T curves in Figure 4.14(b). Meanwhile, it is possible to calculate the carrier effective mass (m^*) from the experimental results of the S and n_H. Thus, we estimated the reduced effective mass, $m = m^*/m_0$, of the carriers using a single parabolic

band model based on Fermi statistics, where m_0 is the free electron mass. The S, carrier concentration p, and Fermi integral $F_i(\eta)$ can be expressed as:[92]

$$S = \frac{k_e}{e}\left\{\eta - \frac{(2+r)F_{1+r}(\eta)}{(1+r)F_r(\eta)}\right\} \tag{4.4}$$

$$p = \sqrt{\frac{2}{\pi}}\left(\frac{m^*k_BT}{\hbar^2}\right)^{3/2}F_{1/2}(\eta) \tag{4.5}$$

$$F_i(\eta) = \int_0^\infty \frac{x^i dx}{1+\exp(x-\eta)} \tag{4.6}$$

Where k_B is Boltzmann constant, r is the exponent of the energy dependence of the hole mean free path, $\eta = E_F/k_BT$ is the reduced chemical potential, and $\hbar$ is reduced Planck constant. According to the carrier scattering mechanism, one can postulate the r values as $r = 0$ for both acoustic phonon scattering and alloy disorder scattering, $r = 2$ for scattering by ionized impurities. Here we introduced $r = 0$ of the former mechanism. The m values of both Ga doped samples and Ga/In co-added samples were shown in Figure 4.15 (a) and those values were even larger than $m = 0.175$ of an undoped-$CoSb_3$.[93] Fundamentally, both curvature and multiplicity of bands near the energy gap are the main features in the electronic band structure that determines transport properties of charge carriers in semiconductors. On the point of view, as shown in Figure 4.15 (a), it could be described that the addition of In content might lead to the introduction of In 5p state with a large curvature into the conduction band, which resulted in the large effective mass as well as the increase of carrier concentration.[78] Furthermore, the rise of the Fermi level by the band convergence may increase the entropy of the charge carriers and the energy degeneracy, restraining the reduction of the Seebeck coefficient. As shown in Figure 4.15 (b), the μ_H value of the $Ga_{0.34}In_{0.11}Co_4Sb_{12}$ sample was higher than those of the $Ga_{0.2}In_xCo_4Sb_{12}$ samples, although they located below a trend line for the single- and multiple-filled n-type skutterudites.[80] It can be understood from the discrepancy of grain sizes between both of them. As shown in Figure 4.12 (a) and (d), one can consider that the mean free path of charge carriers in the $Ga_{0.34}In_{0.11}Co_4Sb_{12}$ sample were larger than that in the $Ga_{0.2}In_xCo_4Sb_{12}$ samples due to the larger grain size, which leaded to the increase of the μ_H value. As shown in Figure 4.14 (a), it resulted in the increase of ρ. Thus, as shown in Figure 4.16, the results leaded to the enhancement of power factor ($S^2\rho^{-1}$) because the $S^2\rho^{-1}$ is generally proportionate to $\mu_H(m^*)^{3/2}$.[24]
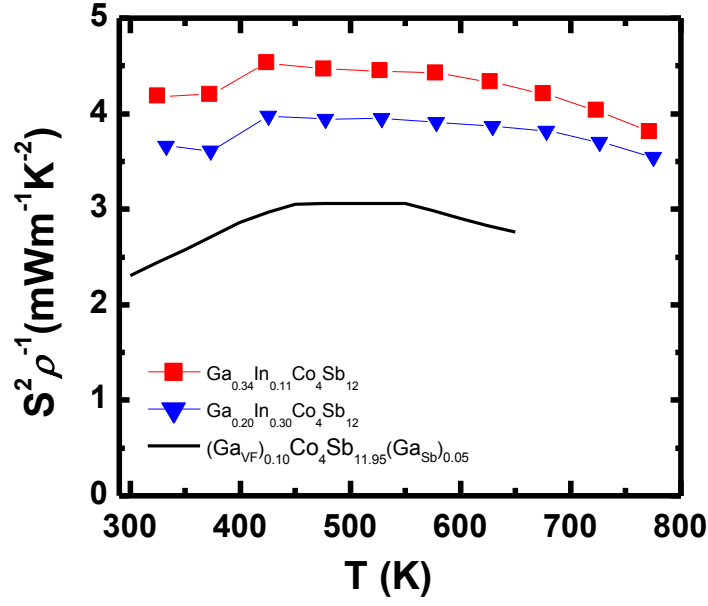
Figure 4.16 Power Factor $S^2\rho^{-1}$ as a function of temperature for the samples with nominal composition $Ga_{0.34}In_{0.11}Co_4Sb_{12}$, $Ga_{0.2}In_{0.30}Co_4Sb_{12}$, and $(Ga_{VF})_{0.10}Co_4Sb_{11.95}(Ga_{Sb})_{0.05}$.
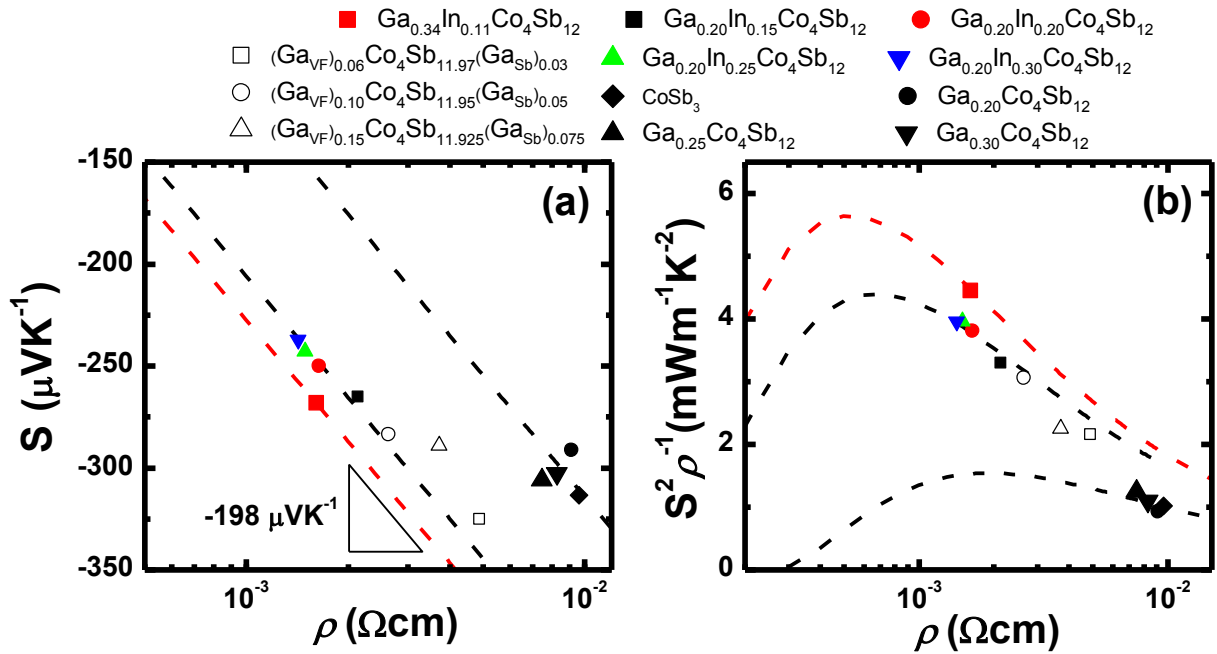

Figure 4.17 Electrical resistivity dependence of S and $S^2\rho^{-1}$ for Ga-filled and Ga/In co-filled skutterudites.(The calculation for dot lines was performed based on Ref. [94])

Figure 4.17 shows the $Ga_{0.34}In_{0.11}Co_4Sb_{12}$ sample has an excellent electrical properties despite of the low carrier concentration. Furthermore, it is predicted that the $Ga_{0.34}In_{0.11}Co_4Sb_{12}$ sample could ideally obtain the high power factor of 5.6 mWm^{-1}K^{-1} at 5×10^{-4}Ωcm.
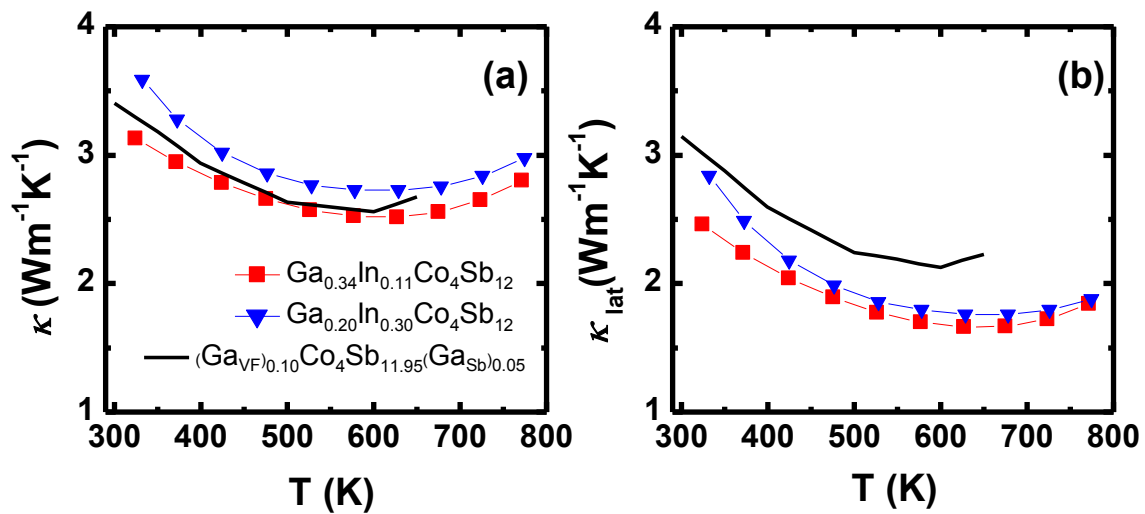
Figure 4.18 (a) Thermal conductivity κ and (b) lattice thermal conductivity κ_{lat} as a function of temperature for the samples with nominal composition $Ga_{0.34}In_{0.11}Co_4Sb_{12}$, $Ga_{0.2}In_{0.30}Co_4Sb_{12}$, and $(Ga_{VF})_{0.10}Co_4Sb_{11.95}(Ga_{Sb})_{0.05}$.

Figure 4.18 (a) and (b) shows the temperature dependence of the thermal conductivity κ and the lattice thermal conductivity κ_{lat}, respectively. The κ_{lat} was calculated by using the Wiedemann-Franz law, i.e. $\kappa_{lat} = \kappa - LT\rho^{-1}$, where L is the Lorentz number (2.45×10^{-8} W Ω K^{-2}). Figure 4.19 (a) and (b) shows the inverse temperature dependence of κ_{lat} and κ, κ_{lat}, respectively. As shown in Figure 4.3 and 4.12, the $Ga_{0.34}In_{0.11}Co_4Sb_{12}$ sample shows the lowest κ_{lat} despite of the large-sized grains and small amount of nanoparticles compared to the $Ga_{0.2}In_xCo_4Sb_{12}$ samples. As shown in Table 4.4 and 4.5, one can understand that it results from the increase of the Ga solubility for the CoSb$_3$. On the other hand, all samples have the considerable contribution of the bipolar diffusion by the intrinsic excitation. The bipolar diffusion contribution in thermal conductivity can be expressed as equation (3.2).
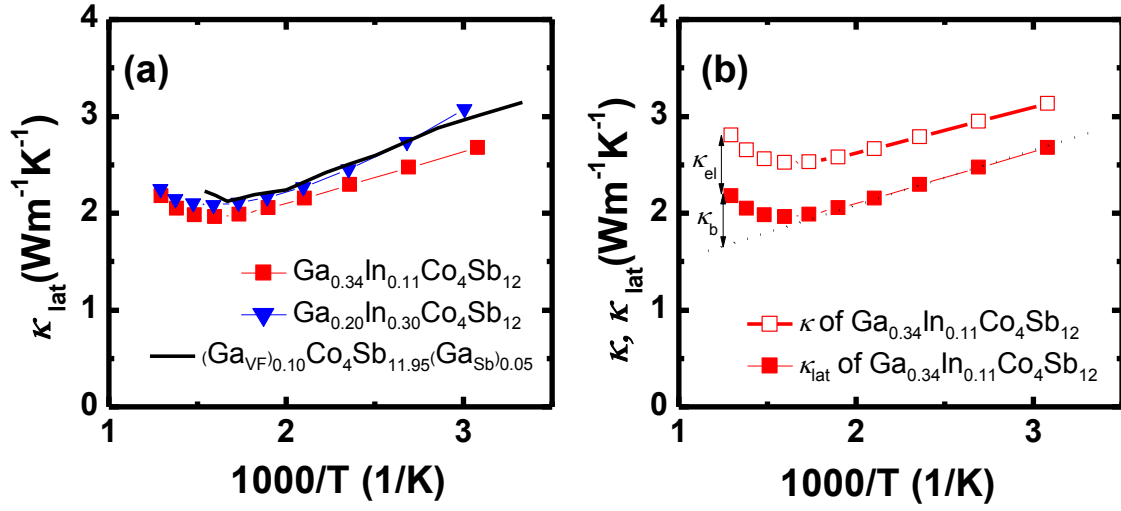
Figure 4.19 (a) κ and (b) κ, κ_{lat} as a function of inverse temperature for the samples with nominal composition $Ga_{0.34}In_{0.11}Co_4Sb_{12}$, $Ga_{0.2}In_{0.30}Co_4Sb_{12}$, and $(Ga_{VF})_{0.10}Co_4Sb_{11.95}(Ga_{Sb})_{0.05}$.
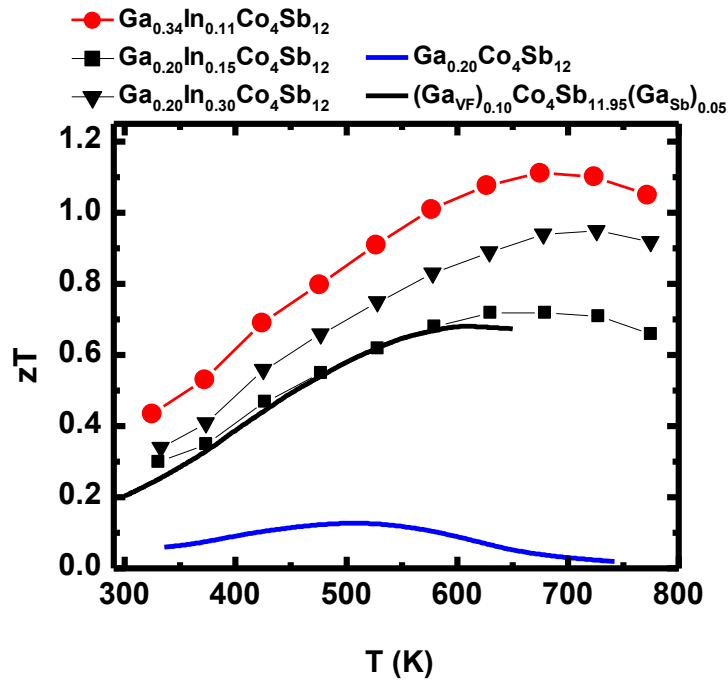

Figure 4.20 (a) Thermal conductivity κ and (b) lattice thermal conductivity κ_{lat} as a function of temperature for the samples with nominal composition $Ga_{0.34}In_{0.11}Co_4Sb_{12}$, $Ga_{0.2}In_{0.15}Co_4Sb_{12}$, $Ga_{0.2}In_{0.30}Co_4Sb_{12}$, and $(Ga_{VF})_{0.10}Co_4Sb_{11.95}(Ga_{Sb})_{0.05}$.

Finally, Figure 4.20 shows temperature dependence of dimensionless figure of merit zT. The sample with composition $Ga_{0.34}In_{0.11}Co_4Sb_{12}$ exhibited the best zT values among all samples and the maximum zT value was 1.11 at 675 K which is put into the intermediate

temperature range for the module application in the automobile system as mentioned in Chapter 1.4 (page16).

4.2.3 Summary

The sample with the nominal composition $Ga_{0.34}In_{0.11}Co_4Sb_{12}$ was synthesized using a melt-quench-anneal-SPS method and its TE properties were investigated with other Ga and In added samples. From both the Rietveld and the SEM-EDX analyses, we confirmed that Ga and In were filled into voids at the same time and a small amount of Ga substituted for Sb at the Sb sites of $CoSb_3$. On the other hand, both Ga and In which exceeded the filling limit formed (Ga,In)Sb nano-sized precipitates at the grain boundary and in the grain of the polycrystalline sample. Furthermore, the optimization of both microstructure and chemical composition leaded to the significant improvement of TE properties. As a result, the $Ga_{0.34}In_{0.11}Co_4Sb_{12}$ sample exhibited the maximum zT of 1.11 at 675 K.

CHAPTER V

Summary

The present thesis have investigated on group 13 elements (Ga, In, Tl)-added p-type and n-type filled skutterudite compounds. It have been studied how the crystallographic modification has an influence on the thermoelectric (TE) properties.

First of all, we have investigated on two sort of Tl-filled p-type skutterudites whose repots have been limited. Firstly, we paid attention to Co substitution by other transition metals, because it is favorable for the mass production. Thus, the crystallographic and TE properties of both polycrystalline samples of $Tl_xFe_{2.5}Ni_{1.5}Sb_{12}$ and $Tl_xFe_{1.5}Co_{2.5}Sb_{12}$ were investigated. We could obtain the precise crystal structures and occupancies of the Tl atoms within the skutterudite matrix phase for the compounds through the Rietveld refinement using the ratio of the transition metals (Fe/Ni and Fe/Co) obtained from the quantitative EDX analysis. Thus, we have confirmed that the actual Tl filling fraction increased with increasing the nominal Tl fraction and also modified the ratio of the transition metals. The Tl filling was favorable for TE properties, because it contributed the enhancement of electrical properties as a electron donor and the scattering of heat carrying phonon as a rattler. Furthermore, the compounds with the high Fe fraction have showed the high p-type performance, which means that the Co substitution by the Fe for skutterudite matrix phase is effective for the enhancement of TE properties as much as the Tl filling.

Secondly, we have investigated on Ga and In co-added n-type filled skutterudites. In order to obtain the precise crystal structure and the occupancies of elements, the Rietveld refinement was performed using the Ga/In ratio obtained from the quantitative EDX analysis. From the results, we confirmed that Ga and In were filled into voids at the same time and a small amount of Ga substituted for Sb at the Sb sites of $CoSb_3$. Furthermore, we could observed the precipitated nano-sized particles that was formed by reacting the excessive Ga and In content with Sb. For the $Ga_{0.2}In_xCo_4Sb_{12}$ systems, it is confirmed that, as the increase of nominal In content, the Ga filling fraction was nearly fixed and the In filling fraction increased. Thus, we could understand that the In filled into voids of the skutterudite matrix phase played an dominant role as a carrier donor and the scattering point of heat carrying phonon.

Furthermore, the nanoparticles of (Ga,In)Sb sysptem and the Ga forming dual-defects in skutterudite matrix phases is expected to reduce the lattice thermal conductivity. From the result, we could obtain the zT of unity. Through the additional study, we could know that the sample with nominal composition $Ga_{0.34}In_{0.11}Co_4Sb_{12}$ shows the enhanced zT. The grain growth resulted in the enhancement of electrical properties without degrading thermal conductivity, leading to the increase of zT. On the other hand, we can systematically understand the enhancement of zT by the addition of both Ga and In for $CoSb_3$-based skutterudites. As shown in Figure 5.1, It can be explained by comparing the maximum zT values of the present study with the reported results mentioned before. Firstly, as the first reported result, the lowest zT of this single filled sample, $Ga_{0.20}Co_4Sb_{12}$,[95] is due to Small amounts of the filled Ga and the micrometer scale Ga metal precipitates. Secondly, as the second reported result, this sample, $(Ga_{VF})_{0.10}Co_4Sb_{11.95}(Ga_{Sb})_{0.05}$,[79] have shown dramatic improvement of zT which was due to Dual site occupancy of Ga. Thirdly, for the $Ga_{0.20}In_{0.30}Co_4Sb_{12}$ sample in the present study, the filling of In and nano-sized precipitates led to the additional improvement. And finally, for the $Ga_{0.34}In_{0.11}Co_4Sb_{12}$ sample in the present study, through the optimization of both microstructure and chemical composition, we could obtain zT over unity.
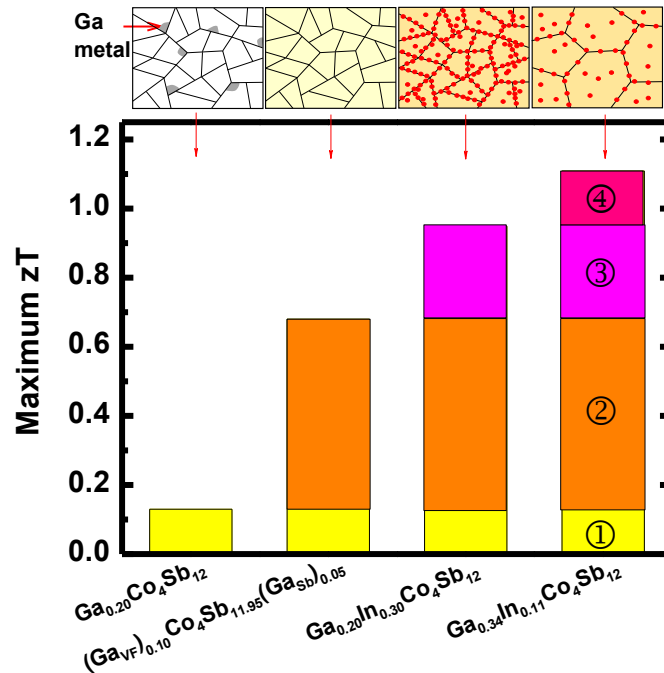

Figure 5.1 Comparison of maximum zT values for Ga and In added $CoSb_3$ based skutterudites.

Conclusion

The present dissertation has aimed to study the behavior of group 13 elements (Ga, In, Tl) in both *p*-type and *n*-type skutterudites. In particular, the behavior of both Ga and In co-added in the *n*-type skutterudite was crystallographically investigated, which was firstly revealed by the experimental results obtained from XRD-Rietveld method in the present study.
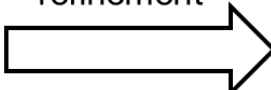
<table>
<tr><td>Nominal
composition</td><td></td><td>Actual composition
(Refined composition)</td></tr>
<tr><td>$Ga_{0.20}In_{0.15}Co_4Sb_{12}$</td><td rowspan="5">Rietveld
refinement →</td><td>$(Ga_{VF})_{0.019}In_{0.11}Co_4Sb_{11.991}(Ga_{Sb})_{0.009}$</td></tr>
<tr><td>$Ga_{0.20}In_{0.20}Co_4Sb_{12}$</td><td>$(Ga_{VF})_{0.020}In_{0.12}Co_4Sb_{11.990}(Ga_{Sb})_{0.010}$</td></tr>
<tr><td>$Ga_{0.20}In_{0.25}Co_4Sb_{12}$</td><td>$(Ga_{VF})_{0.021}In_{0.14}Co_4Sb_{11.990}(Ga_{Sb})_{0.010}$</td></tr>
<tr><td>$Ga_{0.20}In_{0.30}Co_4Sb_{12}$</td><td>$(Ga_{VF})_{0.024}In_{0.15}Co_4Sb_{11.988}(Ga_{Sb})_{0.012}$</td></tr>
<tr><td>$Ga_{0.34}In_{0.11}Co_4Sb_{12}$</td><td>$(Ga_{VF})_{0.043}In_{0.10}Co_4Sb_{11.978}(Ga_{Sb})_{0.022}$</td></tr>
</table>

Figure 5.2 Refinement of chemical composition by Rietveld method

In the conventional study, the TE properties of skutterudites were mainly explained on the basis of the simple analysis of XRD and FE-SEM with nominal composition. In the present study, we have tried to precisely observe the chemical composition and crystal structure from XRD-Rietveld method as well as the SEM-EDX analysis. After then it has been reflected into the analysis of TE properties of skutterudites.
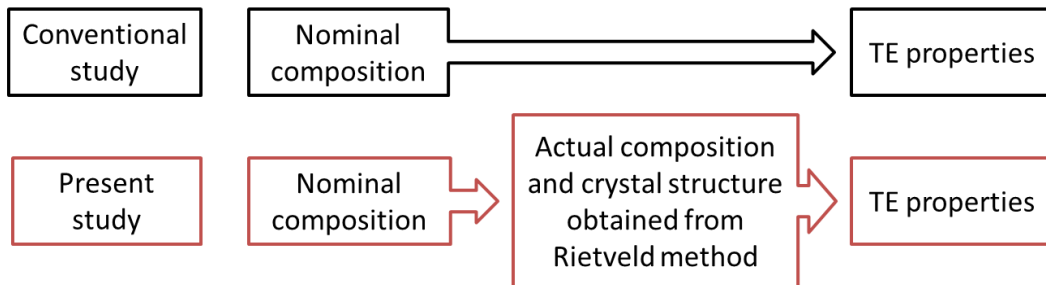

Figure 5.3 Comparison of analysis sequences for the conventional and the present studies.

From the study, we could understand the behavior of both Ga and In in $CoSb_3$ skutterudites at the very first as followings; Firtsly, a large part of In content occupied the void sites. At the same time, Ga occupied both void sites and Sb sites, which form the charge compensation. Secondly, Ga and In exceeding solubility for skutterudites form the nano-sized precipitates with composition (Ga,In)Sb by reacting Sb. The crystallographic information made understand TE properties of all samples.

On the other hand, to develop TE module, we need not only *n*-type materials but also *p*-type materials. Tl was located well into void site of skutterudite structure, which have shown excellent performances as a hole compensation source and a rattler. However, since Tl is so toxic and easily oxidized in the air, we have to research the non-toxic and inoxidizable filler candidates. Both Ga and In are non-toxic and very stable in the air and thus they are suitable for mass production. Their unusual behavior such as Sb-substitution in skutterudite structure may provide the chemical degrees of freedom necessary for further enhancement of TE properties. In the point of view, Ga and In would be a promising filler candidates for *p*-type skutterudites. Furthermore, both In and Ga have shown excellent performances in *n*-type filled skutterudites. However, for the application the reports of high temperature TE for In and Ga filled *p*-type skutterudites have been limited. Thus, we need to investigate the TE properties of (In, Ga)-filled *p*-type skutterudites.

References

[1]   G. J. Snyder and E. S. Toberer, Nature Materials **7,** 105 (2008).

[2]   D. M. Rowe, *CRC handbook of thermoelectrics* (Boca Raton, FL, CRC Press, 1995).

[3]   G. Chen, M. S. Dresselhaus, G. Dresselhaus, J. P. Fleurial, and T. Caillat, International Materials Reviews **48,** 45 (2003).

[4]   M. S. Dresselhaus, G. Chen, M. Y. Tang, R. G. Yang, H. Lee, D. Z. Wang, Z. F. Ren, J. P. Fleurial, and P. Gogna, Advanced Materials **19,** 1043 (2007).

[5]   F. J. DiSalvo, Science **285,** 703 (1999).

[6]   F. M. Andrew and G. J. Snyder, in *Materials, Preparation, and Characterization in Thermoelectrics* (CRC Press, 2012), p. 1.

[7]   Y. Pei, A. D. LaLonde, N. A. Heinz, X. Shi, S. Iwanaga, H. Wang, L. Chen, and G. J. Snyder, Advanced Materials **23,** 5674 (2011).

[8]   C. B. Vining, Journal of Applied Physics **69,** 331 (1991).

[9]   B. Abeles, Physical Review **131,** 1906 (1963).

[10]   P. G. Klemens, Proceedings of the Royal Society of London. Series A. Mathematical and Physical Sciences **208,** 108 (1951).

[11]   J. Salvador, J. Cho, Z. Ye, J. Moczygemba, A. Thompson, J. Sharp, J. König, R. Maloney, T. Thompson, J. Sakamoto, H. Wang, A. Wereszczak, and G. Meisner, Journal of Electronic Materials **42,** 1389 (2013).

[12]   J. Yang and F. Stabler, Journal of Electronic Materials **38,** 1245 (2009).

[13]   B. C. Sales, D. Mandrus, B. C. Chakoumakos, V. Keppens, and J. R. Thompson, Physical Review B **56,** 15081 (1997).

[14]   G. S. Nolas, D. T. Morelli, and T. M. Tritt, Annual Review of Materials Science **29,** 89 (1999).

[15]   B. C. Chakoumakos and B. C. Sales, Journal of Alloys and Compounds **407,** 87 (2006).

[16]   R. P. Hermann, R. Jin, W. Schweika, F. Grandjean, D. Mandrus, B. C. Sales, and G. J. Long, Physical Review Letters **90,** 135505 (2003).

[17]   H. Kitagawa, M. Hasaka, T. Morimura, H. Nakashima, and S.-i. Kondo, Materials Research Bulletin **35,** 185 (2000).

[18]   L. D. Chen, T. Kawahara, X. F. Tang, T. Goto, T. Hirai, J. S. Dyck, W. Chen, and C. Uher, Journal of Applied Physics **90,** 1864 (2001).

[19]   X. Y. Zhao, X. Shi, L. D. Chen, W. Q. Zhang, W. B. Zhang, and Y. Z. Pei, Journal of Applied Physics **99** (2006).

[20]   Y. Z. Pei, L. D. Chen, W. Zhang, X. Shi, S. Q. Bai, X. Y. Zhao, Z. G. Mei, and X. Y. Li, Applied Physics Letters **89,** 221107 (2006).

[21]   J. Yang, W. Zhang, S. Q. Bai, Z. Mei, and L. D. Chen, Applied Physics Letters **90** (2007).

[22]   X. Shi, H. Kong, C.-P. Li, C. Uher, J. Yang, J. R. Salvador, H. Wang, L. Chen, and W. Zhang, Applied Physics Letters **92** (2008).

[23]   X. Shi, J. R. Salvador, J. Yang, and H. Wang, Journal of Electronic Materials **38,** 930 (2009).

[24]   R. Liu, P. Qiu, X. Chen, X. Huang, and L. Chen, Journal of Materials Research **26,** 1813 (2011).

[25]   M. Puyet, B. Lenoir, A. Dauscher, C. Candolfi, J. Hejtmanek, C. Stiewe, and E. Müller, Applied Physics Letters **101,** 222105 (2012).

[26]   R. Liu, J. Y. Cho, J. Yang, W. Zhang, and L. Chen, Journal of Materials Science & Technology **30,** 1134 (2014).

[27]   G. Rogl, A. Grytsiv, P. Rogl, E. Bauer, M. Hochenhofer, R. Anbalagan, R. C. Mallik, and E. Schafler, Acta Materialia **76,** 434 (2014).

[28]   Y. Tang, R. Hanus, S.-w. Chen, and G. J. Snyder, Nat Commun **6** (2015).

[29]   Y. Tang, S.-w. Chen, and G. J. Snyder, Journal of Materiomics **1,** 75 (2015).

[30]   M. Rull-Bravo, A. Moure, J. F. Fern?ndez, and M. Mart?n-Gonz?lez, RSC Advances **5,** 41653 (2015).

[31]   R. Liu, J. Yang, X. Chen, X. Shi, L. Chen, and C. Uher, Intermetallics **19,** 1747 (2011).

[32]   K.-H. Park, S.-W. You, S.-C. Ur, I.-H. Kim, S.-M. Choi, and W.-S. Seo, Journal of Electronic Materials **41,** 1051 (2012).

[33]   P. F. Qiu, J. Yang, R. H. Liu, X. Shi, X. Y. Huang, G. J. Snyder, W. Zhang, and L. D. Chen, Journal of Applied Physics **109** (2011).

[34]   G. Rogl, A. Grytsiv, E. Bauer, P. Rogl, and M. Zehetbauer, Intermetallics **18,** 57 (2010).

[35]   A. Harnwunggmoung, K. Kurosaki, A. Kosuga, M. Ishimaru, T. Plirdpring, R. Yimnirun, J. Jutimoosik, S. Rujirawat, Y. Ohishi, H. Muta, and S. Yamanaka, Journal of Applied Physics **112,** 043509 (2012),/.

[36]   K. Kurosaki, G. Li, Y. Ohishi, H. Muta, and S. Yamanaka, Frontiers in Chemistry **2,** 84 (2014).

[37]   H. Li, X. Tang, Q. Zhang, and C. Uher, Applied Physics Letters **94,** 102114 (2009).

[38]   X. Su, H. Li, Y. Yan, H. Chi, X. Tang, Q. Zhang, and C. Uher, Journal of Materials Chemistry **22,** 15628 (2012).

[39]   A. Harnwunggmoung, K. Kurosaki, H. Muta, and S. Yamanaka, Applied Physics Letters **96** (2010).

[40]   G. Li, K. Kurosaki, Y. Ohishi, H. Muta, and S. Yamanaka, Journal of Electronic Materials **42,** 1463 (2013).

[41]   B. C. Sales, B. C. Chakoumakos, and D. Mandrus, Physical Review B **61,** 2475 (2000).

[42]   D. Kim, K. Kurosaki, Y. Ohishi, H. Muta, and S. Yamanaka, APL Materials **1** (2013).

[43]   K. Yang, H. Cheng, H. H. Hng, J. Ma, J. L. Mi, X. B. Zhao, T. J. Zhu, and Y. B. Zhang, Journal of Alloys and Compounds **467,** 528 (2009).

[44]   J. R. Salvador, J. Yang, H. Wang, and X. Shi, Journal of Applied Physics **107** (2010).

[45]   L. Xi, J. Yang, C. Lu, Z. Mei, W. Zhang, and L. Chen, Chemistry of Materials **22,** 2384 (2010).

[46]   A. Harnwunggmoung, K. Kurosaki, Y. Ohishi, H. Muta, and S. Yamanaka, in *Thermoelectric properties of (Ga, Tl) double-filled skutterudites*, Pacifico Yokohama, Japan, 2012.

[47]   J. Peng, W. Xu, Y. Yan, J. Yang, L. Fu, H. Kang, and J. He, Journal of Applied Physics **112,** 024909 (2012).

[48]   W. Xu, J. Peng, J. He, M. Zhou, J. Yang, and L. Fu, Journal of Wuhan University of Technology-Mater. Sci. Ed. **28,** 677 (2013).

[49]   J. Graff, J. He, and T. Tritt, Inorganics **2,** 168 (2014).

[50]   A. Harnwunggmoung, Thesis, Osaka University, 2011.

[51]   H. Okamoto, Journal of Phase Equilibria **12,** 244 (1991).

[52]   Wikipedia, en.wikipedia.org/wiki/Crystal (2015).

[53]   J. Gilfrich, X-Ray Spectrometry **22,** 119 (1993).

[54]   F. Izumi and K. Momma, Solid State Phenomena **130,** 15 (2007).

[55]   L. J. v. d. Pauw, Philips Tech. Rev. **20,** 220 (1958).

[56]   G. A. Slack, Solid State Physics **Volume 34,** 1 (1979).

[57]   A. Möchel, I. Sergueev, N. Nguyen, G. J. Long, F. Grandjean, D. C. Johnson, and R. P. Hermann, Physical Review B **84,** 064302 (2011).

[58]   D. R. Thompson, C. Liu, J. Yang, J. R. Salvador, D. B. Haddad, N. D. Ellison, R. A. Waldo, and J. Yang, Acta Materialia **92,** 152 (2015).

[59]   J. Leszczynski, A. Dauscher, P. Masschelein, and B. Lenoir, Journal of Electronic Materials **39,** 1764 (2010).

[60]   P. F. Qiu, R. H. Liu, J. Yang, X. Shi, X. Y. Huang, W. Zhang, L. D. Chen, J. Yang, and D. J. Singh, Journal of Applied Physics **111** (2012).

[61]   R. P. Hermann, F. Grandjean, and G. J. Long, American Journal of Physics **73,** 110 (2005).

[62]   G. Li, K. Kurosaki, Y. Ohishi, H. Muta, and S. Yamanaka, MATERIALS TRANSACTIONS **55,** 1232 (2014).

[63]   S. Choi, K. Kurosaki, Y. Ohishi, H. Muta, and S. Yamanaka, Journal of Applied Physics **115** (2014).

[64]   S. Choi, K. Kurosaki, A. Yusufu, Y. Ohishi, H. Muta, and S. Yamanaka, Journal of Electronic Materials **44,** 1743 (2015).

[65]   G. Yoon, H. Sellinschegg, and D. C. Johnson, Thermochimica Acta **388,** 151 (2002).

[66]   H. J. Goldsmid and J. W. Sharp, Journal of Electronic Materials **28,** 869 (1999).

[67]   Z. M. Gibbs, H.-S. Kim, H. Wang, and G. J. Snyder, Applied Physics Letters **106,** 022112 (2015).

[68]   J. Young Cho, Z. Ye, M. M. Tessema, J. R. Salvador, R. A. Waldo, J. Yang, W. Zhang, J. Yang, W. Cai, and H. Wang, Journal of Applied Physics **113,** 143708 (2013).

[69]   J. Y. Cho, Z. Ye, M. M. Tessema, R. A. Waldo, J. R. Salvador, J. Yang, W. Cai, and H. Wang, Acta Materialia **60,** 2104 (2012).

[70]   D. Bérardan, E. Alleno, C. Godart, M. Puyet, B. Lenoir, R. Lackner, E. Bauer, L. Girard, and D. Ravot, Journal of Applied Physics **98,** 033710 (2005).

[71]   Y. Dong, P. Puneet, T. M. Tritt, and G. S. Nolas, Journal of Solid State Chemistry **209,** 1 (2014).

[72]   G. Rogl, D. Setman, E. Schafler, J. Horky, M. Kerber, M. Zehetbauer, M. Falmbigl, P. Rogl, E. Royanian, and E. Bauer, Acta Materialia **60,** 2146 (2012).

[73]   G. Rogl, A. Grytsiv, M. Falmbigl, E. Bauer, P. Rogl, M. Zehetbauer, and Y. Gelbstein, Journal of Alloys and Compounds **537,** 242 (2012).

[74]   G. Philippe and V. Marek, Journal of Physics: Condensed Matter **19,** 096002 (2007).

[75]   J. Yang, G. P. Meisner, D. T. Morelli, and C. Uher, Physical Review B **63,** 014410 (2000).

[76]   X. Shi, W. Zhang, L. D. Chen, and J. Yang, Physical Review Letters **95,** 185503 (2005).

[77]   A. Grytsiv, P. Rogl, H. Michor, E. Bauer, and G. Giester, Journal of Electronic Materials **42,** 2940 (2013).

[78]   J. Leszczynski, V. D. Ros, B. Lenoir, A. Dauscher, C. Candolfi, P. Masschelein, J. Hejtmanek, K. Kutorasinski, J. Tobola, R. I. Smith, C. Stiewe, and E. Müller, Journal of Physics D: Applied Physics **46,** 495106 (2013).

[79]   Y. Qiu, L. Xi, X. Shi, P. Qiu, W. Zhang, L. Chen, J. R. Salvador, J. Y. Cho, J. Yang, Y.-c. Chien, S.-w. Chen, Y. Tang, and G. J. Snyder, Advanced Functional Materials **23,** 3194 (2013).

[80]   Y. Qiu, J. Xing, X. Gao, L. Xi, X. Shi, H. Gu, and L. Chen, Journal of Materials Chemistry A **2,** 10952 (2014).

[81]   A. Sesselmann, B. Klobes, T. Dasgupta, O. Gourdon, R. Hermann, and E. Mueller, physica status solidi A**,** 1 (2015).

[82]   Y. Tang, Y. Qiu, L. Xi, X. Shi, W. Zhang, L. Chen, S.-M. Tseng, S.-w. Chen, and G. J. Snyder, Energy & Environmental Science **7,** 812 (2014).

[83]   E. Visnow, C. P. Heinrich, A. Schmitz, J. de Boor, P. Leidich, B. Klobes, R. P. Hermann, W. E. Müller, and W. Tremel, Inorganic Chemistry **54,** 7818 (2015).

[84]   L. Xi, Y. Qiu, S. Zheng, X. Shi, J. Yang, L. Chen, D. J. Singh, J. Yang, and W. Zhang, Acta Materialia **85,** 112 (2015).

[85]   W. Zhao, P. Wei, Q. Zhang, H. Peng, W. Zhu, D. Tang, J. Yu, H. Zhou, Z. Liu, X. Mu, D. He, J. Li, C. Wang, X. Tang, and J. Yang, Nat Commun **6,** 6197 (2015).

[86]   X. Shi, J. Yang, L. Wu, J. R. Salvador, C. Zhang, W. L. Villaire, D. Haddad, J. Yang, Y. Zhu, and Q. Li, Scientific Reports **5,** 14641 (2015).

[87]   T. He, J. Chen, H. D. Rosenfeld, and M. A. Subramanian, Chemistry of Materials **18,** 759 (2006).

[88]   C. Seongho, K. Ken, H. Adul, M. Yoshinobu, O. Yuji, M. Hiroaki, and Y. Shinsuke, Japanese Journal of Applied Physics **54,** 111801 (2015).

[89]   R. Mallik, C. Stiewe, G. Karpinski, R. Hassdorf, and E. Müller, Journal of Electronic Materials **38,** 1337 (2009).

[90]   A. Harnwunggmoung, K. Kurosaki, T. Plirdpring, T. Sugahara, Y. Ohishi, H. Muta, and S. Yamanaka, Journal of Applied Physics **110**, 013521 (2011).

[91]   W. Y. Zhao, C. L. Dong, P. Wei, W. Guan, L. S. Liu, P. C. Zhai, X. F. Tang, and Q. J. Zhang, Journal of Applied Physics **102,** 113708 (2007).

[92]   X. Liu, T. Zhu, H. Wang, L. Hu, H. Xie, G. Jiang, G. J. Snyder, and X. Zhao, Advanced Energy Materials **3,** 1238 (2013).

[93]   J. Yang, G. P. Meisner, C. J. Rawn, H. Wang, B. C. Chakoumakos, J. Martin, G. S. Nolas, B. L. Pedersen, and J. K. Stalick, Journal of Applied Physics **102** (2007).

[94]   T. Sekimoto, K. Kurosaki, H. Muta, and S. Yamanaka, MATERIALS TRANSACTIONS **46,** 1481 (2005).

[95]   A. Harnwunggmoung, K. Kurosaki, T. Plirdpring, T. Sugahara, Y. Ohishi, H. Muta, and S. Yamanaka, Journal of Applied Physics **110,** 013521 (2011).

Research Achievements

Publications of Articles

1. **Thermoelectric Properties of Tl-filled Co-free p-type Skutterudites: $Tl_x(Fe,Ni)_4Sb_{12}$,**
   Journal of Applied Physics, **115**, 023702 (2014).
   <u>Seongho Choi</u>, Ken Kurosaki, Yuji Ohishi , Hiroaki Muta, and Shinsuke Yamanaka

2. **Thermoelectric Properties of p-type Tl-Filled Skutterudites: $Tl_xFe_{1.5}Co_{2.5}Sb_{12}$**
   Journal of Electronic Materials, **44**, 1743 (2015).
   <u>Seongho Choi</u>, Ken Kurosaki, Aikebaier Yusufu, Yuji Ohishi , Hiroaki Muta, and Shinsuke Yamanaka

3. **Enhancement of thermoelectric properties of $CoSb_3$ skutterudite by addition of Ga and In**
   Japanese Journal of Applied Physics, **54**, 111801 (2015).
   <u>Seongho Choi</u>, Ken Kurosaki, Adul Harnwunggmoung, Yoshinobu Miyazaki, Yuji Ohishi , Hiroaki Muta, and Shinsuke Yamanaka

International Conference

1. **Thermoelectric Thermoelectric properties of Tl-filled p-type skutterudites**
   Materials Research Society Fall Meeting, Boston (USA), (2013.12).
   <u>Seongho Choi</u>, Ken Kurosaki, Yuji Ohishi, Hiroaki Muta, and Shikuke Yamanaka

2. **High-temperature thermoelectric properties of Tl-filled p-type Co-free skutterudites: $Tl_x(Fe,Ni)_4Sb_{12}$**
   Energy Materials Nanotechnology East Meeting, Beijing (China), (2014.5).
   <u>Seongho Choi</u>, Ken Kurosaki, Yuji Ohishi, Hiroaki Muta, and Shikuke Yamanaka

3. **Thermoelectric properties of Tl-filled p-type skutterudites: $Tl_xFe_{1.5}Co_{2.5}Sb_{12}$**
   International Conference on Thermoelectrics 2014, Neshville (USA), (2014.7).
   <u>Seongho Choi</u>, Ken Kurosaki, Yuji Ohishi, Hiroaki Muta, and Shikuke Yamanaka

4. **Thermoelectric properties of Ga and In co-filled CoSb3–based Skutterudites**
   11th International Conference on Ceramic Materials and Components for Energy and Environmental Applications, Vancouver (Canada), (2015.6).
   <u>Seongho Choi</u>, Ken Kurosaki, Yuji Ohishi, Hiroaki Muta, and Shikuke Yamanaka

Domestic Conference

1. タリウムを添加したコバルトフリーp型スクッテルダイト化合物：$Tl_x(Fe,Ni)_ySb_{12}$の熱電特性

   第十回日本熱電学会学術講演会(TSJ2013)，2013 年 9 月 8-9 日，名古屋大学豊田講堂.
   Seongho Choi，黒崎　健，大石　佑治，牟田　浩明，山中　伸介

Acknowledgements

January, 2016

Seongho Choi